TECHNISCHE
UNIVERSITÄT
DRESDEN

Complex Paths for Regular-to-Chaotic Tunneling Rates

Dissertation
zur Erlangung des wissenschaftlichen Grades
Doctor rerum naturalium

vorgelegt von

Normann Mertig
geboren am 28.05.1983 in Dresden

Institut für Theoretische Physik
Fachrichtung Physik
Fakultät für Mathematik und Naturwissenschaften
Technische Universität Dresden
2013

Eingereicht am 07. Juni 2013

1. Gutachter: Prof. Dr. Roland Ketzmerick
2. Gutachter: Prof. Akira Shudo

Abstract

Tunneling is a fundamental effect of quantum mechanics, which allows waves to penetrate into regions that are inaccessible by classical dynamics. We study this phenomenon for generic non-integrable systems with a mixed phase space, where tunneling occurs between the classically separated phase-space regions of regular and chaotic motion. We derive a semiclassical prediction for the corresponding tunneling rates from the regular region to the chaotic sea. This prediction is based on paths which connect the regular and the chaotic region in complexified phase space. We show that these complex paths can be constructed despite the obstacle of natural boundaries. For the standard map we demonstrate that tunneling rates can be predicted with high accuracy, by using only a few dominant complex paths. This gives the semiclassical foundation for the long-conjectured and often-observed exponential scaling with Planck's constant of regular-to-chaotic tunneling rates.

Zusammenfassung

Tunneln ist ein grundlegender Effekt der Quantenmechanik, welcher es quantenmechanischen Wellenfunktionen erlaubt in Gebiete einzudringen, die der klassischen Dynamik verwehrt bleiben. In dieser Arbeit wird das Phänomen des Tunnelns für generische Hamilton'sche Systeme mit gemischten Phasenraum untersucht. In diesen Systemen tritt das Tunneln zwischen den klassisch getrennten Phasenraumbereichen regulärer und chaotischer Dynamik auf. Für diesen Tunnelprozess wird eine semiklassische Vorhersage regulär-chaotischer Tunnelraten hergeleitet. Diese Vorhersage beruht auf Pfaden, welche Gebiete regulärer und chaotischer Dynamik im komplexen Phasenraum miteinander verbinden. Es wird gezeigt, dass eine Konstruktion dieser komplexen Pfade trotz der Existenz natürlicher Begrenzungen (Engl.: natural boundaries) möglich ist. Die eingeführte Theorie wird auf das Beispiel der Standardabbildung angewandt. Die semiklassisch vorhergesagten Tunnelraten stehen in exzellenter Übereinstimmung mit numerisch bestimmten Tunnelraten und basieren auf einer geringen Anzahl komplexer Pfade. Damit gelingt erstmals eine semiklassische Begründung für den gemeinhin vermuteten und häufig beobachteten exponentiellen Zusammenhang zwischen regulär-chaotischen Tunnelraten und der effektiven Planck'schen Konstante.

Contents

Contents v

1. Introduction 1

2. Systems with a mixed phase space – The standard map 5

- 2.1. The standard map . . . 5
  - 2.1.1. Cylindric and toric phase space . . . 7
  - 2.1.2. Mixed phase space . . . 9
  - 2.1.3. Non-linear resonance chains and partial barriers . . . 10
- 2.2. Quantization of the standard map . . . 12
  - 2.2.1. Quantization on cylindric and toric phase spaces . . . 14
  - 2.2.2. Quantum manifestations of the mixed phase space . . . 18
  - 2.2.3. Quantum manifestations of partial barriers and non-linear resonance chains . . 19

3. Regular-to-chaotic tunneling rates 23

- 3.1. Regular-to-chaotic tunneling rates as decay rates of metastable states . . . 23
  - 3.1.1. Numerical regular-to-chaotic tunneling rates for the standard map . . . 24
- 3.2. Discussion of regular-to-chaotic tunneling rates . . . 26
  - 3.2.1. Regular-to-chaotic tunneling rates and non-linear resonance chains . . . 27
  - 3.2.2. Regular-to-chaotic tunneling rates and partial barriers . . . 28
  - 3.2.3. Regular-to-chaotic tunneling rates and chaos-assisted tunneling . . . 30
- 3.3. Predicting regular-to-chaotic tunneling rates using an improved fictitious integrable system approach . . . 32
  - 3.3.1. Derivation of the improved fictitious integrable system approach . . . 32
  - 3.3.2. Constructing a fictitious integrable system for the standard map . . . 36
  - 3.3.3. Weyl quantization of an integrable system . . . 38
  - 3.3.4. Results for the standard map . . . 40
  - 3.3.5. Discussion and open problems – resonance chains, partial barriers, and regular basis states . . . 44
- 3.4. Summary on quantum-mechanical regular-to-chaotic tunneling rates . . . 45

4. Complex paths for regular-to-chaotic tunneling rates 47
4.1. Semiclassical predictions for regular-to-chaotic tunneling rates 47
4.1.1. Regular-to-chaotic tunneling rates from regular-to-chaotic tunneling-matrix elements 48
4.1.2. Complex paths for regular-to-chaotic tunneling-matrix elements 49
4.1.3. Semiclassical regular-to-chaotic tunneling rates 50
4.2. Constructing regular-to-chaotic complex paths 52
4.3. Results for the standard map 57
4.3.1. Fictitious integrable system approach 57
4.3.2. Improved fictitious integrable system approach 62
4.3.3. Discussion 64
4.4. Tunneling paths in complexified phase space 65

5. Summary and outlook 73

Appendix 77
A. The method of steepest descent 77
A.1. The method of steepest descent in one dimension 77
A.2. Applying the method of steepest descent in physics 79
B. Derivation of complex paths for regular-to-chaotic tunneling-matrix elements 80
B.1. Semiclassical expressions for the basis states and the propagator 80
B.2. Method of steepest descent – The cradle of complex paths 82
B.3. Stability prefactor 85
B.4. WKB-like actions and semiclassical normalization for basis states 86

List of figures 90

1. Introduction

Tunneling is a fascinating quantum-mechanical effect which allows waves to penetrate into regions that are inaccessible by classical dynamics. The discovery of the tunneling effect dates back to a series of seminal papers on molecular spectra [1, 2], nuclear disintegration [3–6], and field emission [7], which unraveled the importance of tunneling in the early days of quantum mechanics. Since then tunneling has been established as a fundamental concept of quantum mechanics leading to Nobel-winning research on electron tunneling [8–10] and scanning-tunneling microscopy [11]. Still, it is driving research on recent frontiers of science, as is, e. g., illustrated by experimental works which demonstrate tunneling for ever larger objects such as atoms [12, 13] and Bose–Einstein condensates [14].

Until today, the textbook picture of tunneling [15, 16] is based on WKB methods [17–21] for integrable systems. For these systems, a WKB-like wave function localizes on a torus, corresponding to regular classical trajectories of energy E inside a potential well $V(q)$. Semiclassically, these wave functions can penetrate through the classically forbidden barrier regions in which $V(q) > E$ along an exponentially decreasing solution of the Schrödinger equation with imaginary momentum $p(q) = \sqrt{2m(E - V(q))}$. This gives rise to an exponentially small tunneling probability of the wave function in classically forbidden regions, leading to metastable states which decay in time. The corresponding tunneling rate of such metastable states is semiclassically given by

$$\gamma \propto \exp\left(-\frac{2\,\mathrm{Im}\,\mathcal{S}}{\hbar}\right). \tag{1.1}$$

This rate depends exponentially on Planck's constant $h = 2\pi\hbar$ and the classical action $\mathcal{S} = \int p(q)\,\mathrm{d}q$ of the single complex path $(q, p(q))$ which goes through the barrier region along the complexified torus of energy E. This is illustrated in Fig. 1.1(a) for the case of a Hamiltonian with cubic potential.

Despite its popularity, this WKB-like picture of tunneling fails for generic non-integrable systems: Such non-integrable systems have a mixed phase space, in which classically separated regions of regular and chaotic motion coexist. Therefore, in contrast to barrier tunneling in integrable systems, non-integrable systems exhibit dynamical tunneling [22, 23] from the regular to the chaotic phase-space region. For this tunneling process it is impossible to find any complex WKB-like path which connects the regular to the chaotic phase-space region. This is due to natural boundaries, beyond which the complexified tori of the regular region cease to exist [24, 25], see Fig. 1.1(b).

Due to the failure of the WKB-method in non-integrable systems, a semiclassical approach to regular-to-chaotic tunneling rates remains an open problem. Its solution is for example important for chaos-assisted tunneling [26–30] for which regular-to-chaotic tunneling is the basic building block. Furthermore, a semiclassical approach to regular-to-chaotic tunneling rates is relevant for applications

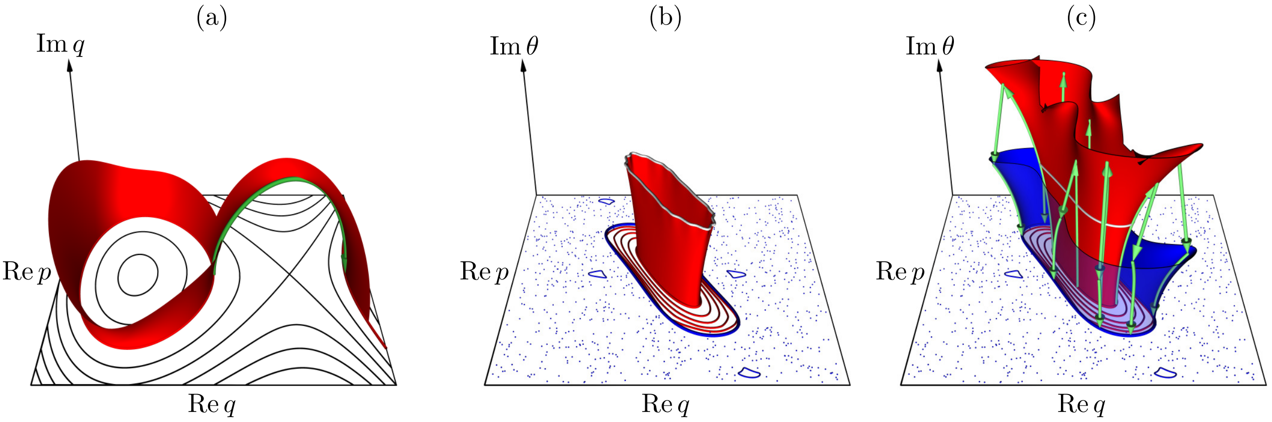

Figure 1.1.: Complex paths for (a) integrable and (c) non-integrable systems. (a) Complexified phase space of an integrable system. The bound motion along regular tori (closed lines) enclosed by the separatrix is semiclassically connected to the regular tori of unbound motion (open lines on the right) by a WKB-like path (green arrow) along the complexified torus (red surface). (b, c) Complexified phase space of the non-integrable standard map with a mixed phase space. Lines show regular tori. Blue dotes show an orbit in the chaotic phase-space region. (b) The complexified regular example torus breaks at the natural boundary (white line), such that a WKB-like path from the regular to the chaotic region does not exist. (c) By using approximate tori for the regular region, which go beyond the natural boundary (white line), we construct complex paths (green arrows) for regular-to-chaotic tunneling rates.

in atomic and molecular physics [31–37], ultra-cold atoms [38–40], optical cavities [41–46], microwave resonators [47–50], spectral statistics [51–54], and the structure of eigenfunctions [55–58] in systems with a mixed phase space. For many of these systems regular-to-chaotic tunneling rates can be determined numerically. Moreover, quantum-mechanical predictions for regular-to-chaotic tunneling rates are available [42, 59–65] and show [64] that regular-to-chaotic tunneling rates exhibit two regimes: (i) The regime $h \lesssim A_{\text{reg}}$ where Planck's constant h is smaller but comparable to the area of the regular region A_{reg}. Here, regular-to-chaotic tunneling rates arise from direct regular-to-chaotic tunneling [42, 62, 65]. (ii) The regime $h \ll A_{\text{reg}}$, where regular-to-chaotic tunneling is additionally affected by resonance-assisted tunneling [59–61, 63].

Nevertheless, a deep understanding of regular-to-chaotic tunneling rates requires a semiclassical theory similar to Eq. (1.1). Up to now, such theories exist for integrable [15, 16, 66, 67] and near-integrable systems [68–75]. However, for non-integrable systems a semiclassical approach to regular-to-chaotic tunneling only exists for propagators in the time domain [76–82]. A semiclassical prediction for regular-to-chaotic tunneling rates, similar to Eq. (1.1), has up to now only been conjectured [83], though, in order to explain the exponential h-scaling of tunneling rates for cavities [42, 43, 47, 50], ultra-cold atoms [40], and quantum maps [65] in the regime $h \lesssim A_{\text{reg}}$.

In this thesis a first semiclassical prediction of direct regular-to-chaotic tunneling rates γ for generic non-integrable systems is achieved in the regime $h \lesssim A_{\text{reg}}$, i. e. in the experimentally relevant regime where γ is large. This prediction is derived by combining the quantum-mechanical predictions of the fictitious integrable system approach, Refs. [62, 65], with the complex-path approach developed by Shudo and Ikeda, Refs. [76–82]. Our main result, Eq. (4.14), uses specific complex paths, whose construction overcomes the conceptual difficulties caused by natural boundaries, see Fig. 1.1(c). It formally resembles Eq. (1.1), but is based on complex paths which contain a time-evolution segment in addition to WKB-like segments. We demonstrate how to predict tunneling rates by our approach and find excellent agreement to numerical tunneling rates for the standard map where only a few complex paths dominate. These results provide a semiclassical foundation of the conjectured exponential h-scaling of regular-to-chaotic tunneling rates.

This thesis is organized as follows: In Chap. 2 we introduce non-integrable systems with a mixed phase space using the paradigmatic example of the standard map and explain both its classical and quantum-mechanical treatment. In Chap. 3 we explain and discuss the concept of regular-to-chaotic tunneling rates and present their quantum-mechanical prediction in terms of the fictitious integrable system approach. The main part of this thesis is presented in Chap. 4 where our complex-path approach to regular-to-chaotic tunneling rates is derived and its application to the standard map is demonstrated. We close this thesis with a summary in Chap. 5.

2. Systems with a mixed phase space – The standard map

Regular-to-chaotic tunneling occurs in generic Hamiltonian systems with a mixed phase space. Such systems comprise ballistic quantum dots, atoms and molecules in a laser field, or optical microcavities. However, for such systems even a numerical treatment of regular-to-chaotic tunneling can become exceedingly complicated. Therefore we exploit the universality of regular-to-chaotic tunneling in Hamiltonian systems with a mixed phase space and study the subject for the standard map, which is the paradigmatic model system that exhibits all generic features of a mixed phase space.

In this chapter we introduce the classical dynamics of the standard map and discuss the notion of a mixed phase space. We further discuss non-linear resonance chains and partial barriers in the standard map. Subsequently, we introduce the quantization of the standard map and qualitatively elucidate quantum manifestations of such classical phase-space structures.

2.1. The standard map

The standard map belongs to the class of kicked Hamiltonian systems, defined by Hamilton functions of the form

$$H(q,p,t) = T(p) + V(q) \sum_{n\in\mathbb{Z}} \delta(t-n). \tag{2.1}$$

Here, $T(p)$ is the kinetic energy. It governs the free motion of a particle which is exposed to a kicking potential $V(q)$ once per unit in time. The standard map [84] in dimensionless units is obtained by using the kinetic energy

$$T(p) = \frac{p^2}{2} \tag{2.2}$$

combined with the kicking potential

$$V(q) = \frac{\kappa}{(2\pi)^2} \cos(2\pi q). \tag{2.3}$$

Since the kicking strength κ is an external parameter, the standard map denotes a whole family of systems.

In order to study the classical dynamics of such a kicked system, it is convenient to consider the system stroboscopically. This gives rise to the stroboscopic map U, which determines how the system evolves in phase space during one period of the external driving. More specifically, starting at (q, p) at time t_0 we reach (q', p') at time $t' = t_0 + 1$ according to

$$(q', p') = U(q, p) = (U_{\text{pos}}(q, p), U_{\text{mom}}(q, p)). \tag{2.4}$$

In order to obtain this mapping U explicitely one has to integrate Hamilton's equations of motion,

$$\dot{q}(t) := \frac{\mathrm{d}q(t)}{\mathrm{d}t} = \frac{\partial H(q(t), p(t), t)}{\partial p}, \tag{2.5a}$$

$$\dot{p}(t) := \frac{\mathrm{d}p(t)}{\mathrm{d}t} = -\frac{\partial H(q(t), p(t), t)}{\partial q}, \tag{2.5b}$$

which read

$$\dot{q}(t) = T'(p(t)), \tag{2.6a}$$

$$\dot{p}(t) = -V'(q(t)) \sum_{n \in \mathbb{Z}} \delta\,(t - n) \tag{2.6b}$$

for a kicked system, Eq. (2.1), with

$$T'(p) := \frac{\partial T(p)}{\partial p}, \tag{2.7a}$$

$$V'(q) := \frac{\partial V(p)}{\partial q}. \tag{2.7b}$$

Since such a map U originate from a Hamiltonian time evolution it is area preserving.

Mappings U for different initial times t_0 are topologically equivalent. Even more they are all related by a canonical transformation. We obtain the class of *generalized half-free* mappings by choosing $t_0 = \delta_{\text{hf}}$, which splits the external period into a free evolution for the time $1 - \delta_{\text{hf}}$, followed by the kick, and a further free evolution which lasts for the time δ_{hf} until $t = 1 + \delta_{\text{hf}}$,

$$q' = q + (1 - \delta_{\text{hf}})T'(p) + \delta_{\text{hf}} T'\left(p - V'\left(q + (1 - \delta_{\text{hf}})T'(p)\right)\right), \tag{2.8a}$$

$$p' = p - V'\left(q + (1 - \delta_{\text{hf}})T'(p)\right). \tag{2.8b}$$

In the above equations δ_{hf} takes values in the interval $[0, 1]$. The class of *generalized half-kick* mappings can be obtained by considering the δ_{hk}'s part of the kick, followed by the free evolution for one unit of time and after that the remaining $(1 - \delta_{\text{hk}})$'s part of the kick,

$$q' = q + T'\left(p - \delta_{\text{hk}} V'(q)\right), \tag{2.9a}$$

$$p' = p - \delta_{\text{hk}} V'(q) - (1 - \delta_{\text{hk}})V'\left(q + T'\left(p - \delta_{\text{hk}} V'(q)\right)\right). \tag{2.9b}$$

Here, δ_{hk} also runs in $[0, 1]$. The three most common representations of the mapping U are: (i) the *after-kick* map $\delta_{\mathrm{hf}} = 0$, (ii) the *half-free* map $\delta_{\mathrm{hf}} = 1/2$, and (iii) the *half-kick* map $\delta_{\mathrm{hk}} = 1/2$. When discussing the standard map we will focus on its after-kick representation,

$$q' = q + p, \tag{2.10a}$$

$$p' = p + \frac{\kappa}{2\pi}\sin(2\pi[q+p]). \tag{2.10b}$$

For semiclassics it is important to define the action

$$\mathcal{S}(q(t_0), p(t_0);\, t_0, t_0+1) := \int_{t_0}^{t_0+1} [\dot{q}(t)p(t) - H(q(t), p(t), t)]\,\mathrm{d}t. \tag{2.11}$$

For a time-discrete mapping U, an orbit starting at (q,p) acquires the action $\mathcal{S}^U(q,p)$. For the class of generalized half-free mappings this results in

$$\mathcal{S}^U(q,p) = (1-\delta_{\mathrm{hf}})\left[p\,T'(p) - T(p)\right] - V\left(q + (1-\delta_{\mathrm{hf}})T'(p)\right) + \delta_{\mathrm{hf}}\left[p'\,T'(p') - T(p')\right] \tag{2.12}$$

with $p' = U_{\mathrm{mom}}(q,p)$, Eq. (2.8b), while the class of generalized half-kick mappings has

$$\mathcal{S}^U(q,p) = -\delta_{\mathrm{hk}}V(q) + \left[(p - \delta_{\mathrm{hk}}V'(q))T'(p - \delta_{\mathrm{hk}}V'(q)) - T(p - \delta_{\mathrm{hk}}V'(q))\right] - (1-\delta_{\mathrm{hk}})V(q'), \tag{2.13}$$

with $q' = U_{\mathrm{pos}}(q,p)$, Eq. (2.9a). If one eliminates one of the initial coordinates (q,p) by one of the final coordinates (q',p') using the mapping, Eqs. (2.8) in Eq. (2.12) or Eqs. (2.9) in Eq. (2.13) respectively, the action $\mathcal{S}^U$ becomes a generating function. The most common case of a generating function is $\mathcal{S}^U(q,q')$ as a function of the initial and final position. For such a function one can show that the following relations hold,

$$\frac{\partial \mathcal{S}^U(q,q')}{\partial q} = -p(q,q'), \tag{2.14a}$$

$$\frac{\partial \mathcal{S}^U(q,q')}{\partial q'} = p'(q,q'). \tag{2.14b}$$

For the chosen after-kick representation of the standard map the corresponding action $\mathcal{S}^U$ can be written as such a generating function,

$$\mathcal{S}^U(q,q') = \frac{(q-q')^2}{2} - V(q'). \tag{2.15}$$

2.1.1. Cylindric and toric phase space

So far we have considered mappings on the unbound phase space $\mathbb{R}^2$. However, such a phase space is numerically hard to access. It is convenient to exploit the intrinsic periodicity of U and to restrict the phase space to a cylinder or a torus, by applying periodic boundary conditions. For example, if the classical dynamics is M_{pos}-periodic in position, i. e., $\forall r \in \mathbb{Z}\ \exists k \in \mathbb{Z}$, such that

$$U_{\text{pos}}(q,p) = U_{\text{pos}}(q + rM_{\text{pos}}, p) + kM_{\text{pos}} \quad \wedge \quad U_{\text{mom}}(q,p) = U_{\text{mom}}(q + rM_{\text{pos}}, p) \tag{2.16}$$

holds, it is meaningful to restrict the phase space of U to a cylinder $\big(\mathbb{R}/(q_{\text{min}} + M_{\text{pos}}\mathbb{Z})\big) \times \mathbb{R}$, with

$$(q', p') = \left([(U_{\text{pos}}(q,p) - q_{\text{min}}) \mod M_{\text{pos}}] + q_{\text{min}}, U_{\text{mom}}(q,p)\right). \tag{2.17}$$

For the standard map $V(q)$, Eq. (2.3), is $M_{\text{pos}} = 1$-periodic. Hence, the map U, Eq. (2.10), satisfies condition (2.16) and it is possible to consider the classical dynamics on a cylinder $\big(\mathbb{R}/\mathbb{Z}\big) \times \mathbb{R}$.

If the classical dynamics is M_{mom}-periodic in momentum, i. e., $\forall s \in \mathbb{Z}\ \exists l \in \mathbb{Z}$, such that

$$U_{\text{pos}}(q,p) = U_{\text{pos}}(q, p + sM_{\text{mom}}) \quad \wedge \quad U_{\text{mom}}(q,p) = U_{\text{mom}}(q, p + sM_{\text{mom}}) + lM_{\text{mom}}, \tag{2.18}$$

holds, it is meaningful to restrict the phase space of U to a cylinder $\mathbb{R} \times \big(\mathbb{R}/(p_{\text{min}} + M_{\text{mom}}\mathbb{Z})\big)$, with

$$(q', p') = \big(U_{q'}(q,p), \big[\big(U_{p'}(q,p) - p_{\text{min}}\big) \mod M_{\text{mom}}\big] + p_{\text{min}}\big). \tag{2.19}$$

Please note, that the classical dynamics of the standard map, Eqs. (2.10), cannot satisfy condition (2.18) for any M_{mom}. Therefore, the classical dynamics of the standard map cannot be considered on the cylinder $\mathbb{R} \times \big(\mathbb{R}/(p_{\text{min}} + M_{\text{mom}}\mathbb{Z})\big)$. This has its origin in the fact that $T(p)$, Eq. (2.2), is not periodic for any M_{mom}. In case one considers the standard map on a cylinder $\mathbb{R} \times \big(\mathbb{R}/(p_{\text{min}} + M_{\text{mom}}\mathbb{Z})\big)$ nevertheless, one implicitly assumes a modified kinetic energy,

$$\tilde{T}(p) := T([(p - p_{\text{min}}) \mod M_{\text{mom}}] + p_{\text{min}}), \tag{2.20}$$

which is periodic in M_{mom}. The classical dynamics generated by $\tilde{T}(p)$ does not differ from the dynamics of the standard map as long as the momentum remains bound in $[p_{\text{min}}, p_{\text{min}} + M_{\text{mom}})$. However, any classical orbit which propagates beyond this interval shows deviating classical dynamics.

Finally, if the classical dynamics of U is both M_{pos}-periodic in position and M_{mom}-periodic in momentum, i. e., $\forall r, s \in \mathbb{Z}\ \exists k, l \in \mathbb{Z}$, such that

$$\begin{aligned} U_{\text{pos}}(q,p) &= U_{\text{pos}}(q + rM_{\text{pos}}, p + sM_{\text{mom}}) + kM_{\text{pos}}, \\ U_{\text{mom}}(q,p) &= U_{\text{mom}}(q + rM_{\text{pos}}, p + sM_{\text{mom}}) + lM_{\text{mom}}, \end{aligned} \tag{2.21}$$

it is meaningful to restrict the phase space of U to a torus $\big(\mathbb{R}/(q_{\text{min}} + M_{\text{pos}}\mathbb{Z})\big) \times \big(\mathbb{R}/(p_{\text{min}} + M_{\text{mom}}\mathbb{Z})\big)$, with

$$(q', p') = \left([(U_{\text{pos}}(q,p) - q_{\text{min}}) \mod M_{\text{pos}}] + q_{\text{min}}, [(U_{\text{mom}}(q,p) - p_{\text{min}}) \mod M_{\text{mom}}] + p_{\text{min}}\right). \tag{2.22}$$

Since the after-kick representation of the standard map, Eq. (2.10), satisfies condition (2.21) for

$M_{\mathrm{pos}} = M_{\mathrm{mom}} = 1$ its dynamics can be considered on the torus $\big(\mathbb{R}/\mathbb{Z}\big) \times \big(\mathbb{R}/(-0.5+\mathbb{Z})\big)$.

2.1.2. Mixed phase space

In the following we use the standard map on the torus to illuminate typical phase-space structures of Hamiltonian systems. We start by introducing the notion of an orbit, which is a collection of phase-space points

$$\{U^n(q,p) \ : \ n \in \mathbb{N}\}\,. \tag{2.23}$$

Here, U^n denotes the n-fold application of the map U to a phase-space point (q,p).

For $\kappa = 0.0$ the standard map is an integrable system for which all orbits show regular dynamics. This dynamics is restricted to one-dimensional tori in phase space due to momentum conservation, see Fig. 2.1(a). On the contrary the phase space of the standard map at sufficiently large κ typically hosts chaotic orbits, which explore the whole two-dimensional phase space, see Fig. 2.1(d). However, generic Hamiltonian systems have a mixed phase space in which orbits of regular and chaotic motion coexist on dynamically disjoint phase-space regions, see Figs. 2.1(b, c). Such systems with a mixed phase space can further be classified as weakly perturbed near-integrable or strongly perturbed non-integrable systems. The near-integrable phase space appears in the standard map for small κ. Here, the integrable motion is weakly perturbed by the kick such that regular tori with sufficiently irrational frequencies survive the perturbation and get deformed [85, 86], see red lines in Fig. 2.1(b), while tori with rational frequencies break into chains of regular regions [87], see orange circles in Fig. 2.1(b), around which thin layers of chaotic motion emerge, illustrated by the blue dots in Fig. 2.1(b). Finally, for stronger perturbations at larger κ the standard map shows the typical non-integrable phase space in which regular and chaotic regions are equally pronounced, see Fig. 2.1(c). In such non-integrable systems regular phase-space regions embedded in a chaotic phase-space region are omnipresent, such that regular-to-chaotic tunneling is ubiquitous in their quantum-mechanical counter part. Beyond

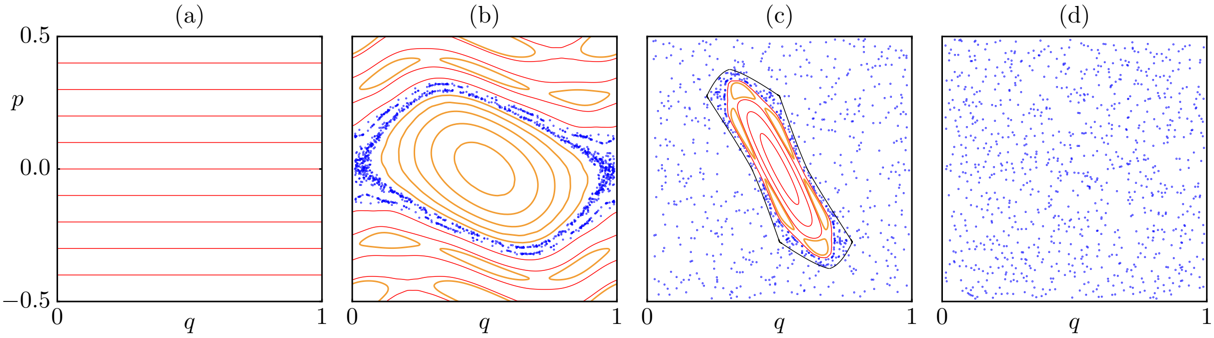

Figure 2.1.: Phase space of the standard map for (a) $\kappa = 0.0$, (b) $\kappa = 0.8$, (c) $\kappa = 3.5$, and (d) $\kappa = 10.0$. Red and orange lines depict tori of regular motion, with orange lines highlighting non-linear resonance chains. Blue dots show orbits of chaotic motion, while black lines indicate a partial barrier.

the omnipresent regular–chaotic phase-space setting it is known that regular-to-chaotic tunneling in non-integrable systems is further affected by non-linear resonance chains in the regular region [59, 60], see orange circles in Fig. 2.1(c). Furthermore, the hierarchical region, which is the chaotic part of phase space next to the regular region contains partial barriers. For an example see the black lines in Fig. 2.1(c). Those barriers can trap a chaotic orbit close to the regular region for many iterations, before it explores the part of the chaotic region beyond the partial barrier. This effect is illustrated by the varying density of blue dots in Fig. 2.1(c).

2.1.3. Non-linear resonance chains and partial barriers

The goal of the upcoming discussion is to motivate why considering the standard map for $\kappa = 2.9$ is optimal for the investigation of regular-to-chaotic tunneling.

In order to understand why this is an interesting question, note that in the regime $\kappa \in [1, 4]$ the standard map has a stable fixed-point at $(q, p) = (0.5, 0.0)$ which is encircled by tori of regular motion. This regular region is further embedded in a connected chaotic phase-space region [88]. At first glance the whole κ-regime with $\kappa \in [1, 4]$ thus seems equally ideal for studying regular-to-chaotic tunneling. However, the secondary phase-space structures, comprising non-linear resonance chains and partial transport barriers, vary considerably, which can add significant complexity to regular-to-chaotic tunneling. Motivated by this fact, we order these classical phase-space structures for the standard map in this section, i. e., we give an overview of these structures as a function of the kicking strength κ, see Figs. 2.3 and 2.4.

From the linearization of the standard map, Eq. (2.10), we compute the frequency of trajectories in the vicinity of the elliptic fixed point $(q, p) = (0.5, 0.0)$,

$$\nu = \frac{1}{\pi} \arcsin\left(\frac{\sqrt{\kappa}}{2}\right), \tag{2.24}$$

where the angle $2\pi\nu$ describes the clockwise rotation of an orbit in one time step. When increasing κ from zero to four, the frequency around the center rises from zero to $1/2$. Accompanying this parameter change, the regular orbits with lower frequency which were formerly close to the central fixed point get shifted towards the regular-chaotic border region. Reminiscent of the near-integrable regime, orbits with sufficiently irrational frequency form regular tori, while orbits with rational frequency,

$$\nu = \frac{s}{r}, \quad s \in \mathbb{Z}, r \in \mathbb{N} \tag{2.25}$$

form a non-linear $r : s$ resonance chain. Such a resonance chain contains r regular regions. Applying U r times results in s clockwise rotations around the fixed point, see the orange circles which show a $6 : 2$ resonance in Fig. 2.1(c). According to Eqs. (2.24) and (2.25), an $r : s$ resonance emerges from the fixed point at κ-values

$$\kappa = 4 \sin\left(\pi \frac{s}{r}\right)^2. \tag{2.26}$$

With increasing κ this resonance is shifted towards the outside until the regular-chaotic border is reached. There the resonance starts to dissolve in the chaotic region. Related to this non-linear resonance chain, there are r unstable periodic points, which are located between the regular regions along the resonance chain. When the resonance enters the chaotic region, the stable and unstable manifolds of these r unstable periodic points give rise to partial barriers, which dominate the transport in the hierarchical region around the regular phase-space region, see, e. g., black lines in Fig. 2.1(c). This implies that non-linear resonance chains and partial barriers are related by changes of the parameter κ.

Roughly speaking the relevance of non-linear resonances and partial barriers for regular-to-chaotic tunneling decreases with rising order r of the resonance. This allows for setting up a scheme for the most relevant resonance frequencies which emerge from the fixed point of the standard map as κ rises from one to four, Fig. 2.2. Due to the parity of the standard map this scheme contains resonances with even order r only. Using Eq. (2.26) we can compute the parameter value κ for which these resonances emerge from the fixed point and trace it to the parameter value κ when the resonance chain is roughly at the regular–chaotic border. Note that the resonance chain is destroyed at a larger κ-parameter. This allows for assigning each κ-value its most relevant resonance chain, see Fig. 2.3.

Beyond the κ parameter for which a resonance starts to dissolve in the chaotic region, we exploit the stable and unstable manifolds of the r unstable points of the resonance chain for constructing partial barriers of the hierarchical region. For increasing κ these structures continue to exist and similar to non-linear resonance chains a scheme of partial barrier in the chaotic region can be established, see Fig. 2.4.

As explained later in this thesis, it is favorable for our investigations to consider a κ parameter for which the dominating resonance has a high order r. From Fig. 2.3 this gives the regime $\kappa \in [2.445\ldots, 2.618\ldots]$ in which the 14 : 4 resonance dominates. However, there the 4 : 1 resonance is still quite dominant, even though it localizes in the chaotic part of phase space already. This leaves

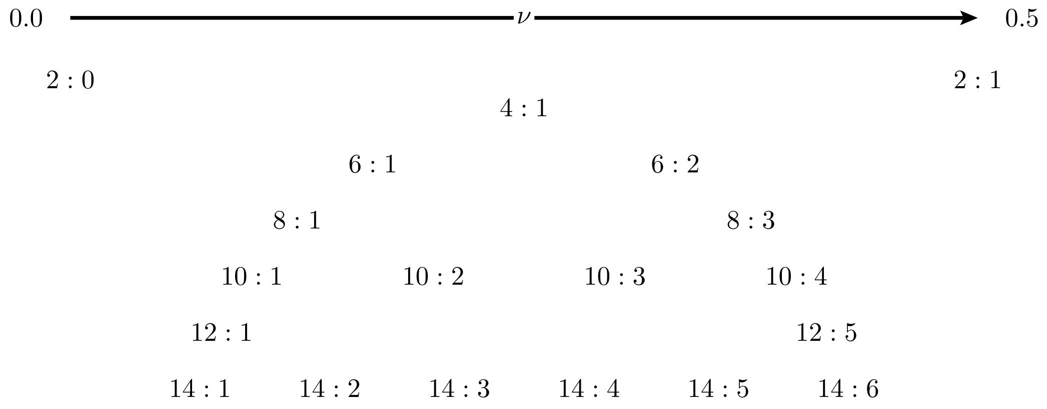

Figure 2.2.: Scheme of lowest order $r : s$ resonances emerging from the fixed point $(q, p) = (0.5, 0.0)$ of the standard map for $\kappa \in [0, 4]$, where $\nu \in (0.0, 0.5)$.

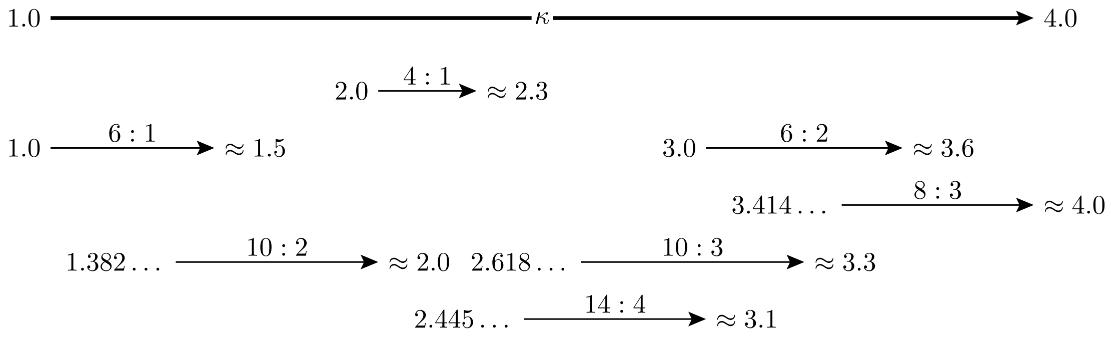

Figure 2.3.: Overview giving the lowest order resonance of the regular region around the fixed point $(q, p) = (0.5, 0.0)$ of the standard map as a function of the kicking strength $\kappa \in [1, 4]$.

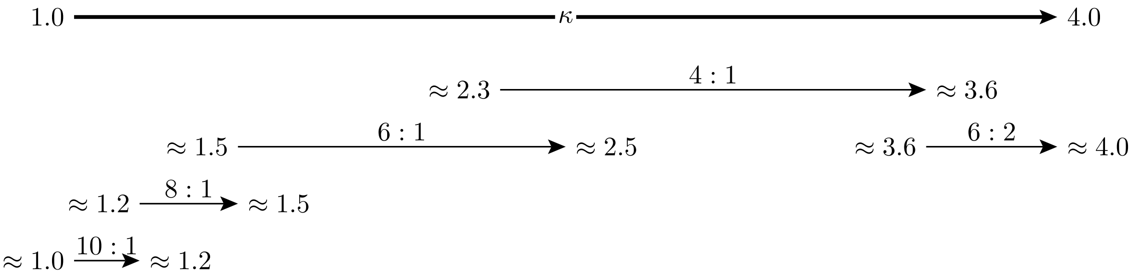

Figure 2.4.: Overview giving the partial barriers parametrically originating from the lowest order $r : s$ resonances of the regular region around the fixed point $(q, p) = (0.5, 0.0)$ of the standard map as a function of the kicking strength $\kappa \in [1, 4]$.

the parameter ranges $\kappa \in [1.5, 2.0]$ and $\kappa \in [2.618\ldots, 3.0]$ as next natural choices for which the $10 : 2$ and the $10 : 3$ resonance are dominant, see Fig. 2.3. From experience it seems that the regime $\kappa \in [1.5, 2.0]$ of the $10 : 2$ resonance is still exposed to more partial barriers in the chaotic region, and thus, we favor the regime $\kappa \in [2.618\ldots, 3.0]$ of the $10 : 3$ resonance in which the hierarchical region is clearly dominated by the single partial barrier of the dissolved $4 : 1$ resonance. Since there is published tunneling data available already [62], we focus on the parameter $\kappa = 2.9$ in this thesis.

2.2. Quantization of the standard map

The quantum-mechanical counterpart of a kicked systems Hamilton function, Eq. (2.1), is given by the operator

$$\widehat{H}(\hat{q}, \hat{p}, t) = T(\hat{p}) + V(\hat{q}) \sum_{n \in \mathbb{Z}} \delta(t - n), \tag{2.27}$$

where $\hat{p}$ and $\hat{q}$ are the position and momentum operators which fulfill the standard commutation relation,

$$[\hat{q},\hat{p}] = \mathrm{i}\hbar. \tag{2.28}$$

Here, $2\pi\hbar = h \in \mathbb{R}$ is the dimensionless effective Planck constant, which is a free parameter in our studies. Note that $\hbar$ is called the reduced effective Planck constant.

Since $\widehat{H}$ is periodic in time,

$$\widehat{H}(\hat{q},\hat{p},t) = \widehat{H}(\hat{q},\hat{p},t+1), \tag{2.29}$$

it is convenient to apply Floquet theory [89, 90], which can be done by considering the time-evolution operator $\widehat{U}$ over one period of the driving. This operator $\widehat{U}$ is the quantum-mechanical analog of the classical map U. Similar to the classical map there exist many representations of the time-evolution operator. The analog of the generalized half-free representations, Eq. (2.8), is given by

$$\widehat{U} = \exp\left(-\frac{\mathrm{i}}{\hbar}\delta_{\mathrm{hf}}T(\hat{p})\right)\exp\left(-\frac{\mathrm{i}}{\hbar}V(\hat{q})\right)\exp\left(-\frac{\mathrm{i}}{\hbar}(1-\delta_{\mathrm{hf}})T(\hat{p})\right) \tag{2.30}$$

and the analog of the generalized half-kick, Eq. (2.9), representation by

$$\widehat{U} = \exp\left(-\frac{\mathrm{i}}{\hbar}(1-\delta_{\mathrm{hk}})V(\hat{q})\right)\exp\left(-\frac{\mathrm{i}}{\hbar}T(\hat{p})\right)\exp\left(-\frac{\mathrm{i}}{\hbar}\delta_{\mathrm{hk}}V(\hat{q})\right). \tag{2.31}$$

In analogy to the classical part, we will consider the time-evolution operator $\widehat{U}$ of the standard map in its after-kick representation,

$$\widehat{U} = \exp\left(-\frac{\mathrm{i}}{\hbar}V(\hat{q})\right)\exp\left(-\frac{\mathrm{i}}{\hbar}T(\hat{p})\right). \tag{2.32}$$

For numerical purposes it is convenient to deal with this operator in position representation, which requires an evaluation of $\exp(\mathrm{i}\,T(p)/\hbar)$ in Fourier space

$$\langle q'|\widehat{U}|q\rangle = \exp\left(-\frac{\mathrm{i}}{\hbar}V(q')\right)\frac{1}{2\pi\hbar}\int_{\mathbb{R}}\mathrm{d}p\,\exp\left(-\frac{\mathrm{i}}{\hbar}\left[T(p)+p(q-q')\right]\right). \tag{2.33}$$

Since $T(p)$ is quadratic, Eq. (2.2), we can compute the arising Gaussian integral analytically [91, 92],

$$\langle q'|\widehat{U}|q\rangle = \left(\frac{1}{2\pi\hbar}\right)^{\frac{1}{2}} e^{-\mathrm{i}\frac{\pi}{4}}\exp\left(\frac{\mathrm{i}}{\hbar}\left[\frac{(q-q')^2}{2}-V(q')\right]\right), \tag{2.34}$$

which for the standard map results exactly in the shape of the general semiclassical propagator [91],

$$\langle q'|\widehat{U}|q\rangle = \left(\frac{\mathrm{i}}{2\pi\hbar}\frac{\partial^2\mathcal{S}^U(q,q')}{\partial q\partial q'}\right)^{\frac{1}{2}}\exp\left(\frac{\mathrm{i}}{\hbar}\mathcal{S}^U(q,q')\right). \tag{2.35}$$

This semiclassical propagator is composed from classical orbits that propagate from q to q', taking their action $\mathcal{S}^U$, Eq. (2.15), and stability $\partial_q \partial_{q'} \mathcal{S}^U$ into account.

2.2.1. Quantization on cylindric and toric phase spaces

Similar to the classical case, it is convenient for numerical purposes to consider a restriction of the time-evolution operator $\widehat{U}$ to cylindric or toric phase space. To this end, we will now exploit the Bloch theorem [93]. If the time-evolution operator $\widehat{U}$ is M_{pos}-periodic, i. e., it commutes with the translation operator $\widehat{T}_{M_{\text{pos}}}$

$$[\widehat{U}, \widehat{T}_{M_{\text{pos}}}] = 0, \tag{2.36}$$

with

$$\widehat{T}_{M_{\text{pos}}} := \exp\left(-\frac{\mathrm{i}}{\hbar} M_{\text{pos}} \hat{p}\right), \tag{2.37}$$

the Bloch theorem holds, such that the Hilbert space $\mathcal{H}$ on which $\widehat{U}$ acts can be decomposed into disjoint subsets $\mathcal{H}(\theta_{\text{pos}})$, which are determined by the Bloch phase $\theta_{\text{pos}} \in [0, 1)$. The states $|\Psi\rangle$ within $\mathcal{H}(\theta_{\text{pos}})$ are quasi-periodic,

$$\widehat{T}_{M_{\text{pos}}} |\Psi\rangle = \exp\left(-\mathrm{i}2\pi\theta_{\text{pos}}\right) |\Psi\rangle, \tag{2.38}$$

and can be represented on a complete set of basis states $|p_n\rangle$ which form a lattice

$$p_n := \frac{2\pi\hbar}{M_{\text{pos}}}(n + \theta_{\text{pos}}) \tag{2.39}$$

with $n \in \mathbb{Z}$ in momentum representation,

$$\langle p | p_n \rangle := \sqrt{\frac{2\pi\hbar}{M_{\text{pos}}}}\, \delta(p - p_n). \tag{2.40}$$

In position space the same basis is a set of quasi-periodic functions,

$$\langle q | p_n \rangle = \frac{1}{\sqrt{M_{\text{pos}}}} \exp\left(\frac{\mathrm{i}}{\hbar} p_n q\right). \tag{2.41}$$

If we expand $\widehat{U}$ such that

$$\widehat{U} |p_n\rangle = \sum_{p_k} \langle p_k | \widehat{U} | p_n \rangle \, |p_k\rangle \tag{2.42}$$

then $\langle p_k | \widehat{U} | p_n \rangle$ is the matrix representation of $\widehat{U}$ on the cylinder $\big(\mathbb{R}/(q_{\min} + M_{\text{pos}}\mathbb{Z})\big) \times \mathbb{R}$. For the standard map $V(q)$, Eq. (2.3), is periodic with $M_{\text{pos}} = 1$ such that $\widehat{U}$ commutes with $\widehat{T}_{M_{\text{pos}}}$ and is given by

$$\langle p_k|\widehat{U}|p_n\rangle = \int_{q_{\min}}^{q_{\min}+1} \mathrm{d}q \, \exp\left(\mathrm{i}2\pi(n-k)\frac{q}{M_{\mathrm{pos}}}\right)\exp\left(-\frac{\mathrm{i}}{\hbar}V(q)\right)\exp\left(-\frac{\mathrm{i}}{\hbar}T(p_n)\right) \tag{2.43a}$$

$$= \mathrm{i}^{(k-n)}\frac{1}{2\pi}\int_{-\pi}^{\pi} \mathrm{d}x \, \exp\left(-\mathrm{i}\left[(k-n)x + \frac{\kappa}{(2\pi)^2\hbar}\sin(x)\right]\right)\exp\left(-\frac{\mathrm{i}}{\hbar}T(p_n)\right) \tag{2.43b}$$

$$= \mathrm{i}^{(k-n)}\mathrm{J}_{(k-n)}\left(-\frac{\kappa}{(2\pi)^2\hbar}\right)\exp\left(-\frac{\mathrm{i}}{\hbar}T(p_n)\right) \tag{2.43c}$$

on the cylinder $\big(\mathbb{R}/\mathbb{Z}\big)\times\mathbb{R}$, with $\mathrm{J}_{(k-n)}\left(-\kappa/[(2\pi)^2\hbar]\right)$ being a Bessel function of the first kind.

Analogously, if $\widehat{U}$ commutes with the translation operator $\widehat{T}_{M_{\mathrm{mom}}}$,

$$[\widehat{U},\widehat{T}_{M_{\mathrm{mom}}}] = 0, \tag{2.44}$$

with

$$\widehat{T}_{M_{\mathrm{mom}}} := \exp\left(\frac{\mathrm{i}}{\hbar}M_{\mathrm{mom}}\hat{q}\right), \tag{2.45}$$

the Hilbert space $\mathcal{H}$ can be decomposed into disjoint subsets $\mathcal{H}(\theta_{\mathrm{mom}})$, which are determined by the Bloch phase $\theta_{\mathrm{mom}}\in[0,1)$. The states $|\Psi\rangle$ within $\mathcal{H}(\theta_{\mathrm{mom}})$ are quasi-periodic,

$$\widehat{T}_{M_{\mathrm{pos}}}\,|\Psi\rangle = \exp\left(\mathrm{i}2\pi\theta_{\mathrm{mom}}\right)|\Psi\rangle\,, \tag{2.46}$$

and can be represented on a complete set of basis states $|q_l\rangle$ which form a lattice

$$q_l := \frac{2\pi\hbar}{M_{\mathrm{mom}}}(l+\theta_{\mathrm{mom}}), \tag{2.47}$$

with $l\in\mathbb{Z}$ in position representation,

$$\langle q|q_l\rangle := \sqrt{\frac{2\pi\hbar}{M_{\mathrm{mom}}}}\,\delta(q-q_l). \tag{2.48}$$

In momentum space the same basis is a set of quasi-periodic functions,

$$\langle p|q_l\rangle := \frac{1}{\sqrt{M_{\mathrm{mom}}}}\exp\left(\frac{\mathrm{i}}{\hbar}q_l p\right). \tag{2.49}$$

If we expand $\widehat{U}$ such that

$$\widehat{U}\,|q_l\rangle = \sum_{q_k}\langle q_k|\widehat{U}|q_l\rangle\,|q_k\rangle \tag{2.50}$$

then $\langle q_k|\widehat{U}|q_l\rangle$ is the matrix representation of $\widehat{U}$ on the cylinder $\mathbb{R}\times\big(\mathbb{R}/(p_{\min}+M_{\mathrm{mom}}\mathbb{Z})\big)$. The time-evolution operator $\widehat{U}$ of the standard map does not commute with $\widehat{T}_{M_{\text{mom}}}$ for any M_{mom}, since $T(p)$, Eq. (2.2), is not periodic with any M_{mom}. Hence, the quantization of the standard map on the cylinder $\mathbb{R} \times \big(\mathbb{R}/(p_{\text{min}} + M_{\text{mom}}\mathbb{Z})\big)$ is mathematically not defined. However, similar to the classical case, it is physically justified that $T(p)$ can be replaced by $\tilde{T}(p)$, Eq. (2.20), if it is sufficient to describe the eigenstates of $\widehat{U}$ between $[p_{\text{min}}, p_{\text{min}} + M_{\text{mom}})$, which localize sufficiently far away from the border regions. In that case $\widehat{U}$ and $\widehat{T}_{M_{\text{mom}}}$ commute such that $\widehat{U}$ is given by

$$\langle q_k|\widehat{U}|q_l\rangle = \exp\left(-\frac{\mathrm{i}}{\hbar}V(q_k)\right) \int\limits_{p_{\text{min}}}^{p_{\text{min}}+1} \frac{\mathrm{d}p}{M_{\text{mom}}} \exp\left(-\mathrm{i}2\pi(k-l)\frac{p}{M_{\text{mom}}}\right) \exp\left(-\frac{\mathrm{i}}{\hbar}T(p)\right), \tag{2.51}$$

which for $p_{\text{min}} = -1/2$ and $M_{\text{mom}} = 1$ gives

$$\langle q_k|\widehat{U}|q_l\rangle = \exp\left(-\frac{\mathrm{i}}{\hbar}V(q_k)\right)\sqrt{\frac{\pi\hbar}{2\mathrm{i}}} \exp\left(-\mathrm{i}\pi^2\hbar(k-l)\right) \tag{2.52}$$

$$\left[\mathrm{erf}\left(\sqrt{\frac{2\hbar}{\mathrm{i}}}\left[\frac{1}{2} + \pi(k-l)\right]\right) - \mathrm{erf}\left(\sqrt{\frac{2\hbar}{\mathrm{i}}}\left[-\frac{1}{2} + \pi(k-l)\right]\right)\right], \tag{2.53}$$

with erf being the error function.

Finally, if we consider an operator which commutes both with the translation operator in position space, Eq. (2.36), and the translation operator in momentum space, Eq. (2.44), it is possible to introduce a set of basis states on a torus $\big(\mathbb{R}/(q_{\text{min}} + M_{\text{pos}}\mathbb{Z})\big) \times \big(\mathbb{R}/(p_{\text{min}} + M_{\text{mom}}\mathbb{Z})\big)$. In order to allow for such states it is further required that the translation operators commute,

$$[\widehat{T}_{M_{\text{pos}}}, \widehat{T}_{M_{\text{mom}}}] = \widehat{T}_{M_{\text{pos}}}\widehat{T}_{M_{\text{mom}}}\left[1 - \exp\left(\mathrm{i}2\pi\frac{M_{\text{pos}}M_{\text{mom}}}{2\pi\hbar}\right)\right] \overset{!}{=} 0, \tag{2.54}$$

which restricts the allowed values of the effective Planck constant h, see, e. g., Ref. [94, 95],

$$h = 2\pi\hbar = \frac{M_{\text{pos}}M_{\text{mom}}}{N} \quad \text{with} \quad N \in \mathbb{N}. \tag{2.55}$$

By Bloch's theorem, the Hilbert space $\mathcal{H}$ can now be decomposed into disjoint subsets $\mathcal{H}(\theta_{\text{pos}}, \theta_{\text{mom}})$, which are determined by the Bloch phases $(\theta_{\text{pos}}, \theta_{\text{mom}}) \in [0,1) \times [0,1)$. The states $|\Psi\rangle$ within $\mathcal{H}(\theta_{\text{pos}}, \theta_{\text{mom}})$ are quasi-periodic under translations both in position and momentum, Eqs. (2.40) and (2.46), and therefore exist on lattices both in position and momentum representation, Eqs. (2.47) and (2.39), simultaneously. Such states can either be decomposed into the basis $|\overline{q}_l\rangle$ or the basis $|\overline{p}_n\rangle$. While states $|\overline{q}_l\rangle$ have the position representation

$$\langle q|\overline{q}_l\rangle := \sqrt{\frac{M_{\text{pos}}}{N}} \exp\left(\mathrm{i}2\pi\theta_{\text{pos}}\frac{q - \overline{q}_l}{M_{\text{pos}}}\right) \sum_{s\in\mathbb{Z}} \delta(q - \overline{q}_l - sM_{\text{pos}}), \tag{2.56}$$

the states $|\overline{p}_n\rangle$ have the momentum representation

$$\langle p|\overline{p}_n\rangle := \sqrt{\frac{M_{\text{mom}}}{N}} \exp\left(-\mathrm{i}2\pi\theta_{\text{mom}}\frac{p-\overline{p}_n}{M_{\text{mom}}}\right)\sum_{r\in\mathbb{Z}} \delta(p-\overline{p}_n - rM_{\text{mom}}). \tag{2.57}$$

It is important to note that the periodicity along each lattice leaves only N independent choices of $\overline{q}_l$ or $\overline{p}_n$, respectively, which implies that $\mathcal{H}(\theta_{\text{pos}},\theta_{\text{mom}})$ is N-dimensional. In practice, we choose these $\overline{q}_l$ or $\overline{p}_n$ from the underlying torus $\big(\mathbb{R}/(q_{\text{min}}+M_{\text{pos}}\mathbb{Z})\big)\times\big(\mathbb{R}/(p_{\text{min}}+M_{\text{mom}}\mathbb{Z})\big)$, as indicated by the bar over the lattice indices. Finally, it can be shown that

$$\langle p|\overline{q}_l\rangle = \sum_{\overline{p}_n}\frac{1}{\sqrt{N}}\exp\left(-\frac{\mathrm{i}}{\hbar}\overline{q}_l\overline{p}_n\right)\langle p|\overline{p}_n\rangle\,, \tag{2.58a}$$

$$\langle q|\overline{p}_n\rangle = \sum_{\overline{q}_l}\frac{1}{\sqrt{N}}\exp\left(\frac{\mathrm{i}}{\hbar}\overline{p}_n\overline{q}_l\right)\langle q|\overline{q}_l\rangle\,, \tag{2.58b}$$

which means the basis states $|\overline{q}_l\rangle$ and $|\overline{p}_n\rangle$ are related by a lattice Fourier transformation. Expanding $\widehat{U}$ such that

$$\widehat{U}\,|\overline{q}_n\rangle = \sum_{\overline{q}_k}\langle\overline{q}_k|\widehat{U}|\overline{q}_n\rangle\,|\overline{q}_k\rangle\,, \tag{2.59}$$

$\langle\overline{q}_k|\widehat{U}|\overline{q}_n\rangle$ is the matrix representation of $\widehat{U}$ on the torus $\big(\mathbb{R}/(q_{\text{min}}+M_{\text{pos}}\mathbb{Z})\big)\times\big(\mathbb{R}/(p_{\text{min}}+M_{\text{mom}}\mathbb{Z})\big)$. For the standard map, one can show that $\widehat{U}$ commutes both with $\widehat{T}_{M_{\text{pos}}}$ and $\widehat{T}_{M_{\text{mom}}}$, if we choose $M_{\text{pos}} = M_{\text{mom}} = 1$ together with either (i) $\theta_{\text{pos}} = 0$ and N being even or (ii) $\theta_{\text{pos}} = 0.5$ and N being odd, see, e. g., Ref. [96]. The corresponding time-evolution operator on the torus is then given by [97]

$$\langle\overline{q}_k|\widehat{U}|\overline{q}_l\rangle = \exp\left(-\frac{\mathrm{i}}{\hbar}V(\overline{q}_k)\right)\sum_{\overline{p}_n}\frac{1}{N}\exp\left(\frac{\mathrm{i}}{\hbar}\overline{p}_n(\overline{q}_k-\overline{q}_l)\right)\exp\left(-\frac{\mathrm{i}}{\hbar}T(\overline{p}_n)\right) \tag{2.60}$$

when starting from Eqs. (2.32) and (2.56) and using lattice Fourier transforms, Eqs. (2.58). Alternatively, one can start from Eqs. (2.34) and (2.56) giving the equivalent result

$$\langle\overline{q}_k|\widehat{U}|\overline{q}_l\rangle = \frac{1}{N^{\frac{1}{2}}}e^{-\mathrm{i}\frac{\pi}{4}}\exp\left(\frac{\mathrm{i}}{\hbar}\left[\frac{(\overline{q}_l-\overline{q}_k)^2}{2}-V(\overline{q}_k)\right]\right), \tag{2.61}$$

which together with Eq. (2.15) gives

$$\langle\overline{q}_k|\widehat{U}|\overline{q}_l\rangle = \left(\frac{\mathrm{i}}{N}\left.\frac{\partial^2\mathcal{S}^U(q,q')}{\partial q\partial q'}\right|_{q=\overline{q}_l,q'=\overline{q}_k}\right)^{\frac{1}{2}}\exp\left(\frac{\mathrm{i}}{\hbar}\mathcal{S}^U(\overline{q}_l,\overline{q}_k)\right). \tag{2.62}$$

This expression has the advantage of being a discretized version of the semiclassical propagator, Eq. (2.35), known from semiclassical quantization [94, 98–100].

2.2.2. Quantum manifestations of the mixed phase space

In the following we examine basic manifestations of the mixed phase space in quantum mechanics by discussing the Husimi representation [101] for eigenstates $|n\rangle$ of the standard map on the torus.

To this end, we solve the eigenvalue equation for the time-evolution operator $\widehat{U}$ of the standard map on the torus,

$$\widehat{U}\,|n\rangle = \exp\left(\mathrm{i}\phi_n\right)|n\rangle\,. \tag{2.63}$$

Since $\widehat{U}$ is unitary ϕ_n are real eigenphases and the N eigenstates $|n\rangle$ form an orthonormal basis. In order to discuss the manifestations of classical phase-space structures, we project the eigenstates $|n\rangle$ onto coherent states $|\alpha(q,p)\rangle$ [102, 103], which have the position representation

$$\big\langle q'|\alpha(q,p)\big\rangle := \frac{1}{(\sqrt{2\pi}\Delta q)^{1/2}}\exp\left(-\frac{(q-q')^2}{4(\Delta q)^2}+\mathrm{i}\frac{p(q'-q)}{\hbar}\right) \tag{2.64}$$

with Δq being a free parameter, which is typically fixed at $\sqrt{\hbar}$. This allows for introducing the Husimi phase-space density

$$\underline{\mathrm{H}}_{|n\rangle}(q,p) = |\langle\alpha(q,p)|n\rangle|^2\,, \tag{2.65}$$

which represents the state $|n\rangle$ in phase space. In agreement with the semiclassical eigenfunction hypothesis [104–106] which predicts that quantum-mechanical eigenstates localize on phase-space structures that a typical orbit explores in the long-time limit, we can classify the eigenstates of a mixed system $\widehat{U}$ into regular and chaotic states, see, e. g., Fig. 2.5(b, c). For chaotic eigenstates this implies that their Husimi density is spread completely across a connected chaotic region, see, e.g., Fig. 2.5(c), while regular states localize on invariant regular tori $\mathcal{T}_m$, as, e. g., visulaized in Fig. 2.5(b).

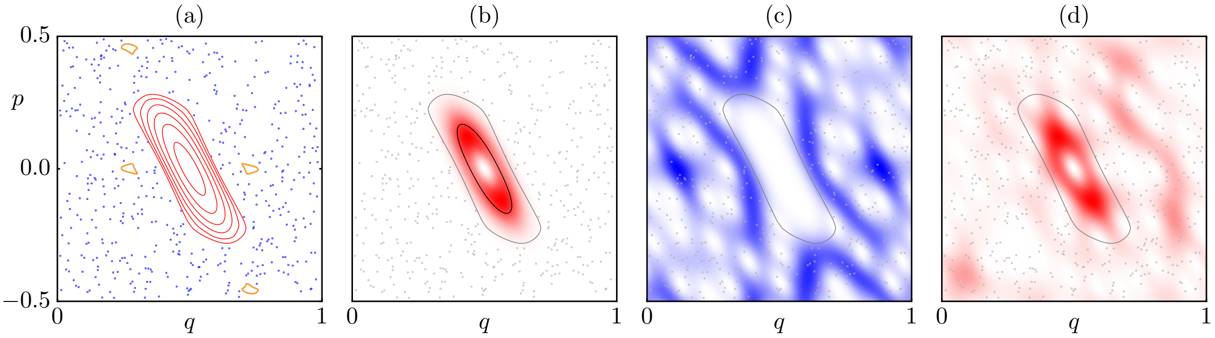

Figure 2.5.: Quantum manifestations of the mixed phase space in the eigenstates of the standard map on the torus for $\kappa = 2.9$, $h = 1/50$, and Bloch phases $(\theta_{\mathrm{pos}}, \theta_{\mathrm{mom}}) = (0, 0)$ in (b, c) and $(\theta_{\mathrm{pos}}, \theta_{\mathrm{mom}}) = (0, 0.19328582)$ in (d). (a) Red lines depict regular tori, orange lines a 4 : 1 resonance, and blue dots a chaotic orbit. (b–d) Same in gray. (b) The red density visualizes a regular state which localizes on a black quantizing torus. (c) The blue density visualizes a chaotic state. (d) The red density visualizes a hybrid state.

According to the Bohr–Sommerfeld quantization, Refs. [107–109], in its improved form including turning points, Refs. [15, 16, 19], these tori have a quantizing action

$$I_m := \frac{1}{2\pi} \oint_{\mathcal{T}_m} p(q)\mathrm{d}q = \hbar \left(m + \frac{1}{2} \right), \tag{2.66}$$

and can be labeled by the semiclassical quantum number m. Since $2\pi I_m$ is the area enclosed by the quantizing torus $\mathcal{T}_m$ it is possible to count the number of quantizing tori N_{reg} hosted by a regular region of size A_{reg}. With $\lfloor \cdot \rfloor$ being the floor function, we get

$$N_{\mathrm{reg}} = \left\lfloor \frac{A_{\mathrm{reg}}}{2\pi\hbar} + \frac{1}{2} \right\rfloor, \tag{2.67}$$

such that

$$m \in \{0, \ldots, N_{\mathrm{reg}} - 1\}. \tag{2.68}$$

It is important though to keep in mind that the semiclassical eigenfunction hypothesis only holds in the limit $\hbar \to 0$. For finite $\hbar$ tunneling effects between the regular and the chaotic region can occur, which implies that regular states always have tunneling admixtures of chaotic states and vice versa, see, e. g., Fig. 2.5(d) for an extreme example. For completeness we mention that in systems with high densities of chaotic states tunneling can cause regular states to disappear [56, 110], which is called flooding.

2.2.3. Quantum manifestations of partial barriers and non-linear resonance chains

In the following we illustrate the influence of partial transport barriers on the structure of chaotic states and demonstrate the hybridization effect between states of the regular region due to non-linear resonance chains. To this end, we exploit the standard map at $\kappa = 2.9$ and $\kappa = 3.5$.

As discussed in Sect. 2.1.3, Fig. 2.4, we expect the stable and unstable manifolds from the dissolving $4:1$ resonance to dominate the chaotic region for $\kappa = 2.9$ and $\kappa = 3.5$, respectively. More specifically the stable manifolds (blue lines in Figs. 2.6(a) and 2.7(a)) emanate from the four unstable points (black dots in Figs. 2.6(a) and 2.7(a)) and intersect with the unstable manifolds (red lines in Figs. 2.6(a) and 2.7(a)). This gives rise to eight heteroclinic points. These manifolds divide the chaotic region into the three chaotic subregions $\mathcal{C}_1$, $\mathcal{C}_2$, and $\mathcal{C}_3$. $\mathcal{C}_1$ denotes the chaotic phase-space region enclosed by the inner partial barrier. This excludes the regular phase-space region. $\mathcal{C}_2$ denotes the chaotic phase-space region between the inner and the outer partial barriers. $\mathcal{C}_3$ denotes the outer chaotic phase-space region, see Figs. 2.6(a) and 2.7(a). The closed curves constructed from these manifolds are not invariant under the classical mapping U, such that a flux Φ is exchanged across them for each application of U. As shown in Ref. [111, 112] these partial barriers act as barriers to quantum transport, if the classical flux Φ is more than ten times smaller than the effective Planck constant $\Phi \lesssim h/10$, while being quantum mechanically transparent for values of the effective Planck constant

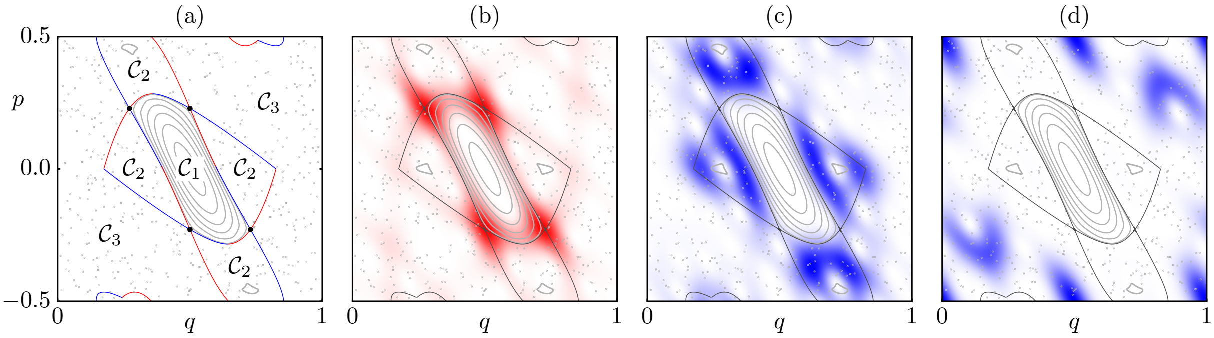

Figure 2.6.: Quantum manifestations of partial barriers for the standard map at $\kappa = 2.9$, $h = 1/50$, and $(\theta_{\text{pos}}, \theta_{\text{mom}}) = (0.0, 0.0)$. The background shows the classical phase space in gray. (a) Blue stable and red unstable manifolds emanating from the period four unstable orbit (black dots) are also shown in (b–d) in gray. Husimi-densities of chaotic states associated with the chaotic regions (b) $\mathcal{C}_1$ in red, (c) $\mathcal{C}_2$ in blue, and (d) $\mathcal{C}_3$ in blue.

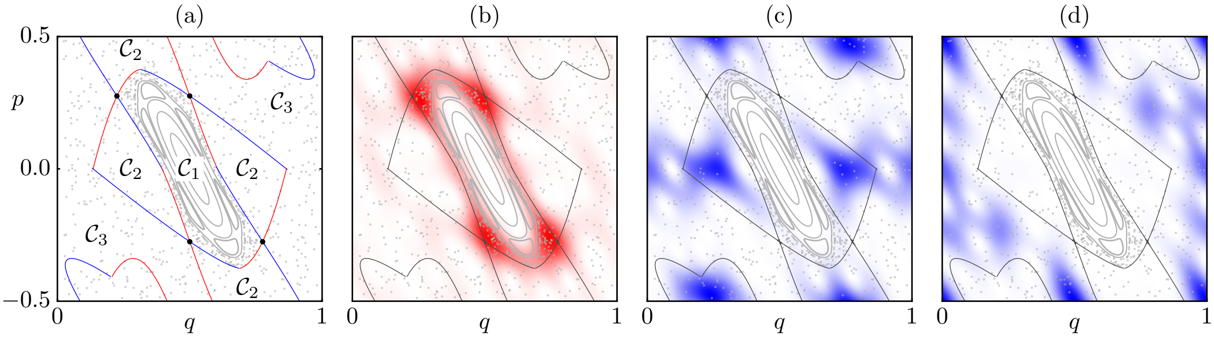

Figure 2.7.: Quantum manifestations of partial barriers for the standard map at $\kappa = 3.5$, $h = 1/50$, and $(\theta_{\text{pos}}, \theta_{\text{mom}}) = (0.0, 0.0)$. The background shows the classical phase space in gray. (a) Blue stable and red unstable manifolds emanating from the period four unstable orbit (black dots) are also shown in (b–d) in gray. Husimi-densities of chaotic states associated with the chaotic regions (b) $\mathcal{C}_1$ in red, (c) $\mathcal{C}_2$ in blue, and (d) $\mathcal{C}_3$ in blue.

being ten times larger than the flux $\Phi \gtrsim h \cdot 10$. In between these h-ranges a transition from barrierness to transparency can be observed, with the transition point being at $\Phi = h$.

For our tunneling investigation the values of the effective Planck constants are typically in $1/h \in [1, 100]$. Therefore h is much larger than the fluxes of the inside partial barriers for $\kappa = 2.9$ or $\kappa = 3.5$, respectively, i. e., the inner partial barrier is quantum mechanically closed. Since the chaotic region $\mathcal{C}_1$ is small and shows motion which sticks to the regular region, this effectively leads to a quantum enlargement of the area A_{reg} of the regular phase-space region. This effect is visualized for quasi-regular states (red) in Figs. 2.6(b) and 2.7(b), which localize on the chaotic region $\mathcal{C}_1$ inside the partial barrier for $\kappa = 2.9$ and $\kappa = 3.5$, respectively. The fluxes Φ across the outer partial barriers are comparable to h values in the regime $1/h \in [10, 100]$. Hence, also the outer partial barrier is quantum-mechanically active, which can be seen from chaotic states localizing in the regions $\mathcal{C}_2$ and $\mathcal{C}_3$, respectively, as visualized for $\kappa = 2.9$ in Figs. 2.6(c, d) and $\kappa = 3.5$ in Figs. 2.7(c, d).

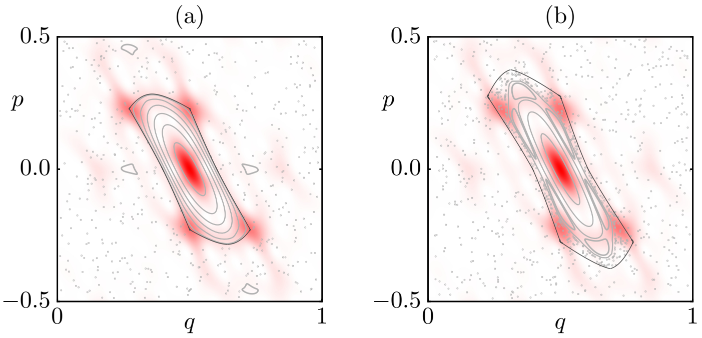

Figure 2.8.: Quantum manifestations of non-linear resonance chains for the standard map at (a) $\kappa = 2.9$, $h = 1/100$, $(\theta_{\text{pos}}, \theta_{\text{mom}}) = (0.0, 0.0)$ and (b) $\kappa = 3.5$, $h = 1/47$, $(\theta_{\text{pos}}, \theta_{\text{mom}}) = (0.5, 0.0)$. Classical phase space including partial barriers is shown in gray and Husimi densities of hybridized regular states are shown in red.

Finally let us examine the quantum-mechanical consequences of classical non-linear resonance chains. As can be seen from Fig. 2.3 the $r : s$ resonances $10 : 3$ or $6 : 2$ have the lowest resonance order r for the standard map at $\kappa = 2.9$ or $\kappa = 3.5$, respectively. As, e. g., shown in Ref. [59, 60] this leads to regular states which are a mixture of Bohr–Sommerfeld like states localizing on quantizing regular tori which differ by integer multiples of the resonance order r in their semiclassical quantum number m. This effect defines resonance-assisted tunneling [59, 60]. As a consequence, the corresponding regular state which predominantly localizes on the torus $\mathcal{T}_m$ with action I_m has resonance-assisted tunneling admixtures of Bohr–Sommerfeld like states localizing on tori $\mathcal{T}_{m+r}, \ldots, \mathcal{T}_{m+r\cdot n}$. This is visualized in Fig. 2.8(a) for $\kappa = 2.9$, where the depicted regular state localizes on the quantizing tori $\mathcal{T}_0$ and $\mathcal{T}_{10}$, while in Fig. 2.8(b) for $\kappa = 3.5$ the depicted regular state localizes on the quantizing tori $\mathcal{T}_0$ and $\mathcal{T}_6$. Note that in both cases the torus $\mathcal{T}_{m+r}$ of the excited state is not hosted inside the regular region, but exists on the effective extension of the regular region due to partial barriers.

In general the involved quantizing actions fulfill the relation

$$I_m < I_{m+r} < \cdots < I_{m+r\cdot n} \leq \frac{A_{\text{reg}}}{2\pi}, \tag{2.69}$$

with A_{reg} being the area of the regular phase-space region. This allows for defining a resonance-free regime in terms of h [64],

$$0 \leq \frac{1}{h} \leq \frac{m + r + \frac{1}{2}}{A_{\text{reg}}}, \tag{2.70}$$

for which resonance-assisted tunneling is irrelevant. Note that for the standard map this criterion is typically true when using the effective area A_{reg} enclosed by the inner partial barrier. Further note that Eq. (2.70) together with Fig. 2.3 explains why considering the standard map for $\kappa = 2.9$, where the lowest order $r : s$ resonance has the relatively high order $r = 10$, is an optimal choice for investigations of regular-to-chaotic tunneling. This choice guarantees a large resonance-free $1/h$-regime, where the additional complexity of resonance-assisted tunneling can be neglected.

3. Regular-to-chaotic tunneling rates

In this chapter we review the quantum-mechanical foundations of regular-to-chaotic tunneling. In the first part of this chapter we introduce regular-to-chaotic tunneling rates as decay rates of metastable states and explain their numerical determination for the standard map. In the second part, we discuss the influences of non-linear resonance chains and partial barriers on such numerical regular-to-chaotic tunneling rates, and comment on their connection to chaos-assisted tunneling [27, 28]. In the third part, we review the quantum-mechanical prediction of regular-to-chaotic tunneling rates with the help of fictitious integrable systems [62, 65]. Most topics of this chapter are covered in Refs. [62, 65]. However, we extend the material covered in these references by (i) a phenomenological discussion of partial barriers and their influence on regular-to-chaotic tunneling rates, (ii) discussing the Weyl quantization for fictitious integrable Hamiltonians, and (iii) introducing a generalization of the fictitious integrable system approach.

3.1. Regular-to-chaotic tunneling rates as decay rates of metastable states

It is intuitively clear that regular-to-chaotic tunneling refers to quantum-mechanical transitions between the regular and the chaotic phase-space region, which are forbidden in the classical system. Nevertheless, it is a difficult (if not impossible) task to capture this intuitive notion of regular-to-chaotic tunneling in a rigorous definition. This is due to Heisenberg's uncertainty principle, which forbids a precise simultaneous measurement of position and momentum, and thus, makes a quantum-mechanical definition of regular and chaotic phase-space regions impossible. Therefore we take an alternative view on the topic of regular-to-chaotic tunneling by considering physical quantities which are doubtlessly affected by regular-to-chaotic tunneling.

Traditionally, such a quantity is the phase splitting $\Delta\phi$ between even and odd states on parity related disjoint phase-space regions. This splitting is discussed in the context of chaos-assisted tunneling [27, 28] which is experimentally relevant, e. g., for billiards [48] and ratchet experiments with cold atoms [38–40]. The big disadvantage of tunnel splittings lies in the required symmetry, which might not be present in general non-integrable systems with a mixed phase space. For this reason, we chose to consider a different quantity in this thesis. Inspired by atoms, molecules, and optical microcavities, we characterize regular-to-chaotic tunneling by the decay rates γ of metastable states $|\psi\rangle$. These states localize on a regular phase-space region, and decay towards an unbound or leaky chaotic phase-space region, due to tunneling, see Fig. 3.1. As a consequence the system is open, such that metastable states have eigenphases $\phi + \mathrm{i}\gamma/2$ with an imaginary part. This imaginary part describes the exponential decay of the metastable state in time,

$$\|\psi(t)\|^2 = \|\psi(0)\|^2 \cdot \exp(-\gamma t). \tag{3.1}$$

Assuming that the transition from the regular to the chaotic phase-space region dominates over transport through the chaotic phase-space region we call this decay rate γ a regular-to-chaotic tunneling rate.

3.1.1. Numerical regular-to-chaotic tunneling rates for the standard map

In order to obtain a regular-to-chaotic tunneling rate γ for the standard map, we introduce an absorber in the chaotic region, as sketched by the gray regions in Fig. 3.1. This is inspired by numerical computations of decay rates for metastable states in molecular physics [113] or the leaky region in optical microcavities. To this end, we consider the time-evolution operator of the standard map $\langle q_k|\widehat{U}|q_l\rangle$ on a cylinder $\mathbb{R} \times \big(\mathbb{R}/(-0.5+\mathbb{Z})\big)$, Eq. (2.52), with $q_k, q_l \in [q_{\min}, q_{\max}]$. The complementary region $\mathcal{R}_{\text{abs}} := (-\infty, q_{\min}) \cup (q_{\max}, \infty)$ is an absorber which ignores transition-matrix elements from and to these lattice points. With $\widehat{P}_{\text{abs}}$ being a projector onto the absorbing region, we can write the time-evolution operator of the open system as

$$\widehat{U}_{\text{open}} = (\mathbb{1} - \widehat{P}_{\text{abs}})\widehat{U}(\mathbb{1} - \widehat{P}_{\text{abs}}). \tag{3.2}$$

Note that typically absorbers require a smooth transition between the non-absorbing and the absorbing reqion in order to avoid quantum reflections on waves traveling towards the absorbing region [114, 115]. In our case this is unnecessary, because regular-to-chaotic tunneling dominates γ such that the subsequent absorption process in the chaotic region is expected to induce only small fluctuations on

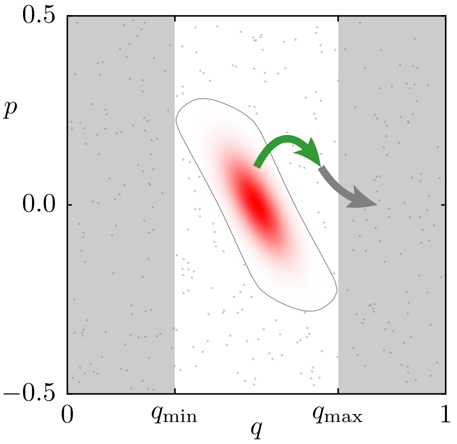

Figure 3.1.: Phase space of the standard map for $\kappa = 2.9$ (gray dots and lines) showing a (gray) absorbing region and a (red) Husimi density ($1/h = 60$) of a metastable state. Arrows indicate regular-to-chaotic tunneling (green) and chaotic transport towards the absorber (gray).

the tunneling rate, see arrows in Fig. 3.1.

The above absorbers give a finite-dimensional, sub-unitary operator $\widehat{U}_{\text{open}}$ which allows for a numerical solution of their eigenvalue equation,

$$\widehat{U}_{\text{open}} |m\rangle = (\mathbb{1} - \widehat{P}_{\text{abs}})\widehat{U}(\mathbb{1} - \widehat{P}_{\text{abs}}) |m\rangle = \lambda_m |m\rangle = \exp\left(\mathrm{i}\left[\phi_m + \mathrm{i}\frac{\gamma_m}{2}\right]\right) |m\rangle . \tag{3.3}$$

From the eigenvalue we extract γ_m according to

$$\gamma_m = -2\log|\lambda_m|, \tag{3.4}$$

which can be shown to describe the decay of the metastable state m,

$$\| \, |m(t=n)\rangle \, \|^2 = \| \, |m(t=0)\rangle \, \|^2 \cdot \exp\left(-\gamma_m \cdot n\right). \tag{3.5}$$

Since the absorber is localized in the chaotic part of phase space one can expect that the regular states of the closed system are only perturbed on the order of magnitude by which they couple to the chaotic region. Hence, it is possible to order the index m such that the states with index $m \leq \lfloor A_{\text{reg}}/(2\pi\hbar) - 1/2 \rfloor$ predominantly localize on the tori $\mathcal{T}_m$ with quantizing action I_m, Eq. (2.66), inside the regular region. As described above, we compute regular-to-chaotic tunneling rates for the standard map at $\kappa = 2.9$ as a function of $\hbar$. Since we consider a cylindric phase space, we are free to chose the effective Planck constant $2\pi\hbar$. The Bloch phase θ_{mom} is fixed according to

$$\theta_{\text{mom}} = \left(\frac{M_{\text{mom}}}{2\pi\hbar}\left(\frac{q_{\min} + q_{\max}}{2}\right) - \frac{1}{2}\left\lfloor \frac{M_{\text{mom}}}{2\pi\hbar}(q_{\max} - q_{\min}) \right\rfloor\right) \quad \text{mod } M_{\text{mom}}, \tag{3.6}$$

which ensures the symmetric configuration of the position lattice, for which the maximal number of sites is in $(q_{\min}, q_{\max})$.

Figure 3.2 shows numerically obtained regular-to-chaotic tunneling rates for $m = 0, 1, 2, 3$ in their resonance-free h-regime, Eq. (2.70). Here, the absorber is chosen tangential to the last torus of the regular region, see gray regions of insets in Fig. 3.2, with $q_{\min} = 0.2843$ and $q_{\max} = 1 - q_{\min}$. We observe that the tunneling rates γ_m increase for larger semiclassical quantum numbers m. This corresponds to the intuition that regular-to-chaotic tunneling should be faster for metastable states of the regular phase-space region, which localize closer towards the regular–chaotic border region. Furthermore, a clear exponential h-scaling of the tunneling rates according to

$$\gamma_m = \exp\left(-\frac{B_m}{\hbar}\right) \tag{3.7}$$

is observed. This behavior meets the semiclassical expectation that tunneling should get harder as we approach the semiclassical limit, $h \to 0$. This exponential h-scaling, of regular-to-chaotic tunneling rates has often been observed for the resonance-free regime [40, 42, 43, 47, 50, 65], but lacks a theoretical explanation so far. Among the goals of this thesis it is one task to provide a semiclassical prediction for regular-to-chaotic tunneling rates and allow for a semiclassical understanding of this

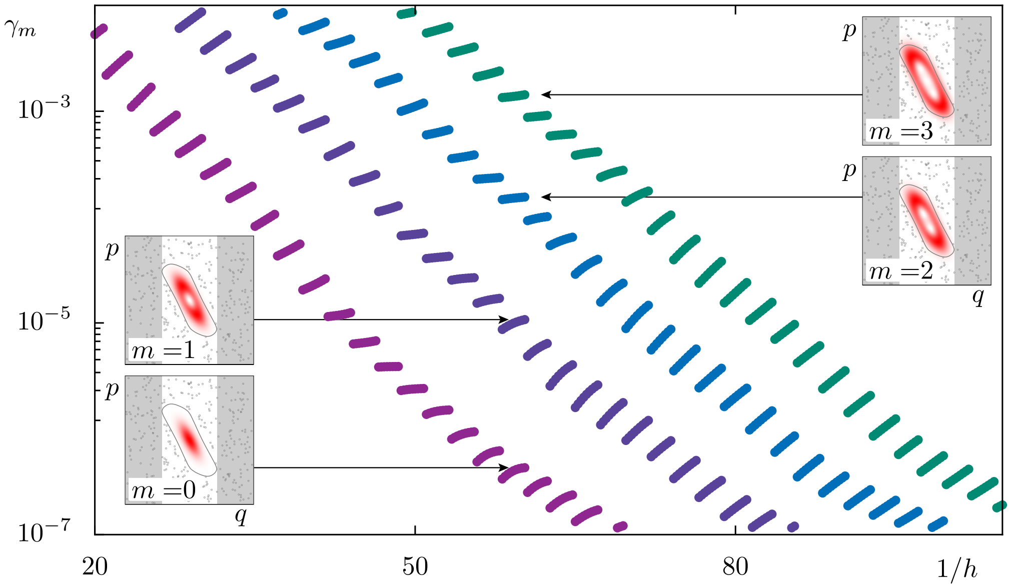

Figure 3.2.: Regular-to-chaotic tunneling rates (dots) versus inverse effective Planck constant for metastable states in the standard map at $\kappa = 2.9$ (parameters described in the text). The insets show corresponding Husimi densities (red, $1/h = 60$), absorbing regions (gray), and the classical phase space (gray dots and lines).

exponential behavior.

Another, less important feature of the numerical tunneling rates are so-called quantization jumps, see Fig. 3.2. They occur, when $1/h$ takes the values

$$\frac{1}{h} = \frac{N}{M_{\mathrm{mom}}(q_{\mathrm{max}} - q_{\mathrm{min}})} \quad \text{with } N \in \mathbb{N}, \tag{3.8}$$

for which $\widehat{U}_{\mathrm{open}}$ has to be quantized with $N+1$ instead of N lattice points. These events are evenly-spaced in $1/h$ with distance $1/[M_{\mathrm{mom}}(q_{\mathrm{max}} - q_{\mathrm{min}})] \approx 2.318$. Note that these quantization jumps did not occur in Refs. [62, 64, 65, 116] since there the chosen resolution in $1/h$ is not fine enough.

3.2. Discussion of regular-to-chaotic tunneling rates

Even though the main objective of this thesis is a semiclassical understanding of regular-to-chaotic tunneling rates in the resonance-free regime, as previously presented in Sect. 3.1.1, it is illuminating to shed light on tunneling rates in a wider context. To this end, we discuss the influence of non-linear resonance chains and the role of partial barriers in the upcoming section, and make a connection to phase splittings $\Delta\phi$ of chaos-assisted tunneling.

3.2.1. Regular-to-chaotic tunneling rates and non-linear resonance chains

In order to illustrate the influence of non-linear resonance chains on regular-to-chaotic tunneling rates Fig. 3.3 presents the numerically determined tunneling rate γ_0 on a larger range of Planck's constant $20 \lesssim 1/h \lesssim 125$. In the resonance-free regime, $20 \lesssim 1/h \lesssim 75$, we observe the exponential decrease of the regular-to-chaotic tunneling rate γ_0 which was previously discussed in Fig. 3.2. This exponential decrease of γ_0 stops in the resonance-assisted tunneling regime, $75 \lesssim 1/h$, where γ_0 shows a plateau and a peak.

As worked out in Ref. [64] the regular-to-chaotic tunneling rate in the resonance-free regime can be understood in terms of a direct probability transfer from a metastable state localizing on the quantizing torus $\mathcal{T}_0$ to the chaotic region. This is called direct regular-to-chaotic tunneling. When entering the regime of resonance-assisted tunneling, an additional decay channel emerges. Similar to Fig. 2.8 the metastable state which localizes on the quantizing torus $\mathcal{T}_0$ has admixtures of a Bohr–Sommerfeld like state which localizes on the quantizing torus $\mathcal{T}_{10}$ due to the $10:3$ resonance. From there the metastable state decays such that this new decay channel eventually dominates over direct regular-to-chaotic tunneling. Remarkably, the regime for which the decay of the metastable state is dominated by resonance-assisted tunneling starts at $1/h \approx 75$. Not only is this before the tenth regular state starts to exist in the regular region ($1/h \approx 95$ as predicted from, Eq. (2.70) with $A_{\text{reg}} = 0.11$), but even before the tenth regular state exists on the union with the chaotic region $\mathcal{C}_1$, Fig. 2.6, which is confined by the inner partial barrier ($1/h \approx 91$ as predicted from, Eq. (2.70) with $A_{\text{reg}} = 0.115$).

Please note that typically direct regular-to-chaotic tunneling rates in the resonance-free regime are

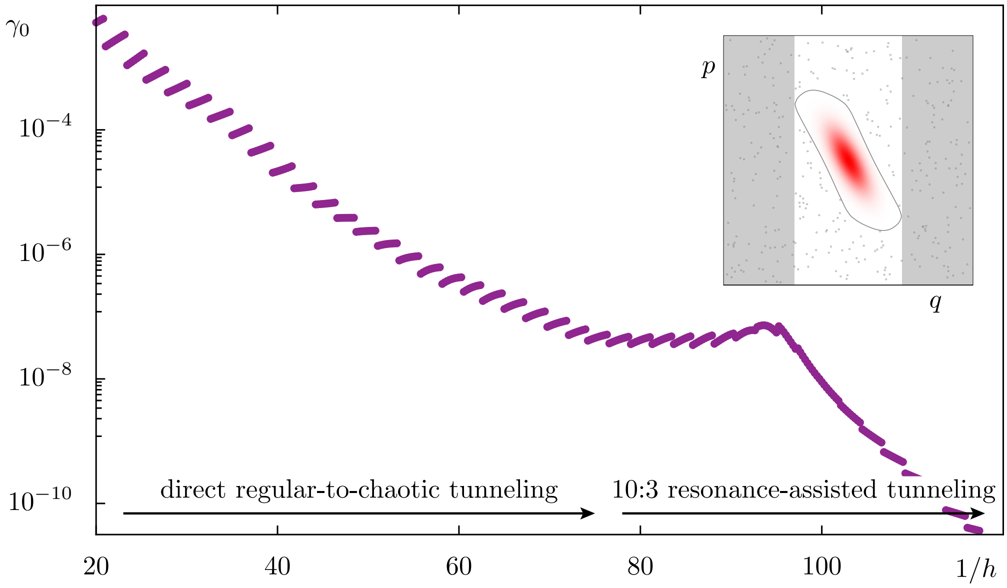

Figure 3.3.: Regular-to-chaotic tunneling rate γ_0 of the standard map at $\kappa = 2.9$ versus the inverse effective Planck constant $1/h$. The inset shows the Husimi representation (red, $1/h = 60$) of the corresponding metastable state, (gray) absorbing regions, and the classical phase space (gray dots and lines).

several orders of magnitude larger than tunneling rates in the regime of resonance-assisted tunneling. Therefore direct regular-to-chaotic tunneling is experimentally more relevant, which justifies the focus of this thesis on direct regular-to-chaotic tunneling rates.

3.2.2. Regular-to-chaotic tunneling rates and partial barriers

In the following the influence of partial barriers on regular-to-chaotic tunneling rates is investigated numerically. Before starting, we recall Fig. 2.6 which shows how the chaotic phase-space region of the standard map is divided into three weakly coupled subregions $\mathcal{C}_1$, $\mathcal{C}_2$, and $\mathcal{C}_3$, with classical fluxes Φ_{12} between $\mathcal{C}_1$ and $\mathcal{C}_2$ and Φ_{23} between $\mathcal{C}_2$ and $\mathcal{C}_3$. As worked out in ref. [111, 112] a partial barrier opens up for $1/h$ increasing in $[1/(10\Phi), 10/\Phi]$ with the transition point at $h = \Phi$. Since Φ_{12} is extremely small, the partial barrier separating the chaotic phase-space regions $\mathcal{C}_1$ and $\mathcal{C}_2$, as introduced in Fig. 2.6, is quantum mechanically closed in our numerical studies. Since the confined area ($A_{\mathcal{C}_1} \approx 0.005$) of the region $\mathcal{C}_1$ is very small too, we consider $\mathcal{C}_1$ as an extension of the regular region for the relevant values of Planck's constant, $20 \lesssim 1/h \lesssim 125$. Furthermore, with $\Phi_{23} \approx 0.0126$ [111, 112], the transition point of the partial barrier between the chaotic phase-space regions $\mathcal{C}_2$ and $\mathcal{C}_3$, as introduced in Fig. 2.6, is at $1/h \approx 80$. Hence, also the outer partial barrier is quantum mechanically active in the considered regime of Planck's constant, $20 \lesssim 1/h \lesssim 125$.

We start our discussion with Fig. 3.4, which shows the tunneling rate γ_0 of the standard map at

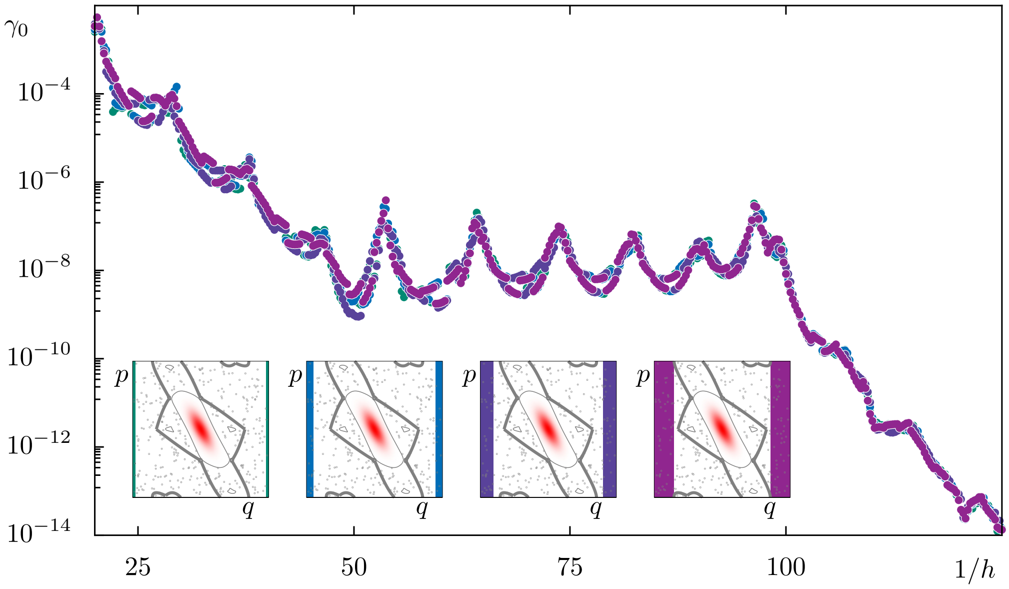

Figure 3.4.: Numerically determined regular-to-chaotic tunneling rates γ_0 of the standard map at $\kappa = 2.9$ are shown as a function of the inverse effective Planck constant $1/h$ by dots for different locations of the absorber $q_{\min} = 0.0$, 0.04858777, 0.09717554, and 0.14576331. These locations are depicted in the inset by shaded regions colored corresponding to the data. The insets further show the (red) Husimi representation of the corresponding metastable state and the classical phase space (gray dots and lines).

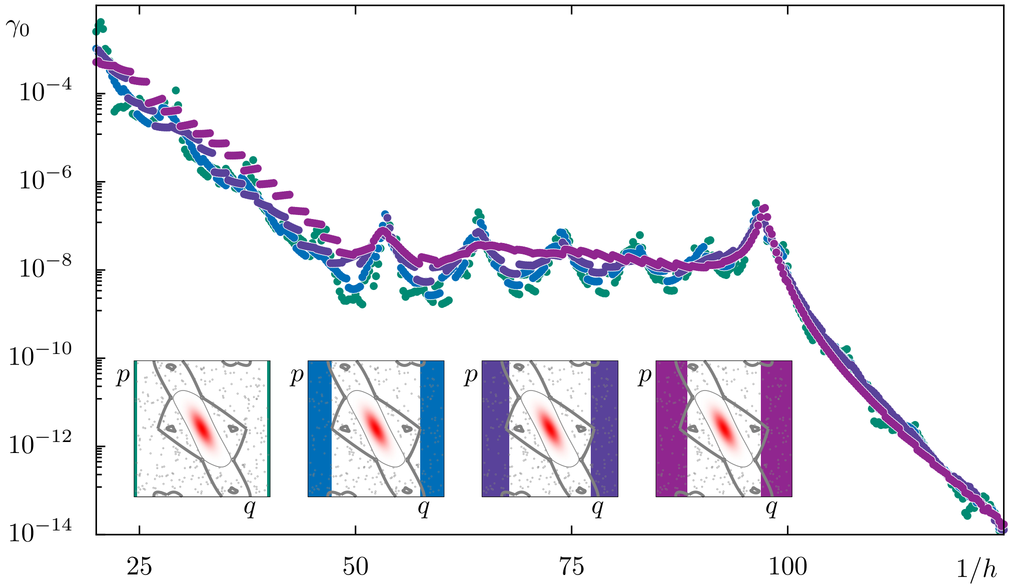

Figure 3.5.: Numerically determined regular-to-chaotic tunneling rates γ_0 of the standard map at $\kappa = 2.9$ are shown as a function of the inverse effective Planck constant $1/h$ by dots for different locations of the absorber $q_{\min} = 0.0, 0.17384221, 0.2019211, 0.23$. These locations are depicted in the inset by shaded regions colored corresponding to the data. The insets further show the (red) Husimi representation of the corresponding metastable state and the classical phase space (gray dots and lines).

$\kappa = 2.9$ on the cylinder $\mathbb{R} \times \big(\mathbb{R}/(-0.5 + \mathbb{Z})\big)$ for absorbing regions, which are entirely located in the chaotic region outside the outer partial barrier ($q_{\min} = 0.0, 0.04858777, 0.09717554$, and 0.14576331 and $q_{\max} = 1 - q_{\min}$). Shifting the absorber in that region leaves the tunneling rate γ_0 invariant up to small variations. On top of the the exponential h-scaling of the tunneling rate in the regime $20 \lesssim 1/h \lesssim 50$ and the plateau and peak of the $10:3$ resonance in the regime $50 \lesssim 1/h \lesssim 125$, the tunneling rate γ_0 shows fluctuations which produce peak-like structures, with peak spacings in the inverse effective Planck constant ≈ 10. The origin of these peaks is not entirely understood. However, a connection to resonance-assisted tunneling via the $4:1$ resonance mediated by the partial barrier is likely [117].

We proceed with Fig. 3.5 which presents the numerical tunneling rate γ_0 for absorbing regions which intersect the outer partial barrier and penetrate into the chaotic subregion $\mathcal{C}_2$, but at the same time do not affect the remnants of the $4:1$ resonance ($q_{\min} = 0.17384221, 0.2019211, 0.23$ with $q_{\max} = 1 - q_{\min}$). As can be seen in Fig. 3.5, the tunneling rate γ_0 still keeps the same order of magnitude. However, the peak-like fluctuations of Fig. 3.4 are washed out the more the absorber is shifted towards the $4:1$ resonance.

We finalize our phenomenological investigation by considering Fig. 3.6, which shows numerically obtained tunneling rates for absorbers ($q_{\min} = 0.271286$ and $q_{\min} = 0.2843$ with $q_{\max} = 1 - q_{\min}$) which are tangential to the inner partial barrier and the last torus of the regular region, respectively. In contrast to the tunneling rates obtained for $q_{\min} = 0.0$, $q_{\max} = 1.0$ (gray data in Fig. 3.6) the

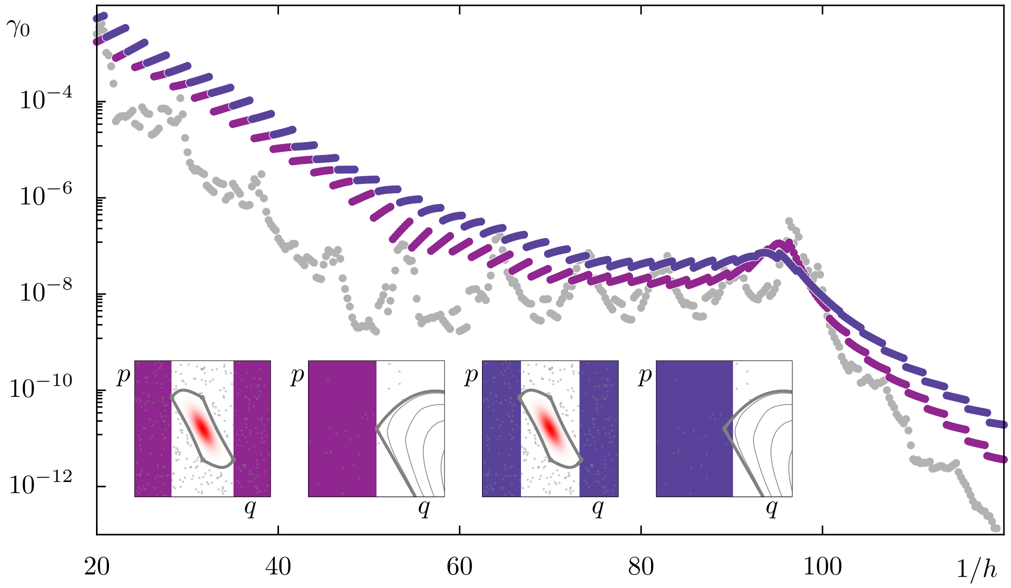

Figure 3.6.: Numerically determined regular-to-chaotic tunneling rates γ_0 of the standard map at $\kappa = 2.9$ are shown as a function of the inverse effective Planck constant $1/h$ by dots for different locations of the absorber $q_{\text{min}} = 0.0$ (gray data) and $q_{\text{min}} = 0.271286$ and 0.2843. The last two locations are depicted in the inset by shaded regions colored corresponding to the data. The insets further show the (red) Husimi representation of the corresponding metastable state and the classical phase space (gray dots and lines).

tunneling rates from absorbers close to the regular region are up to four orders of magnitude larger.

We summarize this discussion with the following conclusions: (1) The location of the absorber has a profound impact on the regular-to-chaotic tunneling rate γ_m. (2) The tunneling rate seems stable for absorbing regions beyond the last partial barrier. In this thesis we focus on experimental situations for which the absorber is close to the regular region, i. e., the complexity of tunneling rates induced by the hierarchical region is ignored and has to be investigated in the future.

3.2.3. Regular-to-chaotic tunneling rates and chaos-assisted tunneling

In this section, we make a connection between regular-to-chaotic tunneling rates γ and the traditionally established phase splittings $\Delta\phi$ of chaos-assisted tunneling. In chaos-assisted tunneling two parity related regular phase-space regions r, l are separated by a chaotic phase-space region. Due to symmetry, these two regular regions host equivalent Bohr–Sommerfeld like states $|r\rangle$ and $|l\rangle$. Here, we restrict the presentation to one such state per region. They are related by the parity operator $\hat{\mathbb{P}}$, according to $|l\rangle = \hat{\mathbb{P}}\,|r\rangle$ and $|r\rangle = \hat{\mathbb{P}}\,|l\rangle$. Due to symmetry, the eigenstates of such a system are the symmetric and antisymmetric combinations $|\pm\rangle = (|r\rangle \pm |l\rangle)/\sqrt{2}$, which have the eigenphases ϕ_+ and ϕ_-. Due to tunneling, these eigenphases are not degenerate and have a small splitting $\Delta\phi = |\phi_- - \phi_+|$, which determines the oscillation period $T = 2\pi/\Delta\phi$ of a complete probability transfer from the regular phase-space region r to the regular phase-space region l and back ($|r\rangle \to |l\rangle \to |r\rangle$).

For the standard map, a determination of such splittings $\Delta\phi$ is possible by using its quantization on the cylinders $\big(\mathbb{R}/(q_{\text{min}} + M_{\text{pos}}\mathbb{Z})\big) \times \mathbb{R}$ with $M_{\text{pos}} = 2$ where the phase space hosts two parity-related regular regions. Equivalently, one can consider the quantization of the standard map on the cylinder $\big(\mathbb{R}/(q_{\text{min}} + M_{\text{pos}}\mathbb{Z})\big) \times \mathbb{R}$ with $M_{\text{pos}} = 1$ and measure the splitting between regular states with the same semiclassical quantum number m on the regular region for the two Bloch-phase configurations $\theta_{\text{mom}} = 0.0, 0.5$ [72], see gray crosses in Fig. (3.7) for $\Delta\phi_0$

According to Ref. [65] regular-to-chaotic tunneling rates γ and chaos-assisted tunnel splittings $\Delta\phi$ are related according to

$$\langle \Delta\phi_m \rangle = \gamma_m. \tag{3.9}$$

Here, $\langle\cdot\rangle$ denotes an ensemble average which assumes random-matrix statistics for the states associated with the chaotic phase-space region. For the standard map the question whether Eq. (3.9) is applicable arises immediately. This is due to partial barriers in the chaotic region, which on the one hand violate the random matrix assumption behind Eq. (3.9) and on the other hand give tunneling rates which depend on the absorber positions $q_{\text{min}}, q_{\text{max}}$. At least numerically we observe that (3.9) is roughly fulfilled, when using the tunneling rates γ_0 obtained with absorber positions beyond the last partial barrier, e. g., $q_{\text{min}} = 0.0, q_{\text{max}} = 1.0$, see purple dots in Fig. (3.7) and comparing them to $\Delta\phi_0$.

In contrast to the statement made in Ref. [65] not only phase splittings but also the tunneling rates can be strongly fluctuating quantities, see Fig. (3.7). For chaos-assisted phase splittings these fluctuations can be understood from avoided crossings between regular states with spectrally fluctu-

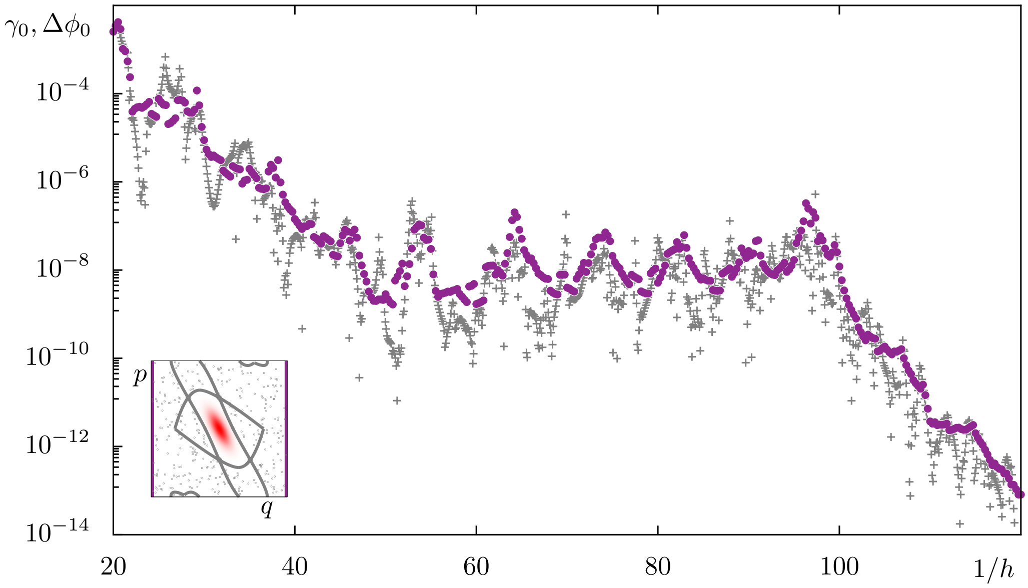

Figure 3.7.: Comparison of regular-to-chaotic the tunneling rates γ_0 for $q_{\text{min}} = 0.0$ and $q_{\text{max}} = 1.0$ (magenta dots) and chaos-assisted phase splittings $\Delta\phi_0$ (gray crosses) of the standard map at $\kappa = 2.9$ as a function of the inverse effective Planck constant $1/h$. The inset shows the (red) Husimi representation of the corresponding regular state and the classical phase space (gray dots and lines) with (magenta) absorbing regions.

ating chaotic states [27, 28]. We conjecture that a similar mechanism causes the fluctuations of the tunneling rates.

3.3. Predicting regular-to-chaotic tunneling rates using an improved fictitious integrable system approach

In this section a quantum-mechanical prediction for regular-to-chaotic tunneling rates γ_m is derived, resulting in an improved version of the fictitious integrable system approach of Refs. [62, 65]. Its application to the standard map is demonstrated.

3.3.1. Derivation of the improved fictitious integrable system approach

In the following we derive a prediction of regular-to-chaotic tunneling rates. While keeping the basic idea of Refs. [62, 65] the presented derivation results in a prediction which can account for the dependence of regular-to-chaotic tunneling rates on the absorbing phase-space region $\mathcal{R}_{\text{abs}}$. Furthermore, the presented derivation points out the errors which occur in approximating numerical regular-to-chaotic tunneling rates γ_m by fictitious integrable system predictions.

The starting point of our derivation is Eq. (3.5) for $n = 1$,

$$\langle m|m\rangle \cdot \exp\left(-\gamma_m\right) = \langle m|\widehat{U}^{\dagger}_{\text{open}}\widehat{U}_{\text{open}}|m\rangle, \tag{3.10}$$

which we consider as a definition of the tunneling rate γ_m. Here, $|m\rangle$ is the metastable eigenstate of the open system $\widehat{U}_{\text{open}}$, which localizes on the torus of U corresponding to the quantizing action I_m. We recall the definition of $\widehat{U}_{\text{open}}$, Eq. (3.2), which is obtained from sandwiching the unitary time-evolution operator $\widehat{U}$ of the closed non-integrable system between the projector $(\mathbb{1} - \widehat{P}_{\text{abs}})$. Here, $\widehat{P}_{\text{abs}}$ is a projector on the absorbing region $\mathcal{R}_{\text{abs}}$.

The derivation proceeds by using the unitarity of $\widehat{U}$, which gives

$$\langle m|m\rangle = \langle m|\widehat{U}^{\dagger}\widehat{U}|m\rangle. \tag{3.11}$$

Subtracting Eq. (3.10) from Eq. (3.11) we get

$$\langle m|m\rangle\left(1 - \exp\left(-\gamma_m\right)\right) = \langle m|\widehat{U}^{\dagger}\widehat{U}|m\rangle - \langle m|(\mathbb{1} - \widehat{P}_{\text{abs}})\widehat{U}^{\dagger}(\mathbb{1} - \widehat{P}_{\text{abs}})\widehat{U}(\mathbb{1} - \widehat{P}_{\text{abs}})|m\rangle \tag{3.12}$$

where the projector properties $(\mathbb{1} - \widehat{P}_{\text{abs}}) = (\mathbb{1} - \widehat{P}_{\text{abs}})^2$ and $(\mathbb{1} - \widehat{P}_{\text{abs}}) = (\mathbb{1} - \widehat{P}_{\text{abs}})^{\dagger}$ were used. Since $|m\rangle$ is an eigenstate of $\widehat{U}_{\text{open}}$, Eq. (3.2), we conclude that

$$(\mathbb{1} - \widehat{P}_{\text{abs}})\,|m\rangle = |m\rangle\,, \tag{3.13}$$

such that $|m\rangle$ can be normalized

$$\langle m|m\rangle = 1. \tag{3.14}$$

Combining Eqs. (3.12), (3.13), and (3.14) with $\widehat{P}_{\text{abs}} = \widehat{P}^2_{\text{abs}}$ and $\widehat{P}_{\text{abs}} = \widehat{P}^{\dagger}_{\text{abs}}$ gives

$$1 - \exp(-\gamma_m) = \|\widehat{P}_{\text{abs}}\widehat{U}\,|m\rangle\,\|^2, \tag{3.15}$$

which assuming that $\gamma_m \ll 1$ is

$$\gamma_m = \|\widehat{P}_{\text{abs}}\widehat{U}\,|m\rangle\,\|^2. \tag{3.16}$$

This relation allows for interpreting the tunneling rate as the probability transfer from the normalized metastable state $|m\rangle$ into the absorber, via the time-evolution operator $\widehat{U}$ of the closed system. For small tunneling rates, this relation is exact. If a semiclassical theory for metastable eigenstates of the open system $\widehat{U}_{\text{open}}$ was available, Eq. (3.16) would provide an ideal starting point for further semiclassical investigations. However, to the best knowledge of this thesis' author, such a theory does not exist. Therefore, we proceed by approximating the metastable state $|m\rangle$ by an approximate regular basis state $\left|\psi^m_{\text{reg}}\right\rangle$ in the following. To this end we define the difference

$$|d\rangle := |m\rangle - \left|\psi^m_{\text{reg}}\right\rangle \tag{3.17}$$

between the metastable state $|m\rangle$ and the regular basis state $\left|\psi^m_{\text{reg}}\right\rangle$, and obtain

$$\gamma_m = \|\widehat{P}_{\text{abs}}\widehat{U}\,\left|\psi^m_{\text{reg}}\right\rangle\|^2 + \langle\psi^m_{\text{reg}}|\widehat{U}^{\dagger}\widehat{P}_{\text{abs}}\widehat{U}|d\rangle + \langle d|\widehat{U}^{\dagger}\widehat{P}_{\text{abs}}\widehat{U}|\psi^m_{\text{reg}}\rangle + \langle d|\widehat{U}^{\dagger}\widehat{P}_{\text{abs}}\widehat{U}|d\rangle. \tag{3.18}$$

This concludes our derivation. Our final quantum-mechanical prediction for regular-to-chaotic tunneling rates γ_m is given by

$$\gamma_m = \|\widehat{P}_{\text{abs}}\widehat{U}\,\left|\psi^m_{\text{reg}}\right\rangle\|^2. \tag{3.19}$$

It is valid up to the error terms provided by

$$\Delta\gamma_m := \langle\psi^m_{\text{reg}}|\widehat{U}^{\dagger}\widehat{P}_{\text{abs}}\widehat{U}|d\rangle + \langle d|\widehat{U}^{\dagger}\widehat{P}_{\text{abs}}\widehat{U}|\psi^m_{\text{reg}}\rangle + \langle d|\widehat{U}^{\dagger}\widehat{P}_{\text{abs}}\widehat{U}|d\rangle. \tag{3.20}$$

Using the triangle inequality, together with the Cauchy–Schwarz inequality, the operator norms $\|\widehat{P}_{\text{abs}}\| = 1$, $\|\widehat{U}\| = 1$, and the normalization $\left\langle\psi^m_{\text{reg}}|\psi^m_{\text{reg}}\right\rangle = 1$ we can provide the error bound

$$|\Delta\gamma_m| \leq 2\|d\| + \|d\|^2, \tag{3.21}$$

which shows that the validity of prediction (3.19) is guaranteed, for regular basis states which approximate the metastable eigenstate on the order of the tunneling rate

$$\|d\| = \| \left|m\right\rangle - \left|\psi_{\text{reg}}^{m}\right\rangle \| \lesssim \mathcal{O}(\gamma_m). \tag{3.22}$$

Note that constructing a regular basis state which approximates the metastable eigenstate of the open system on the order of the tunneling rate is an extremely challenging task. Hence, condition (3.22) is typically not fulfilled in practical implementations of Eq. (3.19), and thus, only serves as a theoretical argument in the derivation of Eq. (3.19) which is not further exploited in this thesis.

If we assume that the transport through the chaotic phase-space region is fast, i. e., there are no significant partial barriers, we can additionally approximate the projector $\widehat{P}_{\text{abs}}$ on the absorbing region by the projector $\widehat{P}_{\text{ch}}$ on the whole chaotic phase-space region. This results in the prediction of the fictitious integrable system approach,

$$\gamma_m = \|\widehat{P}_{\text{ch}}\widehat{U}\left|\psi_{\text{reg}}^{m}\right\rangle\|^2, \tag{3.23}$$

as previously introduced in Refs. [62, 65]. Note that the practical advantage of Eq. (3.19) over Eq. (3.23) lies in its ability to predict regular-to-chaotic tunneling rates γ_m for varying absorbing regions $\mathcal{R}_{\text{abs}}$. This is important, if regular-to-chaotic tunneling rates depend sensitively on the absorbing region, as, e. g., discussed in Sect. 3.2.2 on partial barriers. On the other hand, the advantage of Eq. (3.23) is its intuitive understanding of regular-to-chaotic tunneling as the probability transfer from a state of the regular phase-space region to the chaotic phase-space region.

Having arrived at this result, the remaining challenge lies in providing the regular basis states $\left|\psi_{\text{reg}}^{m}\right\rangle$. As demonstrated in Refs. [62, 65] such basis states can be provided by using the eigenstates of a fictitious integrable system $H_{\text{reg}}(q,p)$. The details of this procedure, are described in Sects. 3.3.2 and 3.3.3 with results for the standard map presented in Sect. 3.3.4. However, before describing these details, we work out an alternative to Eq. (3.19), which allows for WKB-like predictions for regular-to-chaotic tunneling rates.

Towards a WKB-like prediction for regular-to-chaotic tunneling rates

The following derivation aims at deriving a quantum-mechanical prediction for regular-to-chaotic tunneling rates, which semiclassically give WKB-like predictions using the regular basis state $\left|\psi_{\text{reg}}^{m}\right\rangle$. It has been worked out in collaboration with Martin Körber, who pointed out that alternatively to solving the eigenvalue equation, Eq. (3.3), for the numerical determination of regular-to-chaotic tunneling rates, it is possible to solve the eigenvalue equation

$$\widehat{U}(\mathbb{1} - \widehat{P}_{\text{abs}})\left|\underline{m}\right\rangle = \lambda_m \left|\underline{m}\right\rangle = \exp\left(\mathrm{i}\left[\phi_m + \mathrm{i}\frac{\gamma_m}{2}\right]\right)\left|\underline{m}\right\rangle. \tag{3.24}$$

Applying $(\mathbb{1} - \widehat{P}_{\text{abs}})$ from the left and using that $(\mathbb{1} - \widehat{P}_{\text{abs}}) = (\mathbb{1} - \widehat{P}_{\text{abs}})^2$, we recover Eq. (3.3). In that we verify that the operators $\widehat{U}(\mathbb{1} - \widehat{P}_{\text{abs}})$ and $(\mathbb{1} - \widehat{P}_{\text{abs}})\widehat{U}(\mathbb{1} - \widehat{P}_{\text{abs}})$ have the same spectrum [118], while the corresponding metastable eigenstates $\left|\underline{m}\right\rangle$ and $\left|m\right\rangle$, with $\left|m\right\rangle$ as in Eq. (3.3), are related according to

$$|m\rangle = (\mathbb{1} - \widehat{P}_{\text{abs}})\,|\underline{m}\rangle\,. \tag{3.25}$$

Applying the time-evolution operator of the closed systems $\widehat{U}$ from the left, and using Eq. (3.24) we can deduce the inverted relation

$$|\underline{m}\rangle = \frac{\widehat{U}\,|m\rangle}{\lambda_m}, \tag{3.26}$$

which shows that $|\underline{m}\rangle$ is essentially the time-evolved version of $|m\rangle$. In contrast to $|m\rangle$ which has no contributions in the absorbing region, Eq. (3.25), $|\underline{m}\rangle$ also exists on the absorbing region. As a consequence of Eq. (3.26) $|\underline{m}\rangle$ is normalizable, if $|m\rangle$ is normalizable. From Eq. (3.24) it is straight forward to show that

$$\exp(-\gamma_m) = \frac{\|\widehat{U}(\mathbb{1} - \widehat{P}_{\text{abs}})\,|\underline{m}\rangle\,\|^2}{\|\,|\underline{m}\rangle\,\|^2} = 1 - \frac{\|\widehat{P}_{\text{abs}}\,|\underline{m}\rangle\,\|^2}{\|\,|\underline{m}\rangle\,\|^2}, \tag{3.27}$$

where the second step exploits the unitarity of $\widehat{U}$. Assuming $\|\,|\underline{m}\rangle\,\|^2 = 1$ and $\gamma_m \ll 1$, we get

$$\gamma_m = \|\widehat{P}_{\text{abs}}\,|\underline{m}\rangle\,\|^2, \tag{3.28}$$

i. e., the regular-to-chaotic tunneling rate is given by the norm of the metastable state $|\underline{m}\rangle$ in the absorbing region. Note that Eqs. (3.16) and (3.28) are seemingly different due to the missing time-evolution operator in Eq. (3.28). However, both equations are actually the same. This can be seen from Eq. (3.26) which reveals that the time-evolution operator $\widehat{U}$ of Eq. (3.16) is simply hidden in the metastable eigenstate $|\underline{m}\rangle$ for Eq. (3.28).

We now proceed along the lines of the previous derivation. However, this time we approximate the time-evolved version of $|m\rangle$, namely the state $|\underline{m}\rangle$ by a regular basis state $|\psi^m_{\text{reg}}\rangle$. To this end we define the difference state

$$|\underline{d}\rangle := |\underline{m}\rangle - |\psi^m_{\text{reg}}\rangle, \tag{3.29}$$

and get

$$\gamma_m = \|\widehat{P}_{\text{abs}}\,|\psi^m_{\text{reg}}\rangle\,\|^2 + \langle\psi^m_{\text{reg}}|\widehat{P}_{\text{abs}}|\underline{d}\rangle + \langle\underline{d}|\widehat{P}_{\text{abs}}|\psi^m_{\text{reg}}\rangle + \langle\underline{d}|\widehat{P}_{\text{abs}}|\underline{d}\rangle. \tag{3.30}$$

This gives the regular-to-chaotic tunneling rate γ_m according to

$$\gamma_m = \|\widehat{P}_{\text{abs}}\,|\psi^m_{\text{reg}}\rangle\,\|^2, \tag{3.31}$$

which is valid up to errors

$$\Delta\gamma_m := \langle\psi_{\text{reg}}^m|\widehat{P}_{\text{abs}}|\underline{d}\rangle + \langle\underline{d}|\widehat{P}_{\text{abs}}|\psi_{\text{reg}}^m\rangle + \langle\underline{d}|\widehat{P}_{\text{abs}}|\underline{d}\rangle. \tag{3.32}$$

Similar as before we can provide the error bound

$$|\Delta\gamma_m| \leq 2\|\underline{d}\| + \|\underline{d}\|^2, \tag{3.33}$$

which shows that the validity of prediction (3.31) is guaranteed, for regular basis states which approximate the metastable eigenstate on the order of the tunneling rate

$$\|\underline{d}\| = \|\, |\underline{m}\rangle - \left|\psi_{\text{reg}}^m\right\rangle \| \lesssim \mathcal{O}(\gamma_m). \tag{3.34}$$

Similar to the previous derivation, it is an extremely challenging task to construct a regular basis state which approximates the metastable eigenstate $|\underline{m}\rangle$ on the order of the tunneling rate, such that, condition (3.34) is typically not fulfilled in practical implementations of Eq. (3.31). Hence, in this thesis Eq. (3.34) remains only a theoretical argument we use for deriving Eq. (3.31).

In contrast to Eq. (3.19) the new prediction, Eq. (3.31), does not contain the time-evolution operator $\widehat{U}$ any more. Therefore, assuming that $\widehat{P}_{\text{abs}}$ projects onto position space and $\left|\psi_{\text{reg}}^m\right\rangle$ can be constructed within a semiclassical WKB-approach, Eq. (3.31) is a quantum-mechanical precursor of a WKB-prediction for γ_m. For practical implementations though, Eq. (3.19) is typically favorable over Eq. (3.31). This is especially striking for maps with strongly mixing chaotic regions, as, e. g., discussed in Refs. [62, 65]. For such maps pulling the absorbing region away from the regular phase-space region gives numerically stable tunneling rates. The same is true, when applying Eq. (3.19) together with a basis state which concentrates in the regular phase-space region while decreasing exponentially towards the chaotic phase-space region. In contrast, using Eq. (3.31) together with such a basis state gives exponentially decreasing tunneling rates when pulling the absorbing regions away from the regular phase-space regions [119].

3.3.2. Constructing a fictitious integrable system for the standard map

As worked out in the previous sections, a prediction of regular-to-chaotic tunneling rates requires basis states $\left|\psi_{\text{reg}}^m\right\rangle$, which approximate the metastable eigenstates of an opened system $\widehat{U}_{\text{open}}$. As discussed in Refs. [62, 65], one possible way to construct such basis states is provided by using eigenstates of a fictitious integrable system H_{reg}. This fictitious integrable system H_{reg} has to resemble the regular tori of U as closely as possible, while extending the torus structure of the regular region beyond its boundary, see Fig. 3.8. In this section we show how such an integrable approximation H_{reg} for the standard map U is obtained, based on the analysis of fundamental frequencies [120] for the regular region. In that, we follow the presentation of Ref. [65].

The algorithm starts by defining a curve in phase space which parametrizes the tori of the regular phase-space region in terms of a curve parameter $\alpha \in [0, 1]$. For the standard map at $\kappa = 2.9$ we

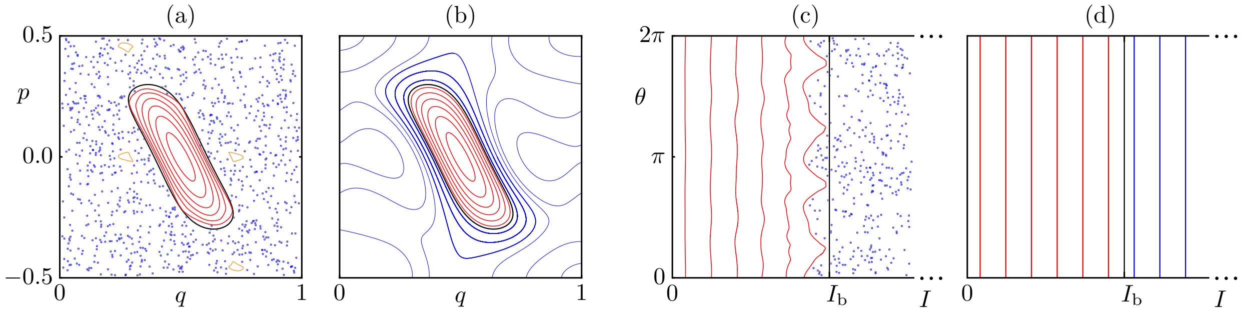

Figure 3.8.: (a) Phase space of the standard map at $\kappa = 2.9$ with regular tori (lines) and a chaotic orbit (dots), (c) in the action–angle coordinates of H_{reg}. (b) Phase space of H_{reg}, (d) in action–angle coordinates. The boundary torus I'_b is marked by a black line.

choose the curve

$$(q(\alpha), p(\alpha)) := (0.5 + 0.1 \cdot \alpha, 0.0), \tag{3.35}$$

connecting the central fixed point $(q, p) = (0.5, 0.0)$ with the boundary of the regular phase-space region. Subsequently, we choose values of α according to

$$0 \leq \alpha_0 \leq \dots \leq \alpha_i \leq \dots \leq \alpha_{i_{\max}} \leq 1 \quad \text{with} \quad i = 0, \dots, i_{\max}, \tag{3.36}$$

which defines initial conditions $(q(\alpha_i), p(\alpha_i))$ along the curve Eq. (3.35). From these initial conditions $(q(\alpha_i), p(\alpha_i))$ we compute orbits

$$(q_{i,n}, p_{i,n}) = U^n(q(\alpha_i), p(\alpha_i)) \quad \text{with} \quad n = 0, \dots, n_{\max} \tag{3.37}$$

with U^n denoting the n-fold application of the map U. Using the numerical analysis of fundamental frequencies [120], we determine the frequency ω_i of each orbit. Furthermore, an action I_i is assigned to each orbit according to $I_i = A_i/(2\pi)$, with A_i being the numerically computed phase-space area enclosed by the ith orbit. For the standard map we typically choose $\alpha_i = ([i + 1/2]/i_{\max})^{1/2}$ and exclude values of α, for which $(q(\alpha_i), p(\alpha_i))$ is too close to a non-linear resonance chain, i. e., we exclude orbits for which $\omega_i/(2\pi)$ is rational.

Consecutively, we fit a polynomial of order R,

$$\omega(I) := \omega_{\text{center}} + \sum_{r=1}^{R} c_r I^r, \tag{3.38}$$

to the numerically obtained data ω_i, I_i. Here, ω_{center} is the frequency of the regular phase-space region around the central fixed point, which for the standard map is given by, Eq. (2.24), with $\omega_{\text{center}} = \nu/(2\pi)$. For the above polynomial we typically use orders $3 \leq R \leq 5$. Subsequently we integrate Eq. (3.38),

$$E(I) := \int_0^I \omega(I')\,\mathrm{d}I' = \omega_{\mathrm{center}} I + \sum_{r=1}^{R} \frac{c_r}{r+1} I^{r+1}, \tag{3.39}$$

which allows for assigning energies $E_i := E(I_i)$ to all points of the regular orbit starting in (q_i, p_i). In that we define energies for the non-resonant points of the regular phase-space region. In order to obtain the integrable system H_{reg}, which approximates the tori of the regular phase-space region and provides an extension of regular tori to the chaotic region, we fit the function

$$H_{\mathrm{reg}}(q,p) = \sum_{k=-K}^{K} \sum_{l=-L}^{L} h_{k,l} \exp\left(2\pi \mathrm{i}\,[kq + lp]\right) \tag{3.40}$$

to the above energy landscape E_i at $(q_{i,n}, p_{i,n})$ of the regular region. Choosing an appropriate order K, L in this last fitting step, which on the one hand ensures a good approximation of tori inside the regular region of U, while providing a suitable extension of regular tori towards the chaotic phase-space region is typically an act of trial and error, which does not allow for many variations. For the standard map at $\kappa = 2.9$ we use an $H_{\mathrm{reg}}(q,p)$ according to Eq. (3.40) with $K = 2$, $L = 2$ together with the coefficients $h_{k,l}$ of Tab. 3.1. Note that the parity which is present in the standard map, is not imposed on the above Hamiltonian. However, the weakly broken parity of H_{reg} does not appear too striking in the following discussions.

3.3.3. Weyl quantization of an integrable system

In this section we show how to quantize the classical Hamilton function $H_{\mathrm{reg}}(q,p)$ obtained in the previous section, using the Weyl quantization [121].

Within the Weyl quantization scheme the operator $\widehat{H}_{\mathrm{reg}}$ is given by

$$\widehat{H}_{\mathrm{reg}}(\hat{q},\hat{p}) := \frac{1}{(2\pi)^2} \int_{\mathbb{R}} \mathrm{d}\xi \int_{\mathbb{R}} \mathrm{d}\eta \int_{\mathbb{R}} \mathrm{d}\tilde{q} \int_{\mathbb{R}} \mathrm{d}\tilde{p}\; H_{\mathrm{reg}}(\tilde{q},\tilde{p}) \exp\left(-\mathrm{i}\,[\xi(\tilde{q}-\hat{q}) + \eta(\tilde{p}-\hat{p})]\right). \tag{3.41}$$

Here, $\hat{q}$ and $\hat{p}$ are the position and momentum operators which fulfill the usual commutation relation $[\hat{q},\hat{p}] = \mathrm{i}\hbar$. Using the Baker–Campbell–Hausdorff formula [122, 123] it is convenient to split the exponential into two parts, such that

$$\widehat{H}_{\mathrm{reg}} = \frac{1}{(2\pi)^2} \int_{\mathbb{R}} \mathrm{d}\xi \int_{\mathbb{R}} \mathrm{d}\eta \int_{\mathbb{R}} \mathrm{d}\tilde{q} \int_{\mathbb{R}} \mathrm{d}\tilde{p}\; H_{\mathrm{reg}}(\tilde{q},\tilde{p}) \exp\left(-\mathrm{i}\xi(\tilde{q}-\hat{q})\right) \exp\left(-\mathrm{i}\eta(\tilde{p}-\hat{p})\right) \exp\left(\frac{\mathrm{i}\hbar}{2}\xi\eta\right). \tag{3.42}$$

Computing the position representation of this operator gives

$$\langle q' |\, \widehat{H}_{\mathrm{reg}}\, | q \rangle = \frac{1}{2\pi\hbar} \int_{\mathbb{R}} \mathrm{d}\tilde{p}\, H_{\mathrm{reg}}\left(\frac{q+q'}{2}, \tilde{p}\right) \exp\left(-\frac{\mathrm{i}}{\hbar}\tilde{p}(q-q')\right). \tag{3.43}$$

k	l	$h_{k,l}$
-2	-2	$-0.00354402080947 + \mathrm{i} \cdot 0.000223128338845$
-2	-1	$-0.00732397492445 - \mathrm{i} \cdot 0.000127286868468$
-2	0	$-0.00331407736367 - \mathrm{i} \cdot 5.66429043182 \cdot 10^{-05}$
-2	1	$-0.000230553400738 - \mathrm{i} \cdot 7.91885605796 \cdot 10^{-05}$
-2	2	$0.000463741567981 - \mathrm{i} \cdot 3.21015504093 \cdot 10^{-05}$
-1	-2	$0.00493726436345 + \mathrm{i} \cdot 0.000471199917317$
-1	-1	$0.0062671306568 + \mathrm{i} \cdot 0.000278024303203$
-1	0	$0.0154371570277 - \mathrm{i} \cdot 0.000404998467013$
-1	1	$-0.00122593699659 - \mathrm{i} \cdot 0.00028978687544$
-1	2	$0.00287198380122 - \mathrm{i} \cdot 0.000186151345082$
0	-2	$0.00765549922097 + \mathrm{i} \cdot 0.000388234368692$
0	-1	$-0.00280480280752 + \mathrm{i} \cdot 0.000636073701545$
0	0	$0.0748060409176 - \mathrm{i} \cdot 7.67538562065 \cdot 10^{-14}$
0	1	$-0.00280480280472 - \mathrm{i} \cdot 0.000636073701415$
0	2	$0.00765549922031 - \mathrm{i} \cdot 0.000388234368717$
1	-2	$0.00287198380169 + \mathrm{i} \cdot 0.000186151345055$
1	-1	$-0.00122593699741 + \mathrm{i} \cdot 0.000289786875538$
1	0	$0.0154371570258 + \mathrm{i} \cdot 0.000404998466916$
1	1	$0.00626713065914 - \mathrm{i} \cdot 0.000278024303132$
1	2	$0.00493726436331 - \mathrm{i} \cdot 0.000471199917323$
2	-2	$0.000463741568062 + \mathrm{i} \cdot 3.21015504001 \cdot 10^{-05}$
2	-1	$-0.000230553400642 + \mathrm{i} \cdot 7.91885606052 \cdot 10^{-05}$
2	0	$-0.00331407736444 + \mathrm{i} \cdot 5.66429042975 \cdot 10^{-05}$
2	1	$-0.00732397492399 + \mathrm{i} \cdot 0.000127286868481$
2	2	$-0.00354402080933 - \mathrm{i} \cdot 0.000223128338844$

Table 3.1.: Coefficients of the integrable approximation, Eq. (3.40), to the regular phase-space region of the standard map at $\kappa = 2.9$.

As we consider Hamilton functions $H_{\text{reg}}(q,p)$ which are M_{mom}-periodic in momentum space,

$$H_{\text{reg}}(q,p) = H_{\text{reg}}(q, p + M_{\text{mom}}) \qquad \forall q,p \in \mathbb{R}, \tag{3.44}$$

we can show that $\widehat{H}_{\text{reg}}$ commutes with the translation operator $\widehat{T}_{M_{\text{mom}}}$, introduced in Eq. (2.45),

$$[\widehat{H}_{\text{reg}}, \widehat{T}_{M_{\text{mom}}}] = 0. \tag{3.45}$$

Hence, we can consider the matrix representation of $\widehat{H}_{\text{reg}}$ on the cylinder $\mathbb{R} \times \big(\mathbb{R}/(p_{\min} + M_{\text{mom}}\mathbb{Z})\big)$,

$$\langle q_k | \widehat{H}_{\text{reg}} | q_l \rangle = \int\limits_{p_{\min}}^{p_{\min}+M_{\text{mom}}} \frac{\mathrm{d}p}{M_{\text{mom}}} H_{\text{reg}}\left(\frac{q_k + q_l}{2}, p\right) \exp\left(2\pi\mathrm{i}(k-n)\frac{p}{M_{\text{mom}}}\right). \tag{3.46}$$

Here, q_l are the sites of the position lattice, Eq. (2.47). Since we further consider Hamilton functions

$H_{\text{reg}}(q, p)$ which are M_{pos}-periodic in position space,

$$H_{\text{reg}}(q + M_{\text{pos}}, p) = H_{\text{reg}}(q, p) \qquad \forall q, p \in \mathbb{R}, \tag{3.47}$$

we can additionally show that $\widehat{H}_{\text{reg}}$ commutes with the translation operator $\widehat{T}_{M_{\text{pos}}}$, introduced in Eq. (2.37),

$$[\widehat{H}_{\text{reg}}, \widehat{T}_{M_{\text{pos}}}] = 0. \tag{3.48}$$

Hence, we can even consider the matrix representation of $\widehat{H}_{\text{reg}}$ on the torus $\mathbb{T} := \big(\mathbb{R}/(q_{\text{min}} + M_{\text{pos}}\mathbb{Z})\big) \times \big(\mathbb{R}/(p_{\text{min}} + M_{\text{mom}}\mathbb{Z})\big)$,

$$\langle \overline{q}_k | \widehat{H}_{\text{reg}} | \overline{q}_l \rangle = \sum_{\bar{p}_{\frac{r}{2}} \in \mathbb{T}} e^{\frac{\mathrm{i}}{\hbar}(\overline{q}_k - \overline{q}_l)\bar{p}_{\frac{r}{2}}} \frac{1}{2N} \left[H_{\text{reg}}\left(\frac{\overline{q}_k + \overline{q}_n}{2}, \bar{p}_{\frac{r}{2}} \right) + (-1)^r H_{\text{reg}}\left(\frac{\overline{q}_k + \overline{q}_l}{2} + \frac{M_{\text{pos}}}{2}, \bar{p}_{\frac{r}{2}} \right) \right]. \tag{3.49}$$

Here, $\bar{p}_{\frac{r}{2}}$ are momentum sites on the torus $\big(\mathbb{R}/(q_{\text{min}} + M_{\text{pos}}\mathbb{Z})\big) \times \big(\mathbb{R}/(p_{\text{min}} + M_{\text{mom}}\mathbb{Z})\big)$. They are given as in Eq. (2.39). However, the indices $r/2$ run in the half integers $\mathbb{Z}/2$ thereby belonging to the *Wigner phase-space lattice* [95], which is twice as fine as the original momentum lattice. The same is true for the position sites $(\overline{q}_k + \overline{q}_l)/2 = \overline{q}_{[k+l]/2}$, $(\overline{q}_k + \overline{q}_l + M_{\text{pos}})/2 = \overline{q}_{[k+l]/2} + M_{\text{pos}}$, which also belong to the Wigner phase-space lattice, which is twice as fine as the position lattice, Eq. (2.47).

3.3.4. Results for the standard map

In the following we, discuss the predictions of regular-to-chaotic tunneling rates for the standard map according to Eqs. (3.19), (3.31), and (3.23).

We start by constructing $\widehat{H}_{\text{reg}}$ on the torus $\big(\mathbb{R}/\mathbb{Z}\big) \times \big(\mathbb{R}/(-0.5 + \mathbb{Z})\big)$, Eq. (3.49), as introduced in Sects. 3.3.2 and 3.3.3. This gives a finite-dimensional matrix, whose eigenvalue equation,

$$\widehat{H}_{\text{reg}} \, |I_n\rangle = E_n \, |I_n\rangle \,, \tag{3.50}$$

is solved numerically. Its eigenstates $|I_n\rangle$ can be grouped into regular basis states $\big|\psi_{\text{reg}}^m\big\rangle \equiv |I_m\rangle$ for quantizing actions I_m smaller than the regular–chaotic boundary action I_{b}' and chaotic basis states $|\psi_{ch}\rangle \equiv |I_{ch}\rangle$ for actions $I_{ch} \geq I_{\text{b}}'$. If H_{reg} was a perfect approximation to the tori of U the action I_{b}' would be given by the area A_{reg} of the regular region $I_{\text{b}}' = A_{\text{reg}}/(2\pi)$. However, the tori of H_{reg} coincide with the tori of U on an approximate level only. Therefore, we choose $I_{\text{b}}' = 0.1223/(2\pi)$ as the action corresponding to the torus of H_{reg} which encloses the regular phase-space region of U and has minimal action, see black line in Fig. 3.8(a). Since I_{b}' is chosen from a classical criterion, it only coincides with a quantizing action for specific values of $\hbar$. Numerically, the sorting of states is implemented by ordering the basis states according to their localization properties from the inside to the outside of the central phase-space region of H_{reg}. While the first $N_{\text{reg}} = \lfloor I_{\text{b}}'/\hbar + 1/2 \rfloor$ states with

$m \in \{0, \dots, N_{\text{reg}} - 1\}$ are regular according to Bohr–Sommerfeld quantization, all other states are labeled as chaotic basis states. As discussed in Refs. [62, 65] the advantage of basis states $|\psi_{\text{reg}}^{m}\rangle$ and $|\psi_{ch}\rangle$ over eigenstates of the mixed system $\widehat{U}$, is that eigenstates of $\widehat{U}$ already have admixtures in the opposite phase-space region. In contrast the basis states localize maximally in one phase-space region while decaying as fast as possible towards the opposite phase-space region, see, e. g., Fig. 3.9.

Using the above basis states together with the time-evolution operator $\widehat{U}$ of the standard map, Eq. (2.61), on the torus $\big(\mathbb{R}/\mathbb{Z}\big) \times \big(\mathbb{R}/(-0.5 + \mathbb{Z})\big)$, we now evaluate Eqs. (3.19), (3.31), and (3.23). We start by discussing the results for Eq. (3.19), where $\widehat{P}_{\text{abs}}$ is defined according to

$$\widehat{P}_{\text{abs}} = \sum_{q_l \in \mathcal{R}_{\text{abs}}} |q_l\rangle \langle q_l| \tag{3.51}$$

from the states of the position lattice, which localize in the absorbing region $\mathcal{R}_{\text{abs}} = (-\infty, q_{\text{min}}) \cup (q_{\text{max}}, \infty)$, with $q_{\text{min}} = 0.2843$ and $q_{\text{max}} = 1 - q_{\text{min}}$ tangential to the regular region. The predicted tunneling rates are shown as diamonds connected by lines in Fig. 3.10, while numerical rates, Eq. (3.3), are shown as dots. Gray and colored dots further distinguish between numerical rates obtained from solving Eq. (3.3) for opening $\widehat{U}$ on the cylinder $\mathbb{R} \times \big(\mathbb{R}/(-0.5 + \mathbb{Z})\big)$, Eq. (2.52), or the torus $\big(\mathbb{R}/\mathbb{Z}\big) \times \big(\mathbb{R}/(-0.5 + \mathbb{Z})\big)$, Eq. (2.61), respectively. The agreement between predicted and numerical rates is satisfactory.

We continue with Fig. 3.11, which shows predictions obtained from Eq. (3.31) by diamonds connected by lines, i. e., in contrast to the prediction of the previous plot, the time evolution operator was omitted such that the weight of the basis state in the absorbing region provides the tunneling rate. The numerical rates, Eq. (3.3), are shown as dots again, with gray dots obtained from opening $\widehat{U}$ on the cylinder $\mathbb{R} \times \big(\mathbb{R}/(-0.5 + \mathbb{Z})\big)$, Eq. (2.52), and colored dots obtained from opening $\widehat{U}$ on the torus $\big(\mathbb{R}/\mathbb{Z}\big) \times \big(\mathbb{R}/(-0.5 + \mathbb{Z})\big)$, Eq. (2.61), respectively. The agreement between predicted and numerical rates is slightly enhanced, as compared to Fig. 3.10.

In order to illustrate the advantage of the improved fictitious integrable system approach over its

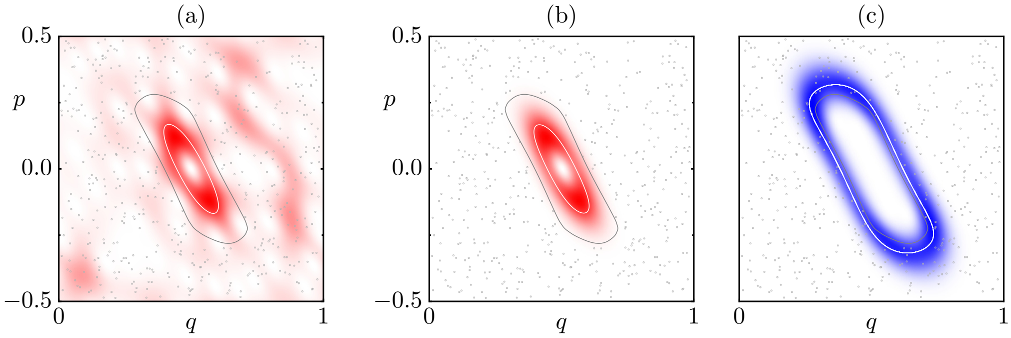

Figure 3.9.: Husimi representation of (a) an eigenstate of $\widehat{U}$ versus (b) a regular and (c) a chaotic basis state at $1/h = 50$. White lines present corresponding quantizing tori while the phase space of U is shown in gray.

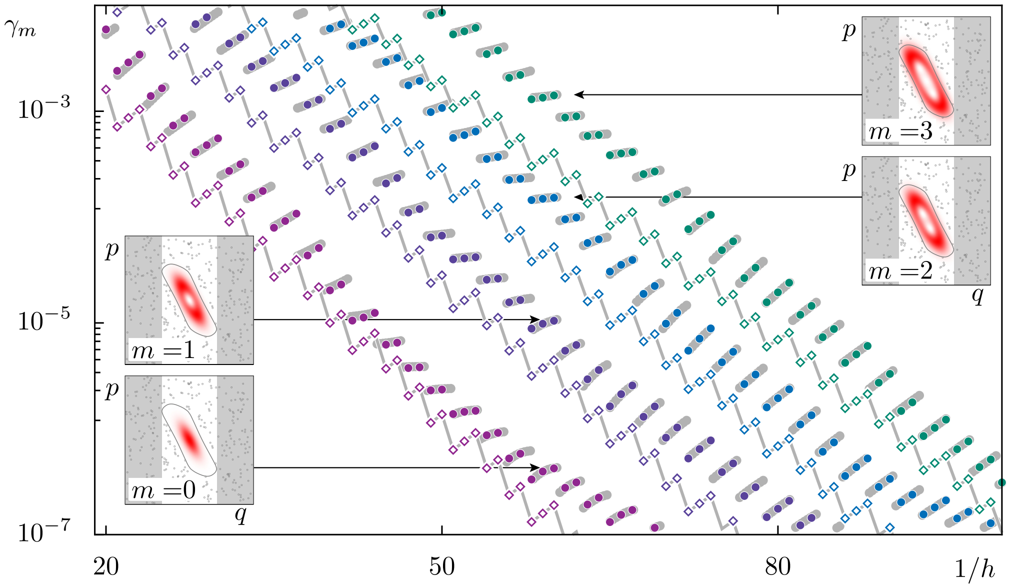

Figure 3.10.: Regular-to-chaotic tunneling rates γ_m versus inverse effective Planck constant $1/h$ of the standard map at $\kappa = 2.9$ for $m = 0, 1, 2, 3$ (bottom to top). Numerical rates (dots) are obtained from Eq. (3.3) using $\widehat{P}_{\text{abs}}$ as in Eq. (3.51) and $\widehat{U}$ on the cylinder (gray dots) or the torus (colored dots), respectively. The predicted rates (diamonds connected by lines) are obtained from Eq. (3.19) with the same $\widehat{P}_{\text{abs}}$.

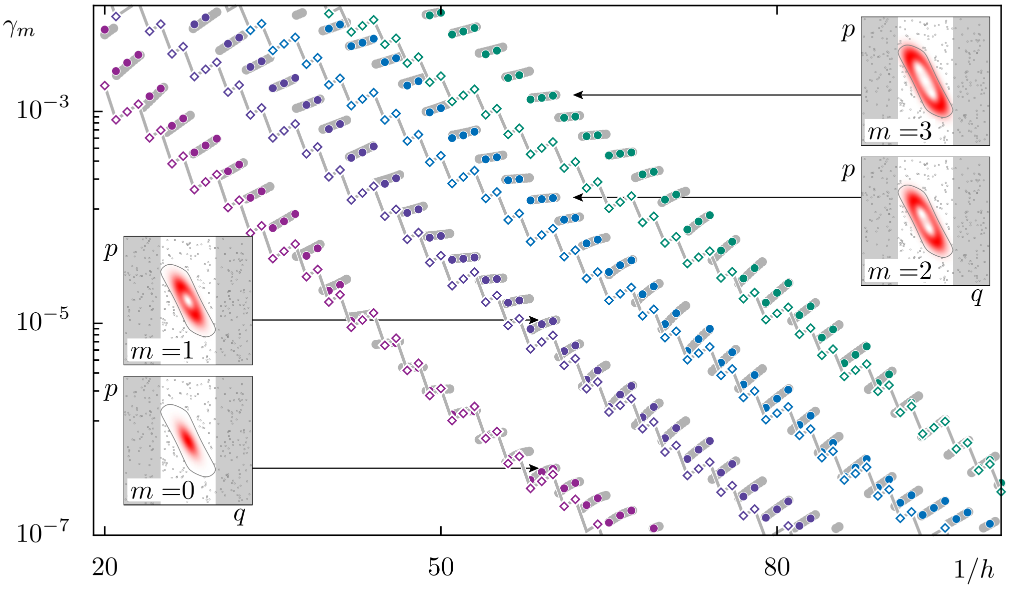

Figure 3.11.: Regular-to-chaotic tunneling rates γ_m versus inverse effective Planck constant $1/h$ of the standard map at $\kappa = 2.9$ for $m = 0, 1, 2, 3$ (bottom to top). Numerical rates (dots) are obtained from Eq. (3.3) using $\widehat{P}_{\text{abs}}$ as in Eq. (3.51) and $\widehat{U}$ on the cylinder (gray dots) or the torus (colored dots), respectively. The predicted rates (diamonds connected by lines) are obtained from Eq. (3.31) with the same $\widehat{P}_{\text{abs}}$.

previous version, as introduced in Refs. [62, 65], we now evaluate Eq. (3.23). The required projector $\widehat{P}_{\text{ch}}$ is constructed according to

$$\widehat{P}_{\text{abs}} = \sum_{I'_{\text{b}}<I_{ch}} |\psi_{ch} \equiv I_{ch}\rangle \langle \psi_{ch} \equiv I_{ch}| \,, \tag{3.52}$$

from the eigenstates $|\psi_{ch}\rangle$ of H_{reg}, which localize in the chaotic phase-space region. The resulting prediction of the tunneling rates is shown as diamonds connected by lines in Fig. 3.12. The numerical rates obtained from Eq. (3.3), are shown by dots. Comparing these results to the results of Figs. 3.10 and 3.11, the agreement between numerical and predicted rates has decreased. Especially the quantization jumps appear at different values of h for numerical and predicted rates. As discussed in the text around Eq. (3.8), the quantization jumps in the numerical rates occur due to a growing number of lattice points in the quantization of $\widehat{U}_{\text{open}}$. On the other hand, quantization jumps predicted by the fictitious integrable system approach, Eq. (3.23), occur due to the chaotic basis state $|\psi_{ch}\rangle \equiv |I_{ch}\rangle$, which localizes just beyond the regular–chaotic border, i. e., $I'_{\text{b}} \leq I_{ch} < I'_{\text{b}} + \hbar$, and carries the dominant contribution to Eq. (3.23). Exactly at values

$$\frac{1}{h} = \frac{ch + \frac{1}{2}}{2\pi I'_{\text{b}}} \tag{3.53}$$

with ch from $\mathbb{N}$, this state $|I_{ch}\rangle$ is relabeled from being a chaotic to being a regular basis state, such

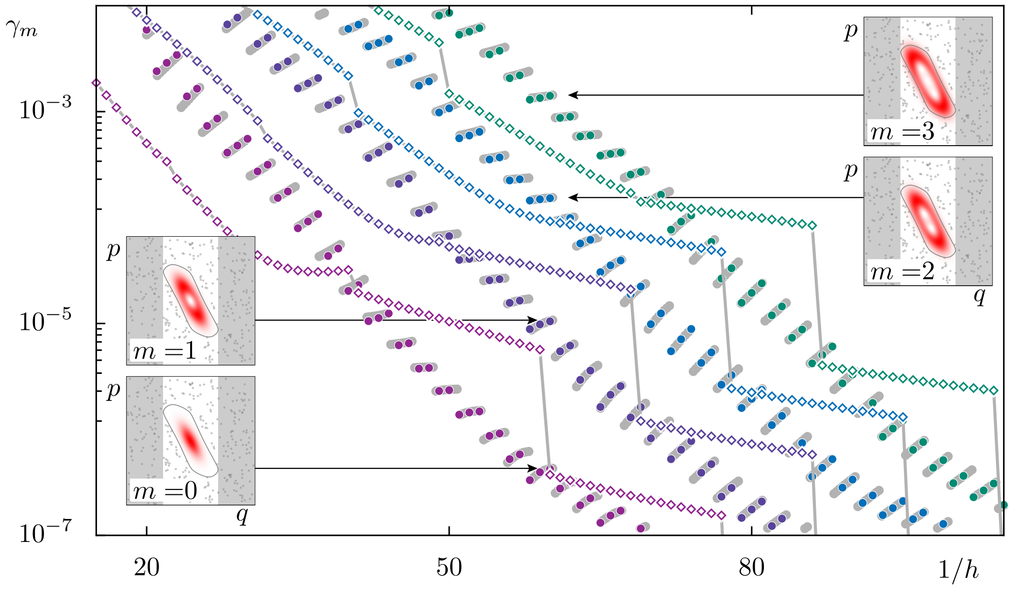

Figure 3.12.: Regular-to-chaotic tunneling rates γ_m versus inverse effective Planck constant $1/h$ of the standard map at $\kappa = 2.9$ for $m = 0, 1, 2, 3$ (bottom to top). Numerical rates (dots) are obtained from Eq. (3.3) using $\widehat{P}_{\text{abs}}$ as in Eq. (3.51) and $\widehat{U}$ on the cylinder (gray dots) or the torus (colored dots), respectively. The predicted rates (diamonds connected by lines) are obtained from Eq. (3.23) with $\widehat{P}_{\text{ch}}$ as in Eq. (3.52).

that it is removed from the projector $\widehat{P}_{\text{ch}}$, Eq. (3.52), and its contribution is removed from Eq. (3.23). This causes the quantization jump of the tunneling rates.

Finally, let us mention that within the improved fictitious integrable system approach, Eq. (3.19), it is of cause meaningful to predict regular-to-chaotic tunneling rates according to Eq. (3.23), if the numerical rates are obtained from Eq. (3.3), with $\widehat{P}_{\text{abs}} = \widehat{P}_{\text{ch}}$, and $\widehat{P}_{\text{ch}}$ defined as in Eq. (3.52). The results for these numerical and predicted data is presented in Fig. 3.13, by dots and diamonds respectively. In that case, the agreement between numerical and predicted data is again completely satisfactory. This result underlines that the essential point of using the improved fictitious integrable system approach, Eq. (3.19), instead of the original approach, Eq. (3.23), for predicting regular-to-chaotic tunneling rates is merely the unified use of $\widehat{P}_{\text{abs}}$ in the numerical determination of tunneling rates and their quantum-mechanical prediction.

3.3.5. Discussion and open problems – resonance chains, partial barriers, and regular basis states

So far, we have only presented predictions for regular-to-chaotic tunneling rates in the resonance-free h-regime of direct regular-to-chaotic tunneling. In addition only absorbing phase-space regions $\mathcal{R}_{\text{abs}}$ close to the regular–chaotic phase-space border were considered. Beyond these constraints, a prediction of regular-to-chaotic tunneling rates within the improved fictitious integrable system approach was so far impossible.

In order to understand the origin of this restriction let us recall that our prediction, Eq. (3.19),

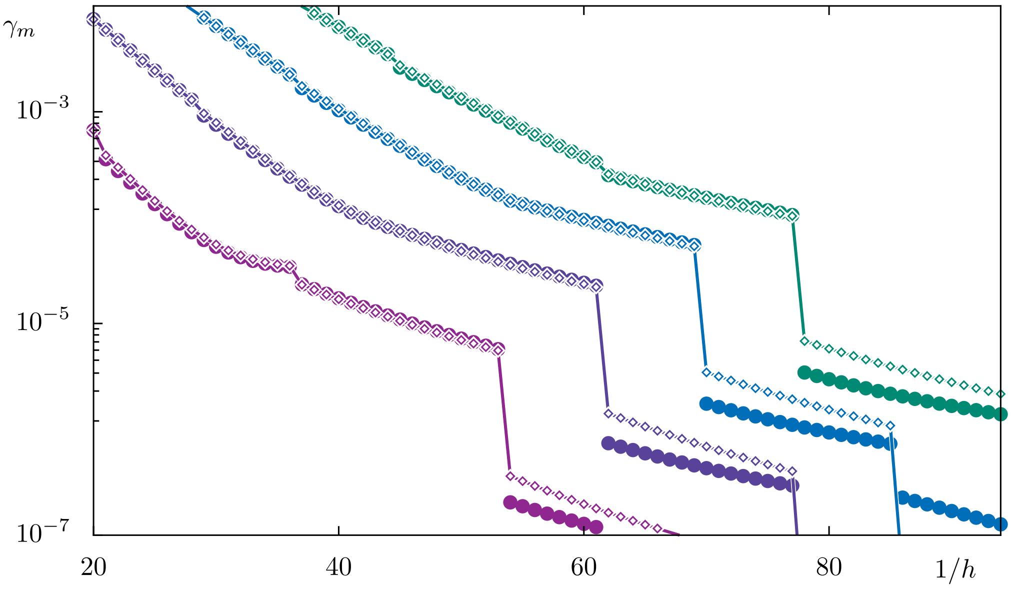

Figure 3.13.: Regular-to-chaotic tunneling rates γ_m versus inverse effective Planck constant $1/h$ of the standard map at $\kappa = 2.9$ for $m = 0, 1, 2, 3$ (bottom to top). Numerical rates (dots) are obtained from Eq. (3.3) using $\widehat{P}_{\text{abs}} = \widehat{P}_{\text{ch}}$ as in Eq. (3.52) and predicted rates (diamonds connected by lines) are obtained from Eq. (3.19) or (equivalently Eq. (3.23)) with $\widehat{P}_{\text{abs}} = \widehat{P}_{\text{ch}}$.

evaluates the exact predictions (3.16), by approximating the corresponding metastable eigenstates $|m\rangle$ in terms of a regular basis state $|\psi_{\text{reg}}^{m}\rangle$. In order to guarantee the validity of this approximation, we require the basis state $|\psi_{\text{reg}}^{m}\rangle$ to agree with the metastable eigenstates $|m\rangle$ within errors which are smaller than the predicted tunneling rate γ_m, see the sufficient condition in Eq. (3.22).

Hence, the future challenge in predicting effects of resonance-assisted tunneling on regular-to-chaotic tunneling rates γ_m in terms of Eq. (3.19) requires basis states $|\psi_{\text{reg}}^{m}\rangle$ which describe the localization of the metastable eigenstate $|m\rangle$ not only on the mth quantizing torus but also its $r:s$ resonance-induced admixtures on the higher excited quantizing tori $m + n \cdot r$. Note that this is already the central idea, behind the perturbation theory applied in Ref. [64]. Analogously, the future challenge in predicting effects of partial barriers on regular-to-chaotic tunneling rates γ_m in terms of Eq. (3.19), requires basis states $|\psi_{\text{reg}}^{m}\rangle$ which describe the localization properties of the metastable eigenstate $|m\rangle$ on the hierarchical phase-space region. Note that a more direct prediction of γ_m in terms of the exact Equation (3.16) would be favorable, if an analytic theory for metastable eigenstates $|m\rangle$, e. g., in terms of semiclassical expressions, was known. Since this is not the case, the detour of replacing $|m\rangle$ by an approximate regular basis state $|\psi_{\text{reg}}^{m}\rangle$ and evaluating Eq. (3.19) instead is so far the best foundation for constructing a semiclassical theory.

Finally, we point out that the prediction of regular-to-chaotic tunneling rates according to Eq. (3.19) possesses error terms which are controlled by Eq. (3.20) or the stronger sufficient condition Eq. (3.22). So far these equations only served as a theoretical justification for approximating metastable eigenstates $|m\rangle$ in terms of a regular basis states $|\psi_{\text{reg}}^{m}\rangle$. In the future it seems reasonable to exploit these equations as benchmarks for regular basis states $|\psi_{\text{reg}}^{m}\rangle$ and the underlying fictitious integrable systems H_{reg}. In the same way, the WKB-like prediction for regular-to-chaotic tunneling rates, Eq. (3.31), its error terms Eq. (3.32) or its sufficient condition Eq. (3.34) deserve a more intense investigation.

3.4. Summary on quantum-mechanical regular-to-chaotic tunneling rates

In this chapter we introduced the notion of regular-to-chaotic tunneling rates γ as a key quantity for characterizing regular-to-chaotic tunneling. A numerical determination of such tunneling rates as decay rates of metastable states was presented. The influence of non-linear resonance chains on regular-to-chaotic tunneling rates was discussed, which lead to a distinction of two h-regimes: (i) The resonance-free h-regime of direct regular-to-chaotic tunneling. Here, the metastable eigenstates of $\widehat{U}_{\text{open}}$ semiclassically localize on a single quantizing torus of the regular region. (ii) The h-regime of resonance-assisted regular-to-chaotic tunneling. Here, the metastable eigenstates of $\widehat{U}_{\text{open}}$ predominantly localize on a specific quantizing torus, but also have resonance-induced tunneling admixtures which localize on higher exited quantizing tori of the regular phase-space region, and thus, assist the tunneling process. Subsequently, we demonstrated that regular-to-chaotic tunneling rates depend on the choice of the absorbing region $\mathcal{R}_{\text{abs}}$. A phenomenological connection between the absorbing region $\mathcal{R}_{\text{abs}}$ and partial barriers in the hierarchical region was considered. Finally, the relation between tunneling rates and phase splittings of chaos-assisted tunneling [27] was discussed.

In the second part of this chapter, we derived an improved fictitious integrable system approach [62, 65], which allows for predicting regular-to-chaotic tunneling rates quantum-mechanically. Its application to the standard map was demonstrated. Finally, we concluded with the open problem of predicting effects of non-linear resonance chains and partial transport barriers on regular-to-chaotic tunneling rates γ_m within the fictitious integrable system approach.

4. Complex paths for regular-to-chaotic tunneling rates

In this chapter we develop a complex-path approach for regular-to-chaotic tunneling rates. In Sect. 4.1, this approach is derived by combining the fictitious integrable system approach, Refs. [62, 65], in its improved version, Eq. (3.19) of Sect. 3.3, with the semiclassical complex-path method of Shudo and Ikeda, Refs. [76–82]. This gives a semiclassical prediction for regular-to-chaotic tunneling rates, Eq. (4.14), which is the main result of this thesis. In Sect. 4.2 we illustrate how the required complex paths for our semiclassical approach can be constructed. An explicit construction of these paths for the standard map is demonstrated. In Sect. 4.3, we present and discuss the successful semiclassical predictions of our complex-path approach for regular-to-chaotic tunneling rates for the standard map. We close this chapter by discussing the embedding of our complex paths into the complexified phase space of the standard map in Sect. 4.4. In that we establish the essential geometric picture of our complex-path approach. The results presented in this chapter are an extended version of Ref. [116].

4.1. Semiclassical predictions for regular-to-chaotic tunneling rates

In this section, we derive a semiclassical prediction, Eq. (4.14), for regular-to-chaotic tunneling rates of time-periodic open systems $(\mathbb{1} - \widehat{P}_{\text{abs}})\widehat{U}(\mathbb{1} - \widehat{P}_{\text{abs}})$. Here, the classical analog of the corresponding unitary time-evolution operator $\widehat{U}$ is a stroboscopic, symplectic map U on a two-dimensional phase space. The derivation of Eq. (4.14) is based on a combination of the improved fictitious integrable system approach, Eq. (3.19) of Sect. 3.3, and the semiclassical complex-path method of Shudo and Ikeda, Refs. [76–82].

This section is organized as follows: In Sect. 4.1.1, we reformulate the quantum-mechanical predictions for regular-to-chaotic tunneling rates, Eq. (3.19), in terms of quantum-mechanical tunneling-matrix elements. Subsequently, these tunneling-matrix elements are expressed in terms of a semiclassical propagator as introduced in Refs. [76–82]. In Sect. 4.1.3 this results in a semiclassical prediction for regular-to-chaotic tunneling rates, Eq. (4.8), which is further simplified to our main result, Eq. (4.14).

4.1.1. Regular-to-chaotic tunneling rates from regular-to-chaotic tunneling-matrix elements

We start our derivation of semiclassical regular-to-chaotic tunneling rates from the quantum-mechanical prediction of Eq. (3.19). This prediction is a sum of quantum-mechanical transition probabilities,

$$\gamma_m = \sum_{ch} |\langle \psi_{\text{abs}}^{ch} | \widehat{U} | \psi_{\text{reg}}^{m} \rangle|^2. \tag{4.1}$$

These transitions take place between the regular basis state $|\psi_{\text{reg}}^{m}\rangle$, localizing on the regular phase-space region, and chaotic basis states $|\psi_{\text{abs}}^{ch}\rangle$, localizing on the absorbing region $\mathcal{R}_{\text{abs}}$ in the chaotic part of phase space. In contrast to Eq. (3.19), Eq. (4.1) explicitly assumes that the projector $\widehat{P}_{\text{abs}}$ on the absorber in the chaotic phase-space region is representable as a projector sum on orthonormal chaotic basis states

$$\widehat{P}_{\text{abs}} = \sum_{ch} |\psi_{\text{abs}}^{ch}\rangle\langle\psi_{\text{abs}}^{ch}|. \tag{4.2}$$

Note that the corresponding projectors, discussed in Chap. 3 for the standard map, Eqs. (3.51) and (3.52), have exactly this shape.

As previously discussed in Sect. 3.3 the basis states $|\psi_{\text{reg}}^{m}\rangle$ are not the eigenstates of the time-evolution operator $\widehat{U}$, but rather originate from an integrable approximation to the regular phase-space region, e. g., in terms of a fictitious integrable system H_{reg}. For the upcoming derivation it is convenient to stress that this gives rise to a canonical transformation,

$$(q, p) = \mathcal{K}_{\text{reg}}(I, \theta), \tag{4.3}$$

which provides the points (q, p) in phase space in terms of the action–angle coordinates of the integrable approximation. This allows for labeling the regular basis states $|\psi_{\text{reg}}^{m}\rangle$ in terms of quantizing actions I_m, according to $|\psi_{\text{reg}}^{m}\rangle = |I_m\rangle$. For the upcoming derivation it is further convenient to assume there is also a fictitious integrable structure which describes the absorber in the chaotic phase-space region. This structure gives rise to another canonical transformation,

$$(q', p') = \mathcal{K}_{\text{abs}}(I', \theta'). \tag{4.4}$$

It represents the points (q', p') of the absorbing phase-space region $\mathcal{R}_{\text{abs}}$ by classical action–angle coordinates $(I', \theta') \in \overline{\mathcal{R}}_{\text{abs}} \times [0, 2\pi)$. This allows for labeling the basis states $|\psi_{\text{abs}}^{ch}\rangle$ in terms of quantizing actions I'_{ch}, according to $|\psi_{\text{abs}}^{ch}\rangle = |I'_{ch}\rangle$. In order to emphasize their localization in the chaotic phase-space region, we denote their semiclassical quantum number by ch. Note that the projectors discussed for the standard map in Chap. 3 are determined from such integrable structures. For $\widehat{P}_{\text{abs}}$, Eq. (3.52), this is due to its origin from a fictitious integrable system H_{reg}. Here, $\overline{\mathcal{R}}_{\text{abs}} = [I'_{\text{b}}, \infty)$. Analogously, for $\widehat{P}_{\text{abs}}$, Eq. (3.51), this is due to its origin from the fictitious integrable system

$H_{\mathrm{reg}}(q,p) = q$. Considering this system on a phase space with period $M_{\mathrm{mom}} = 1$ in momentum direction allows for identifying the quantizing actions with the sites of the position lattice, Eq. (2.47), according to $I'_{ch} = q_{l=ch}/(2\pi)$ such that $\overline{\mathcal{R}}_{\mathrm{abs}} = (-\infty, q_{\mathrm{min}}/(2\pi)) \cup (q_{\mathrm{max}}/(2\pi), \infty)$.

After introducing the relabeled basis states the quantum-mechanical prediction of regular-to-chaotic tunneling rates of Eq. (4.1) becomes

$$\gamma_m = \sum_{I'_{ch} \in \overline{\mathcal{R}}_{\mathrm{abs}}} |\langle I'_{ch}|\widehat{U}|I_m\rangle|^2. \tag{4.5}$$

This prediction is still quantum mechanical in nature. However, the notation already hints the semiclassical picture behind regular-to-chaotic tunneling rates, which are semiclassically given by complex paths between the approximate quantizing tori I_m of the regular phase-space region and the fictitious quantizing absorber tori I'_{ch} which localize in the chaotic phase-space region. Note that the imprint of the improved fictitious integrable system approach on Eq. (4.5) lies in using regular basis states $|I_m\rangle$ and chaotic basis states $|I'_{ch}\rangle$ for the absorbing region, which originate from different sets of action–angle coordinates, i. e., $\mathcal{K}_{\mathrm{abs}} \neq \mathcal{K}_{\mathrm{reg}}$. Nevertheless, Eq. (4.5) also describes the fictitious integrable system approach of Refs. [62, 65], according to Eq. (3.23), if the tori I_m and I'_{ch} are provided by a single canonical transformation $\mathcal{K}_{\mathrm{abs}} = \mathcal{K}_{\mathrm{reg}}$. We further point out that upon replacing the time-evolution operator $\widehat{U}$ by the identity operator, Eq. (4.5) represents the WKB-like prediction of Eq. (3.31).

4.1.2. Complex paths for regular-to-chaotic tunneling-matrix elements

Based on standard semiclassical methods [91, 92] we evaluate the regular-to-chaotic tunneling-matrix elements, $\langle I'_{ch}|\widehat{U}|I_m\rangle$, of Eq. (4.5) semiclassically, see Appendix B for details. This results in a semiclassical propagator for regular-to-chaotic tunneling-matrix elements,

$$\langle I'_{ch}|\widehat{U}|I_m\rangle = \sum_{\nu} \sqrt{\frac{\hbar}{2\pi} \frac{\partial^2 \mathcal{S}_\nu(I'_{ch}, I_m)}{\partial I'_{ch}\, \partial I_m}} \exp\left(\mathrm{i}\frac{\mathcal{S}_\nu(I'_{ch}, I_m)}{\hbar} + \mathrm{i}\phi_\nu\right). \tag{4.6}$$

This propagator is the familiar one-step version of the propagator used in Ref. [81]. Similar versions are discussed in Refs. [76–82]. The above propagator is evaluated from the action

$$\mathcal{S}_\nu(I'_{ch}, I_m) = \int\limits_{\mathcal{C}_{m,\nu}} p(q, I_m)\mathrm{d}q + \mathcal{S}^U_\nu(q'_\nu, q_\nu) + \int\limits_{\mathcal{C}_{ch,\nu}} p'(I'_{ch}, q')\mathrm{d}q' \tag{4.7}$$

of paths ν, which connect the approximate integrable tori I_m of the regular phase-space region to the tori I'_{ch} of the absorber in the chaotic phase-space region. The construction of such paths requires to find the points (q_ν, p_ν) on the complexified torus I_m which map to points (q'_ν, p'_ν) on the complexified torus I'_{ch} via the complexified map U. These points give rise to three path segments, see Fig. 4.1, (S1–S3):

(S1) The first WKB-like segment originates from the regular basis states $|I_m\rangle$. It corresponds to the curve $\mathcal{C}_{m,\nu}$ on the complexified initial torus I_m. This curve connects a reference point (q_m, p_m) on the real torus I_m to the point (q_ν, p_ν). Along this curve we compute the WKB-like contribution $\int_{\mathcal{C}_{m,\nu}} p(q, I_m)\mathrm{d}q$ to Eq. (4.7). (S2) The second segment originates from the semiclassical propagator corresponding to $\widehat{U}$. This time-evolution segment is obtained by applying the complexified map U of the non-integrable system. It has to connect (q_ν, p_ν) on the initial complexified torus I_m to a point (q'_ν, p'_ν) on the final complexified torus I'_{ch}. This requirement also defines the possible end points (q_ν, p_ν) of the first segment. Note that this time-evolution segment can only exist, if I_m is not an invariant torus of U. This demonstrates the importance of using approximate tori I_m, e. g., from a fictitious integrable system in our approach. The time-evolution segment contributes the action $\mathcal{S}^U_\nu(q'_\nu, q_\nu)$ to Eq. (4.7). (S3) The final WKB-like segment originates from the chaotic basis state $|I'_{ch}\rangle$ in the absorbing phase-space region. It is the curve $\mathcal{C}_{ch,\nu}$ along the analytic continuation of the final torus I'_{ch}. This curve connects the end point of the time-evolution segment (q'_ν, p'_ν) on the complexified torus I'_{ch} to a reference point (q'_{ch}, p'_{ch}) of the real torus I'_{ch}. Along this curve we compute the WKB-like contribution $\int_{\mathcal{C}_{ch,\nu}} p'(I'_{ch}, q')\mathrm{d}q'$ to Eq. (4.7). Finally, the Maslov phase ϕ_ν in Eq. (4.6) accounts for phase shifts between distinct paths ν due to turning points. For a sketch of the complex paths, see, e. g., Fig. 4.1.

4.1.3. Semiclassical regular-to-chaotic tunneling rates

Combining Eqs. (4.5) and (4.6), we obtain a semiclassical prediction for regular-to-chaotic tunneling rates,

$$\gamma_m = \sum_{I'_{ch} \in \overline{\mathcal{R}}_{\text{abs}}} \left| \sum_\nu \sqrt{\frac{\hbar}{2\pi} \frac{\partial^2 \mathcal{S}_\nu(I'_{ch}, I_m)}{\partial I'_{ch}\, \partial I_m}} \exp\left(\mathrm{i}\frac{\mathcal{S}_\nu(I'_{ch}, I_m)}{\hbar} + \mathrm{i}\phi_\nu\right)\right|^2. \tag{4.8}$$

Unfortunately, the evaluation of the above expression requires a determination of new complex paths for each quantizing torus I'_{ch} of the absorbing phase-space region. Moreover, each path ν requires a determination of the Maslov phase ϕ_ν, in order to describe interference between distinct paths correctly.

Diagonal approximation

In order to derive a semiclassical prediction which is easier to evaluate, we simplify Eq. (4.8) in terms of a diagonal approximation,

$$\gamma_m = \sum_{I'_{ch} \in \overline{\mathcal{R}}_{\text{abs}}} \sum_\nu \frac{\hbar}{2\pi} \left| \frac{\partial^2 \mathcal{S}_\nu(I'_{ch}, I_m)}{\partial I'_{ch}\, \partial I_m} \right| \exp\left(-\frac{2\,\mathrm{Im}\,\mathcal{S}_\nu(I'_{ch}, I_m)}{\hbar}\right). \tag{4.9}$$

This approximation is exact, if only a single path contributes to the path summation ($\sum_\nu$) in Eq. (4.8). In contrast, if a finite number ($\nu_{\max} + 1$) of equally contributing paths dominate the path summation ($\sum_\nu$) in Eq. (4.8), we assume that random interference between these dominant paths cancels the cross terms, giving the diagonal approximation of Eq. (4.8). A more rigorous statement can be made using Jensen's inequality,

$$\begin{aligned}\Bigg|\sum_\nu \sqrt{\frac{\hbar}{2\pi}\frac{\partial^2\mathcal{S}_\nu(I'_{ch},I_m)}{\partial I'_{ch}\,\partial I_m}}\exp\left(\mathrm{i}\frac{\mathcal{S}_\nu(I'_{ch},I_m)}{\hbar}+\mathrm{i}\phi_\nu\right)\Bigg|^2&\\ \leq(\nu_{\max}+1)\sum_\nu\frac{\hbar}{2\pi}\left|\frac{\partial^2\mathcal{S}_\nu(I'_{ch},I_m)}{\partial I'_{ch}\,\partial I_m}\right|\exp\left(-\frac{2\,\mathrm{Im}\,\mathcal{S}_\nu(I'_{ch},I_m)}{\hbar}\right),&\qquad(4.10)\end{aligned}$$

which means that the tunneling rate of Eq. (4.8) is at most $(\nu_{\max}+1)$ times larger than the diagonal approximation of Eq. (4.9). On the other hand uncontrolled errors can arise from the diagonal approximation, if destructive interference of different paths in Eq. (4.8) leads to tunneling rates, which are significantly overestimated by the diagonal approximation of Eq. (4.9). For our predictions errors due to this diagonal approximation are expected to vanish in the semiclassical limit. In this limit the single path with the smallest imaginary action dominates the paths summation ($\sum_\nu$) in Eq. (4.8), such that the diagonal approximation becomes exact.

Edge contribution

Summing the diagonal terms in Eq. (4.9) over the quantizing actions I'_{ch} still requires to determine new complex paths for each quantizing torus I'_{ch}. This effort can be drastically reduced by approximating the sum over discrete quantizing actions I'_{ch} by an integral over continuous actions I',

$$\gamma_m=\sum_\nu\int_{I'\in\overline{\mathcal{R}}_{\mathrm{abs}}}\mathrm{d}I'\,\frac{1}{2\pi}\left|\frac{\partial^2\mathcal{S}_\nu(I',I_m)}{\partial I'\,\partial I_m}\right|\exp\left(-\frac{2\,\mathrm{Im}\,\mathcal{S}_\nu(I',I_m)}{\hbar}\right).\qquad(4.11)$$

Numerically we observe that the most important contributions to Eq. (4.11), originate from the (possibly multiple) boundaries of the absorbing phase-space region $\partial\overline{\mathcal{R}}_{\mathrm{abs}}$, where $I'=I'_{\mathrm{b}}$, see, e. g., Fig. 4.4. Hence, the integrals in Eq. (4.11) are dominated by the corresponding integrands at the boundaries I'_{b}, rather than by saddle points along the integration contour. Under this assumption we expand the actions $\mathcal{S}_\nu(I',I_m)$ to first order in the exponential in the vicinity of I'_{b},

$$\mathcal{S}_\nu(I',I_m)\approx\mathcal{S}_\nu(I'_{\mathrm{b}},I_m)+\left.\frac{\partial\mathcal{S}_\nu(I',I_m)}{\partial I'}\right|_{I'=I'_{\mathrm{b}}}(I'-I'_{\mathrm{b}}).\qquad(4.12)$$

From now on using the notation

$$\left.\frac{\partial\mathcal{S}_\nu(I',I_m)}{\partial I'}\right|_{I'=I'_{\mathrm{b}}}=\frac{\partial\mathcal{S}_\nu(I'_{\mathrm{b}},I_m)}{\partial I'_{\mathrm{b}}},\qquad(4.13)$$

we evaluate the contribution of the integral at the boundaries, $I'_{\mathrm{b}}\in\partial\overline{\mathcal{R}}_{\mathrm{abs}}$, of the absorbing region. In contrast to Eq. (4.8) this results in a prediction which only requires paths that connect the complexified torus I_m to the complexified boundary torus I'_{b}. This gives the main semiclassical result for regular-to-chaotic tunneling rates,

$$\gamma_m = \sum_{\nu} \sum_{I'_{\mathrm{b}} \in \partial\overline{\mathcal{R}}_{\mathrm{abs}}} \frac{\hbar}{2\pi} \frac{\left| \frac{\partial^2 \mathcal{S}_\nu(I'_{\mathrm{b}}, I_m)}{\partial I'_{\mathrm{b}} \partial I_m} \right|}{\left| 2\,\mathrm{Im}\, \frac{\partial \mathcal{S}_\nu(I'_{\mathrm{b}}, I_m)}{\partial I'_{\mathrm{b}}} \right|} \exp\left(- \frac{2\,\mathrm{Im}\,\mathcal{S}_\nu(I'_{\mathrm{b}}, I_m)}{\hbar} \right). \tag{4.14}$$

It predicts regular-to-chaotic tunneling rates from the complex action $\mathcal{S}_\nu(I'_{\mathrm{b}}, I_m)$, Eq. (4.7), of complex paths ν, which connect the WKB-like segments (S1) and (S3) on the complexified tori I_m and I_{ch} via a time-evolution segment (S2) of the non-integrable system U, see Fig. 4.1.

Discussion

The main advance of the presented complex-path approach is that here the required complex paths for regular-to-chaotic tunneling rates can be constructed. In that we show that a semiclassical prediction of regular-to-chaotic tunneling rates in non-integrable systems with a mixed phase space is possible. In contrast to WKB-like approaches this is facilitated within our complex-path approach due to the use of approximate tori I_m for the regular region. The analytic continuation of such tori can be extended beyond the natural boundary of the corresponding invariant tori. This allows for extending the WKB-segment (S1) sufficiently deep into the complexified phase space in order to provide a time-evolution segment (S2) which maps to the quantizing absorber tori I'_{b} in the chaotic phase space. This would not be possible with the corresponding invariant tori of the non-integrable system U, because there the WKB-segment (S1) can only be extended up to the natural boundary such that the time-evolution segment (S2) would remain on I_m. For a deeper discussion of this geometric picture see Sect. 4.4. Note that for WKB-like paths in near-integrable systems similar ideas to overcome natural boundaries were used [59, 71, 73, 75].

Furthermore, our main result, Eq. (4.14), formally resembles the WKB-prediction for integrable systems, Eq. (1.1). In that it provides a semiclassical justification for the long-conjectured, Ref. [83], and often-observed, Refs. [40, 42, 43, 47, 50, 65], exponential scaling of direct regular-to-chaotic tunneling rates γ_m with effective Planck's constant h.

For applying our prediction, Eq. (4.14), one has to (A) construct the complexified tori I_m and I'_{b}, e. g., by using a fictitious integrable system H_{reg}, (B) find the complex paths ν between I_m and I'_{b} giving rise to the segments (S1–S3), and (C) compute their action $\mathcal{S}_\nu$ according to Eq. (4.7) and select the dominant paths, which have the smallest positive imaginary action. How this is done is demonstrated in the following section.

4.2. Constructing regular-to-chaotic complex paths

In this section we describe how a semiclassical evaluation of regular-to-chaotic tunneling rates according to Eq. (4.14) is implemented. To this end, we implement steps (A–C): (A) We complexify the tori I_m and I'_{ch} corresponding to the regular and the chaotic phase-space region, respectively. (B) We search for the complex paths, connecting these tori in complexified phase space. This gives the time-evolution segment (S2) connecting the WKB-segments (S1) and (S3) along the tori I_m and I'_{b}, respectively. (C) From Eq. (4.7) we compute the action of each path, using the dominant ones with the smallest positive imaginary action for evaluating Eq. (4.14). A similar procedure would apply for evaluating regular-to-chaotic tunneling-matrix elements, Eq. (4.6), or regular-to-chaotic tunneling rates from Eq. (4.8).

The following implementation of (A–C) is given from the point of view that the canonical transformations, $\mathcal{K}_{\mathrm{reg}}$ and $\mathcal{K}_{\mathrm{abs}}$, which generate the approximate tori of the regular and the absorbing phase-space region, are not given explicitly. Instead they are given implicitly by fictitious integrable systems H_{reg} and H_{abs}. In order to illustrate the method, each step (A–C) is specified for the standard map, focusing on the case $H_{\mathrm{reg}} = H_{\mathrm{abs}}$, with H_{reg} provided by Eq. (3.40) and Tab. 3.1 of Sect. 3.3.2.

Prior to implementing steps (A–C), we identify reference points, (q_m, p_m) and $(q'_{\mathrm{b}}, p'_{\mathrm{b}})$, on the tori I_m of H_{reg} and I'_{b} of H_{abs}, respectively. Subsequently, we determine the round-trip frequencies, ω_m and ω'_{b}, and the energies, E_m and E'_{b}, of I_m and I'_{b}, respectively. For the example of the standard map with $H_{\mathrm{reg}} = H_{\mathrm{abs}}$, this is implemented by parametrizing the tori of H_{reg} by a curve of reference points $(q(\alpha), p(\alpha)) = (0.5 + \alpha, 0.0)$. Along this curve we determine (q_m, p_m) and $(q'_{\mathrm{b}}, p'_{\mathrm{b}})$ by numerical optimization, i. e., we shift α until a numerical integration of Hamilton's equations gives closed orbits which encircle the areas $2\pi I_m$ or $2\pi I'_{\mathrm{b}}$, respectively. The corresponding round-trip frequencies, $\omega_m = 2\pi/T_m$ and $\omega'_{\mathrm{b}} = 2\pi/T'_{\mathrm{b}}$, are obtained by numerically integrating Hamilton's equations from the reference points (q_m, p_m) and $(q'_{\mathrm{b}}, p'_{\mathrm{b}})$ up to periods T_m and T'_{b} respectively, for which the numerical trajectories first revisit the corresponding reference points. The energies of the tori I_m and I'_{b} are computed as $E_m = H_{\mathrm{reg}}(q_m, p_m)$ and $E'_{\mathrm{b}} = H_{\mathrm{abs}}(q'_{\mathrm{b}}, p'_{\mathrm{b}})$, respectively.

Constructing complexified tori of H_{reg}

In construction step (A) we provide the complexified tori corresponding to I_m and I'_{b}. If the canonical transformations $\mathcal{K}_{\mathrm{reg}}$ and $\mathcal{K}_{\mathrm{abs}}$ were explicitly known, the complex positions and complex momenta of the complexified tori,

$$T_{I_m} := \left\{ \big(q(I_m,\theta),\, p(I_m,\theta)\big) = \mathcal{K}_{\mathrm{reg}}(I_m,\theta) \in \mathbb{C}^2 \;:\; \theta \in \big([0,2\pi) + \mathrm{i}\mathbb{R}\big) \right\}, \tag{4.15}$$

$$T_{I'_{\mathrm{b}}} := \left\{ \big(q'(I'_{\mathrm{b}},\theta'),\, p'(I'_{\mathrm{b}},\theta')\big) = \mathcal{K}_{\mathrm{abs}}(I'_{\mathrm{b}},\theta') \in \mathbb{C}^2 \;:\; \theta' \in \big([0,2\pi) + \mathrm{i}\mathbb{R}\big) \right\}, \tag{4.16}$$

can be determined from the action–angle coordinates, respectively, with fixed action and complex angle.

Here, the canonical transformations are not known explicitly. In order to provide the complexified torus I_m of H_{reg} we exploit that the time-evolution along the torus I_m is given by $\theta(t) = \omega_m t$, in action–angle coordinates. Hence, a numerical integration of Hamilton's equations starting from the reference point $(q_m, p_m) = \mathcal{K}_{\mathrm{reg}}(I_m, 0)$ up to complex times $t = \theta/\omega_m$ gives the point $(q(I_m,\theta), p(I_m,\theta)) = \mathcal{K}_{\mathrm{reg}}(I_m, \theta = \omega_m t)$ on the complexified torus I_m, Eq. (4.15). Since this torus may have singularities at complex angles θ, we set branch cuts by first integrating in real and then in imaginary time. Analogously we obtain the points on the complexification of the torus I'_{b}, Eq. (4.16). An example of the resulting tori for H_{reg} is illustrated by red and blue surfaces in Fig. 4.1. Figure 4.2 presents the same tori in action–angle coordinates. Note that constructing complexified tori of H_{reg} by the method of real and imaginary time evolution only works for systems with a two-dimensional phase space.

A shooting algorithm for finding time-evolution segments

In construction step (B) we search for points (q_ν, p_ν) on the complexified torus I_m which map to a point (q'_ν, p'_ν) on the complexified torus I'_{b}. This gives the segments (S1–S3) of the complex path ν, see, e. g., the green arrows in Figs. 4.1 and 4.2.

In order to find these points we apply a shooting algorithm, i. e., we map the initial complexified torus I_m, Eq. (4.15), giving $U(q(I_m, \theta), p(I_m, \theta))$ and search for intersections of these mapped points with the complexified final torus I'_{b}, Eq. (4.16). This amounts to finding the intersection points of two real manifolds of dimension two in a four-dimensional phase space. In order to find these intersection

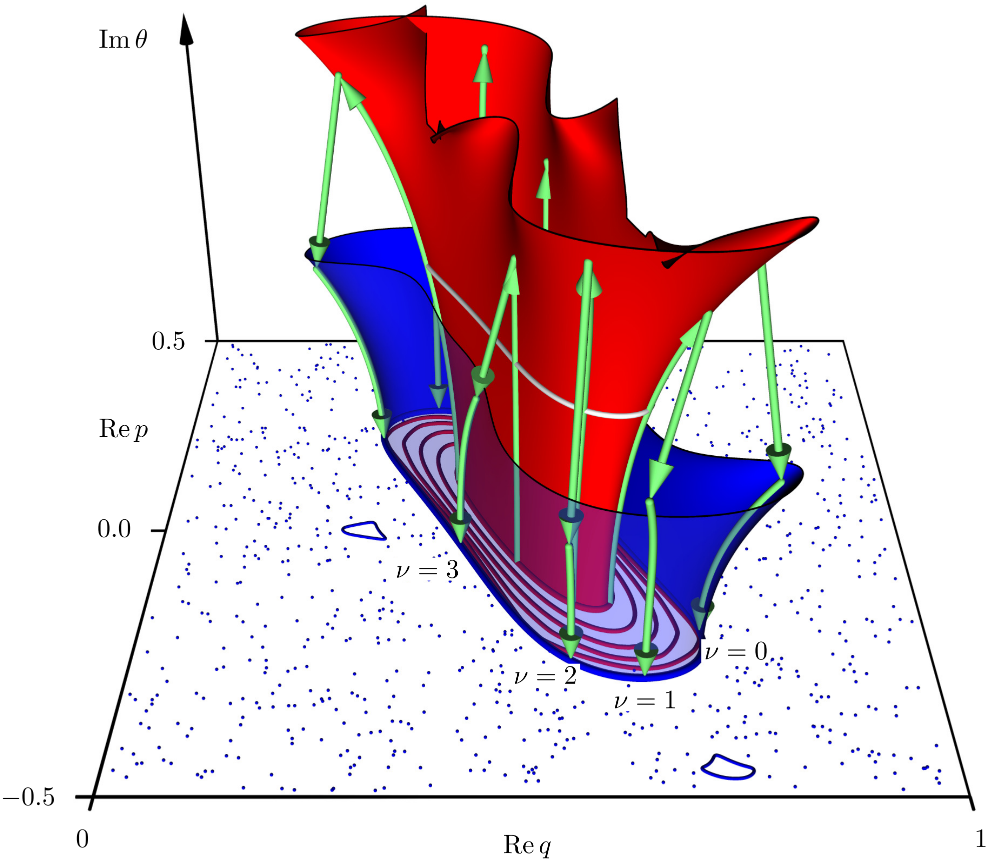

Figure 4.1.: Dominant complex paths (green arrows) for the tunneling rate γ_1 of the standard map at $\kappa = 2.9$ and $h = 1/50$ with $H_{\mathrm{reg}} = H_{\mathrm{abs}}$. The complexified torus I_1 is shown as a projection in red while the complexified torus I'_{b} is shown as a projection in blue. The visualization is simplified by shifting the angle of the end points of segment (S2) by $-\omega_{\mathrm{b}}$ along I'_{b}. Furthermore, only the complex parts of segments (S1) and (S3) are shown. The natural boundary of the corresponding invariant torus of U is shown as a projection (white line) on the initial torus.

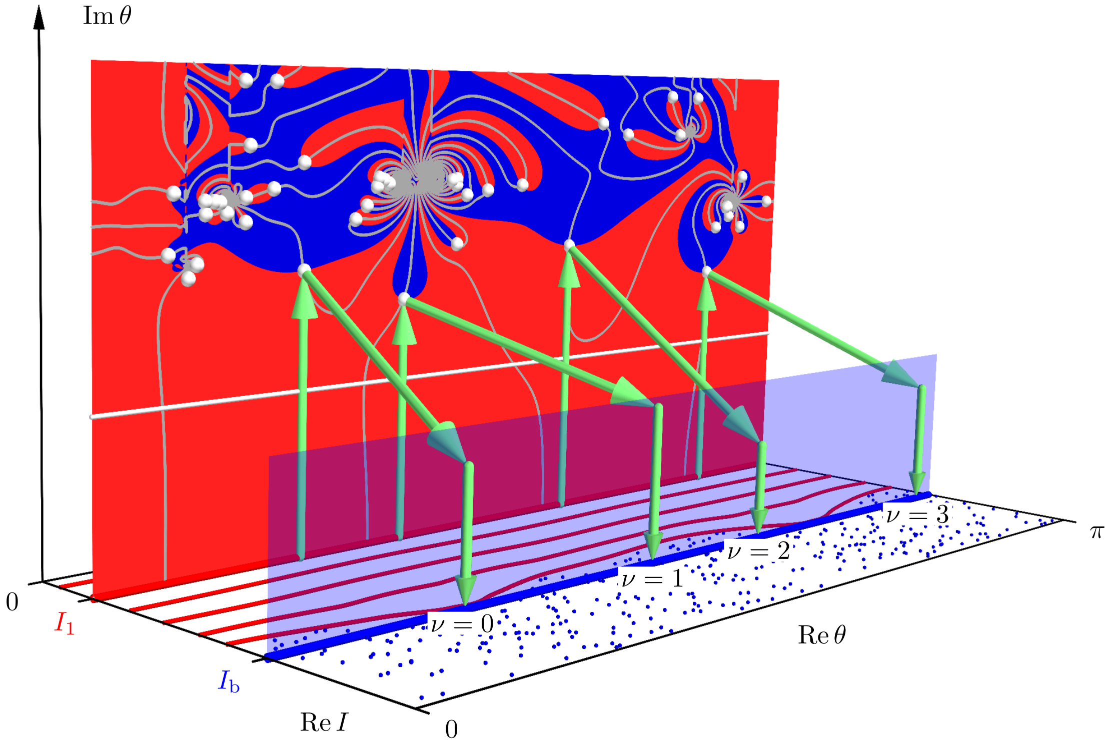

Figure 4.2.: Dominant complex paths (green arrows) for the tunneling rate γ_1 of the standard map at $\kappa = 2.9$ and $h = 1/50$ in action–angle representation with $H_\mathrm{reg} = H_\mathrm{abs}$. The planes are the complexified torus I_1 and the complexified torus I'_b of H_reg. White dots represent points on I_1 which map onto I'_b. They are at the intersection of the gray lines (M-set) with the boundary between red and blue regions. The visualization is simplified by shifting the angle of the end points of segment (S2) by $-\omega_\mathrm{b}$ along I'_b. Furthermore, only the complex parts of segments (S1) and (S3) are shown. The natural boundary is shown as a projection (white line) on the initial torus.

points we exploit that the mapped points of I_m are only on I'_b, if their final energy is equal to the energy E'_b of the boundary torus I'_b. Therefore, we apply a numerical root search on

$$\tilde{H}(\theta) := H_\mathrm{abs}(U(q(I_m, \theta), p(I_m, \theta))) - E'_\mathrm{b}, \tag{4.17}$$

giving the angles θ_ν. In order to find a good initial guess for θ_ν we visualize $\tilde{H}(\theta)$ by plotting the θ-curves where $\operatorname{Im} \tilde{H}(\theta) = 0$. These curves are called M-set as first introduced in Refs. [76, 77]. Since real energies correspond to tori of H_abs with real action, the M-set indicates locations on the complexified torus I_m, that map to tori of H_abs with real action. For the standard map the M-set is shown by gray lines in Fig. 4.2. In this figure we further mark the different phase-space regions the points on the M-set are mapped to. This is achieved by representing points on the complex θ-plane of I_m in red, if $\operatorname{Re} \tilde{H}(\theta) < 0$ or blue, if $\operatorname{Re} \tilde{H}(\theta) > 0$, respectively. This indicates final tori in the regular and the chaotic phase-space region, respectively. The intersections of the gray M-set lines with the blue–red border provide the roots θ_ν of $\tilde{H}(\theta)$, see dots in Fig. 4.2, and thus, the sought for initial points $(q_\nu, p_\nu) = (q(I_m, \theta_\nu), p(I_m, \theta_\nu))$ and end points $(q'_\nu, p'_\nu) = U(q_\nu, p_\nu)$ of the time-evolution segment (S2).

In order to complete construction step (B) we determine the curve $\mathcal{C}_{\mathrm{b},\nu}$ which connects (q'_ν, p'_ν) to the reference point $(q'_\mathrm{b}, p'_\mathrm{b})$ along the final complexified torus I'_b. To this end, we numerically integrate Hamilton's equations backward in imaginary time up to the value $-\mathrm{Im}\ t'_\nu$, giving a curve along the complexified torus I'_b starting from (q'_ν, p'_ν) back to real phase space. From the end point of this curve we integrate Hamilton's equations backward in real time, up to the value $-\mathrm{Re}\ t'_\nu$. This gives a curve along the real torus back to the reference point $(q'_\mathrm{b}, p'_\mathrm{b})$. This involves two optimization procedures giving the integration times which provide the complex angle according to $\theta'_\nu = t'_\nu/(2\pi)$.

This finalizes the construction of segments (S1–S3). The WKB-like segment (S1) is the curve $\mathcal{C}_{m,\nu}$ on the complexification of I_m connecting the reference point (q_m, p_m) to the point (q_ν, p_ν) according to the numerical integration of Hamilton's equations. The time-evolution segment (S2) connects the points (q_ν, p_ν) and (q'_ν, p'_ν) on the complexification of I_m and I'_b, respectively, via the complexified map U. The WKB-like segment (S3) is the curve $\mathcal{C}_{\mathrm{b},\nu}$ on the complexification of I'_b connecting the point (q'_ν, p'_ν) to the reference point $(q'_\mathrm{b}, p'_\mathrm{b})$ according to the numerical integration of Hamilton's equations.

Evaluating actions and selecting dominant paths

In construction step (C) we compute the action $\mathcal{S}_\nu(I'_\mathrm{b}, I_m)$ of the paths ν according to Eq. (4.7). The first and the last contribution originate from the WKB-like segments (S1) and (S3) and can be computed by numerical integration along the curves $\mathcal{C}_{m,\nu}$ and $\mathcal{C}_{\mathrm{b},\nu}$, respectively. The time-evolution segment (S2) contributes the action $\mathcal{S}^U_\nu(q_\nu, p_\nu)$ to Eq. (4.7) which is obtained from the map U. For the standard map this contribution is given by Eq. (2.15) with Eq. (2.3).

We further evaluate the action of all paths ν which have a small imaginary angle θ_ν, see dots in Fig. 4.2. We exclude paths which are close to so-called Laputa flowers [76–78], where the M-set forms petal-like clusters. From the evaluated actions, we exclude paths with negative imaginary action as these paths give rise to unphysical transition probabilities. Subsequently, we select the paths with the smallest imaginary action that dominate Eqs. (4.6), (4.8), and (4.14), see, e. g., green arrows in Figs. 4.2 and 4.1. Note, that this is sufficient for our purposes, while in general a Stokes analysis [66, 67, 77, 124] is required.

Steps (A–C) can also be implemented for regular-to-chaotic tunneling rates from the improved fictitious integrable system approach. To this end, we consider the standard map at $\kappa = 2.9$ with H_reg as before (Eq. (3.40) and Tab. 3.1 of Sect. 3.3.2) and $H_\mathrm{abs}(q, p) = q = I'/(2\pi)$. The boundary tori are $q_\mathrm{min} = 0.2843$ and $q_\mathrm{max} = 1 - q_\mathrm{min}$. The resulting complex paths are shown in Fig. 4.3.

We emphasize that the essential point which allows for constructing regular-to-chaotic complex paths for Eq. (4.14) is our use of approximate complexified tori I_m and I'_b. In contrast to the invariant tori of U these tori do not have natural boundaries such that the WKB-segment (S1) can be extended sufficiently deep into complexified phase space to provide a time-evolution segment (S2) which maps to I'_b. This important fact is illustrated in Figs. 4.1, 4.2, and 4.3, where the natural boundary of the corresponding invariant torus of U is indicated by a white line. Clearly, the time-evolution segments (S2) emanate from parts of the initial torus I_m which are above the natural boundary. For

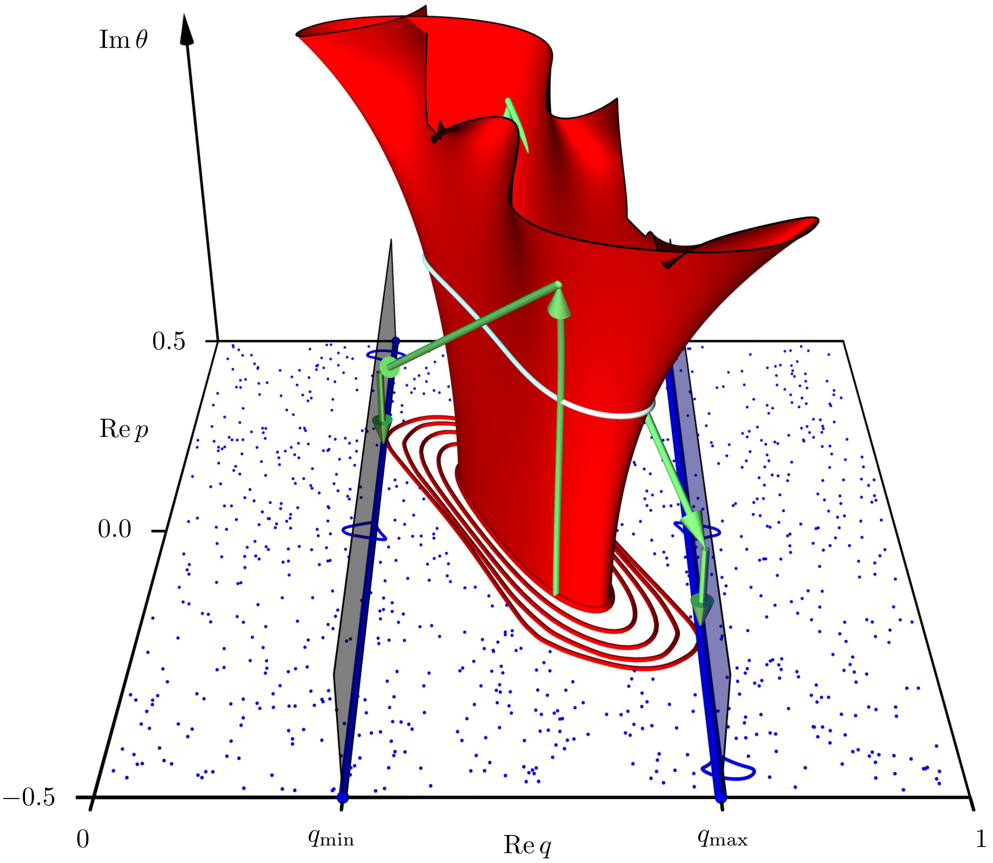

Figure 4.3.: Dominant complex paths (green arrows) for the tunneling rate γ_1 of the standard map at $\kappa = 2.9$ and $h = 1/50$ with H_{reg} as in Eq. (3.40) and $H_{\mathrm{abs}}(q, p) = q$. The complexified torus I_1 is shown as a projection in red while the complexified boundary tori $q_{\min} = 0.2843$ and $q_{\max} = 1 - q_{\min}$ are shown as a projection (depicting Im p instead of Im θ) in blue. Note that only the complex parts of segments (S1) and (S3) are shown. The natural boundary is shown as a projection (white line) on the initial torus.

WKB-like paths in near-integrable systems similar ideas to overcome natural boundaries were used [59, 71, 73, 75].

4.3. Results for the standard map

In this section we show semiclassically predicted regular-to-chaotic tunneling rates γ_m for the standard map at $\kappa = 2.9$. The required paths are constructed according to steps (A–C) as previously described in Sect. 4.2.

4.3.1. Fictitious integrable system approach

We start by considering the semiclassical analog of the fictitious integrable system approach of Refs. [62, 65] with $H_{\mathrm{reg}} = H_{\mathrm{abs}}$ given by Eq. (3.40) and Tab. 3.1 of Sect. 3.3.2.

Regular-to-chaotic tunneling-matrix elements

The first semiclassical result we consider are the regular-to-chaotic tunneling-matrix elements of Eq. (4.6) for the example of $1/h = 50$. We construct each matrix element $\langle I_0|\widehat{U}|I_n\rangle$ from four dominant paths connecting I_0 and I_n in complexified phase space. For each final action I_n these four paths are qualitatively similar to the paths presented in Figs. 4.1 and 4.2. Due to the parity of the standard map U and the fictitious integrable system H_{reg} each of the four paths ν has a symmetry partner. We account for these symmetry partners by doubling the contribution of each path ν in Eq. (4.6). It can further be shown that the interference between symmetry partners semiclassically implements the quantum-mechanical selection rule for the tunneling-matrix elements. We account for this effect by considering only tunneling-matrix elements $\langle I_0|\widehat{U}|I_{2n}\rangle$ between states of the same parity class.

The results are presented in Fig. 4.4 by big black diamonds connected by a black line. The contributions of the four individual paths are presented by the gray underlined small colored diamonds. In order to obtain these results we use Maslov phases $\phi_\nu = 0$. The agreement to quantum data (red circles connected by a red line), numerically obtained by representing the time-evolution operator $\widehat{U}$ of the standard map in the eigenbasis $|I_n\rangle$ of $\widehat{H}_{\text{reg}}$, Eq. (3.50), is acceptable. We observe that the regular-to-chaotic tunneling probabilities decrease with increasing I_n. This behavior is even

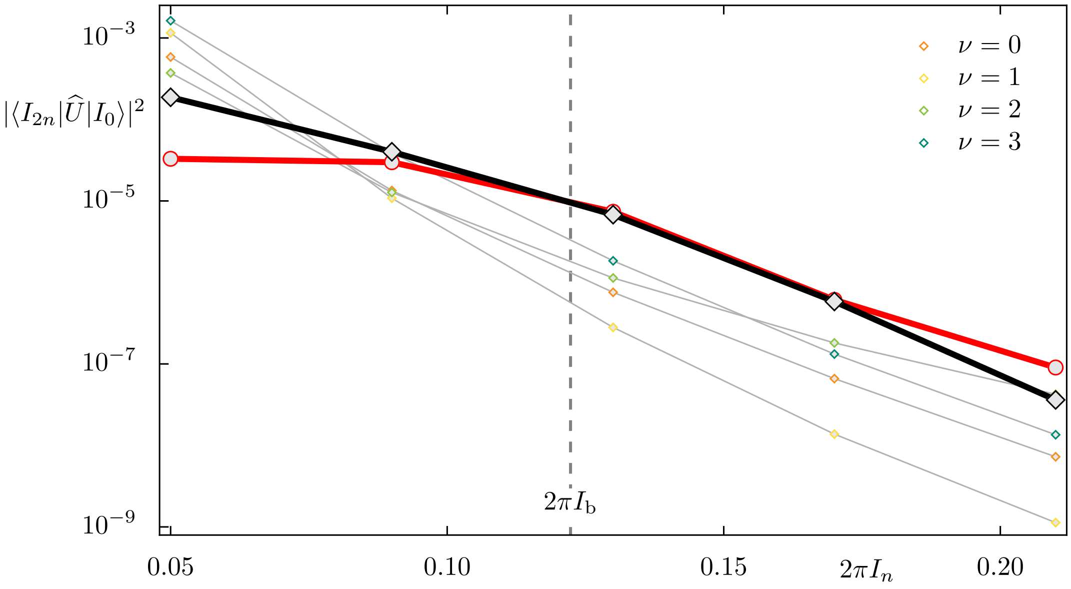

Figure 4.4.: Tunneling probabilities $|\langle I_{2n}|\widehat{U}|I_0\rangle|^2$ versus action $2\pi I_n$ of the final torus for the standard map at $\kappa = 2.9$ and $1/h = 50$. Numerical tunneling probabilities (red circles connected by a thick red line) are obtained from $\widehat{U}$ on toric phase space, represented in the eigenbasis $|I_n\rangle$ of H_{reg}, Eq. (3.50). Semiclassical tunneling probabilities (big diamonds connected by a thick line) are obtained by using Eq. (4.6) together with four dominant paths ν, similar to paths presented in Figs. 4.1 and 4.2. Semiclassical tunneling probabilities corresponding to a single path are presented by small, colored diamonds connected via thin gray lines. The dashed line at $2\pi I_{\text{b}}' = 0.1223$ distinguishes regular-to-regular from regular-to-chaotic tunneling probabilities.

more pronounced for the individual contributions, which decrease roughly exponentially for rising I_n. Therefore the regular-to-chaotic tunneling probability just beyond the boundary of the absorbing region I'_{b} is typically the dominant contribution in Eq. (4.8). This justifies the edge approximation leading to Eq. (4.14). For the presented example in Fig. 4.4 this dominant regular-to-chaotic tunneling probability locates at $2\pi I_n = 0.13$. It requires the combination of all four paths to achieve satisfactory agreement to the numerical result. This is the authors motivation for keeping even the less dominant paths $\nu = 0, 1$ in the following semiclassical prediction of regular-to-chaotic tunneling rates γ_m.

Regular-to-chaotic tunneling rates from summing tunneling-matrix elements

We now take precisely such semiclassical regular-to-chaotic tunneling-matrix elements and sum the resulting tunneling probabilities over all quantizing actions $I'_{ch} > I'_{\mathrm{b}} = 0.1223/(2\pi)$ in the chaotic phase-space region. This gives the semiclassical regular-to-chaotic tunneling rate γ_m according to Eq. (4.8). Note that this corresponds to a semiclassical prediction of regular-to-chaotic tunneling rates according to the fictitious integrable system approach of Refs. [62, 65]. The required matrix elements $\langle I_m|\widehat{U}|I'_{ch}\rangle$ are semiclassically constructed from four dominant paths connecting I_m and I'_{ch}. These paths are qualitatively similar to the paths of Figs. 4.1 and 4.2. As previously discussed the symmetry partners are accounted for by doubling the contribution of each of the paths $\nu = 0, 1, 2, 3$ for tunneling-matrix elements between states of the same symmetry class. This introduces an additional factor of four in our semiclassical prediction of regular-to-chaotic tunneling rates, Eq.(4.8), where due to parity the summation is restricted to contributions from I_m to I'_{ch} with $ch = m + 2n$.

The semiclassical regular-to-chaotic tunneling rates of Eq. (4.8) (underlined diamonds) are presented in Fig. 4.5. They are compared to the corresponding numerical tunneling rates (dots) obtained from Eq. (3.3), with $\widehat{P}_{\mathrm{abs}}$ constructed from $\widehat{H}_{\mathrm{reg}}$ as in Eq. (3.52). Comparing Fig. 4.5 to its quantum-mechanical counterpart, Fig. 3.13, the presented semiclassical predictions are adequate in most regimes of Planck's constant, while being poor especially in the quantum regime, $1/h \approx 25$. The author suspects that these deviation are due to insufficient knowledge on the Maslov phase ϕ_ν which would be required in order to describe the interference between distinct paths correctly. Here we set $\phi_\nu = 0$.

Regular-to-chaotic tunneling rates from edge contributions

We now consider our favored predictions of regular-to-chaotic tunneling rates according to Eq. (4.14), which does not require any Maslov phase. The required semiclassical expressions are constructed from four dominant paths connecting I_m to the boundary torus $I'_{\mathrm{b}} = 0.1223/(2\pi)$. An example of such paths for $I_m = I_1$ at $1/h = 50$ is shown in Figs. 4.1 and 4.2. We implement the parity of U and H_{reg} in Eq. (4.14) by considering only the paths ν without symmetry partners and multiplying the results of Eq. (4.14) with a factor of two. This originates from the following line of reasoning. Accounting for symmetry partners doubles the contribution of each path ν to the regular-to-chaotic tunneling-matrix elements. This gives a factor of four, when summing transition probabilities. Considering that half of these transitions are forbidden by selection rules gives the final factor of two in Eq. (4.14).

The results (lines) are presented in Fig. 4.6. They are compared to the corresponding numerical

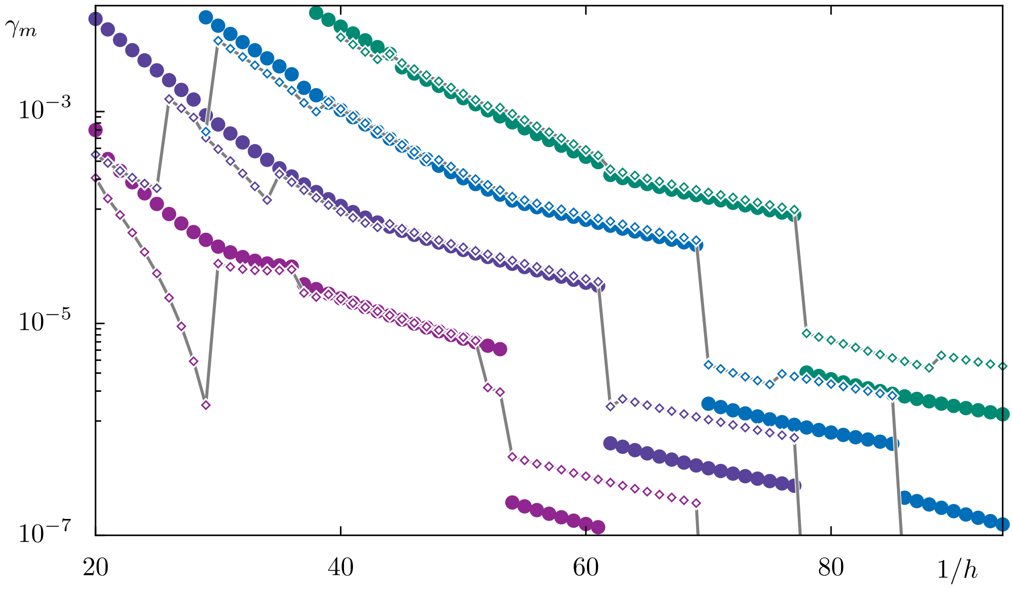

Figure 4.5.: Regular-to-chaotic tunneling rates γ_m of the standard map at $\kappa = 2.9$ for $m = 0, 1, 2, 3$ (bottom to top) versus the inverse effective Planck constant $1/h$. Numerical rates (dots) are obtained from Eq. (3.3) with $\widehat{U}_{\text{open}}$ (3.2) using $\widehat{P}_{\text{abs}}$ as in Eq. (3.52). Semiclassical rates (diamonds connected by lines) are obtained from Eq. (4.8) using four paths ν, as, e. g., presented in Figs. 4.1 and 4.2 for each required transition from I_m to $I'_{ch} > I'_{\text{b}} = 0.1223/(2\pi)$.

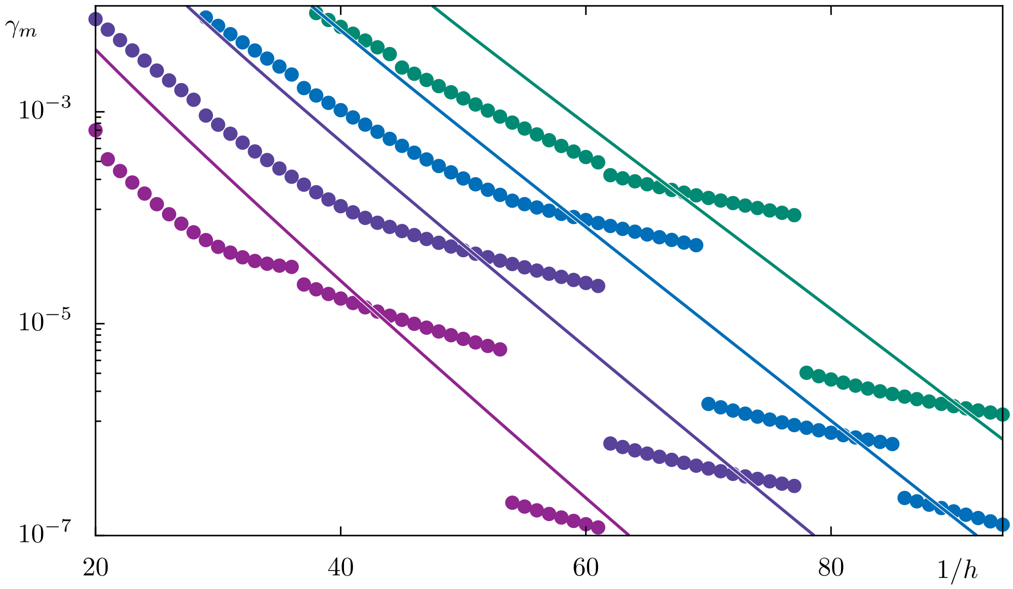

Figure 4.6.: Regular-to-chaotic tunneling rates γ_m of the standard map at $\kappa = 2.9$ versus inverse effective Planck constant $1/h$ for $m = 0, 1, 2, 3$ (bottom to top). Numerical rates (dots) are as in Fig. 4.5. Semiclassical rates (lines) are obtained from Eq. (4.14) using four paths ν, as, e. g., presented in Figs. 4.1 and 4.2 for each required transition from I_m to $I'_{\text{b}} = 0.1223/(2\pi)$.

tunneling rates (dots) obtained from Eq. (3.3), with $\widehat{P}_{\text{abs}}$ constructed from $\widehat{H}_{\text{reg}}$ as in Eq. (3.52). The semiclassical prediction clearly reproduces the exponential decrease of the numerical regular-to-chaotic tunneling rates γ_m for increasing $1/h$. In contrast to Eq. (4.8), Eq. (4.14) fails to reproduce the quantization jumps of the numerical tunneling rates. This is due to approximating the semiclassical information of complex paths ν to each quantizing torus I'_{ch} by the reduced information of complex paths ν to a single boundary torus I'_{b}. Given that this drastically reduces the effort of predicting γ_m, clearly outweighs the loss of quantization jumps and makes Eq. (4.14) favorable over Eq. (4.8) for practical use.

The single-path prediction

Considering that the results of Fig. 4.6 have contributions of four paths, it is an interesting question to understand how much each of these paths contributes to the final result. To this end, we consider the relative contribution of each path $\gamma_{m,\nu}$ to the tunneling rate γ_m in Fig. 4.7. This plot clearly reveals that the tunneling rates γ_m are semiclassically dominated by the path $\nu = 3$. Furthermore, Fig. 4.7 shows that especially the path $\nu = 0$ but also the path $\nu = 1$ have a minor impact on the tunneling rates γ_m. In contrast, the path $\nu = 2$ dominates in the quantum regime of the tunneling rates γ_1, γ_2, and γ_3. Nevertheless, a prediction of regular-to-chaotic tunneling rates according to Eq. (4.14) using only the dominant path $\nu = 3$ gives reasonable results, as can be seen from Fig. 4.8. This allows for the conclusion that Eq. (4.14) represents a generalization of the WKB-like prediction for integrable systems, Eq. (1.1), to non-integrable systems. In that it provides a semiclassical understanding for

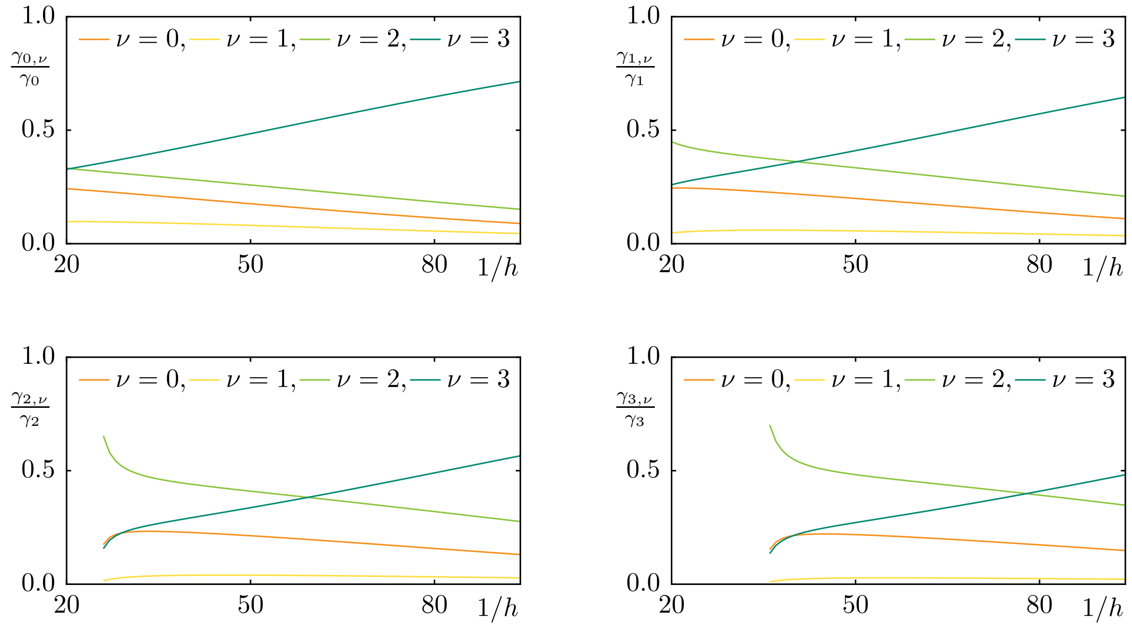

Figure 4.7.: Relative contributions of the paths $\nu = 0, 1, 2, 3$ to the semiclassically predicted regular-to-chaotic tunneling rates γ_m, Eq. (4.14), of Fig. 4.6, for $m = 0, 1, 2, 3$. For an example of the paths ν, see, e. g., Figs. 4.1 and 4.2.

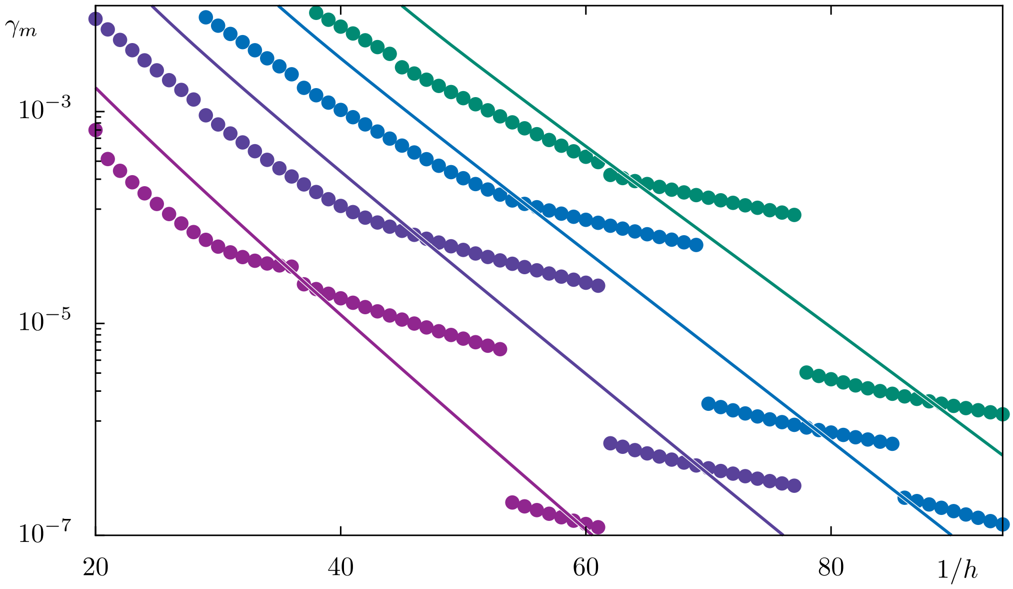

Figure 4.8.: Regular-to-chaotic tunneling rates γ_m of the standard map at $\kappa = 2.9$ versus inverse effective Planck constant $1/h$ for $m = 0, 1, 2, 3$ (bottom to top). Numerical rates are illustrated as in Fig. 4.6. In contrast, the semiclassical rates (lines) are obtained from Eq. (4.14) using only the semiclassically dominant path $\nu = 3$ from I_m to $I'_\mathrm{b} = 0.1223/(2\pi)$. An example of this path is shown in Figs. 4.1 and 4.2.

the exponential decrease of direct regular-to-chaotic tunneling rates with decreasing effective Planck constant h.

4.3.2. Improved fictitious integrable system approach

We now consider semiclassical predictions of regular-to-chaotic tunneling rates of the standard map at $\kappa = 2.9$ corresponding to the improved fictitious integrable system approach of Sect. 3.3. To this end, we keep H_reg according to Eq. (3.40) and Tab. 3.1 of Sect. 3.3.2 but replace the fictitious integrable system for the tori of the absorbing region by $H_\mathrm{abs}(q, p) = q$.

In order to provide this prediction we evaluate Eq. (4.14) using the single dominant complex path $\nu = 0$ which propagates from I_m to the right boundary torus $q_\mathrm{max} = 1.0 - q_\mathrm{min}$ with $q_\mathrm{min} = 0.2843$, see, e. g., Fig. 4.3. Its symmetry partner going to q_min is accounted for by doubling the contribution of the path $\nu = 0$ in Eq. (4.14). The results (lines) are presented in Fig. 4.9. They are compared to the corresponding numerical tunneling rates (dots) obtained from Eq. (3.3), with $\widehat{P}_\mathrm{abs}$ constructed from states of the position lattice, Eq. (2.47) according to Eq. (3.52). The agreement between numerical rates and semiclassical predictions is given within a factor of three. Again the exponential decrease of these direct regular-to-chaotic tunneling rates for decreasing h is semiclassically explained by Eq. (4.14).

Finally we show that Eq. (4.14) can at least predict regular-to-chaotic tunneling rates for absorbing regions just beyond the inner partial barrier. Please see Fig. 3.6 to recall the precise setup. In order

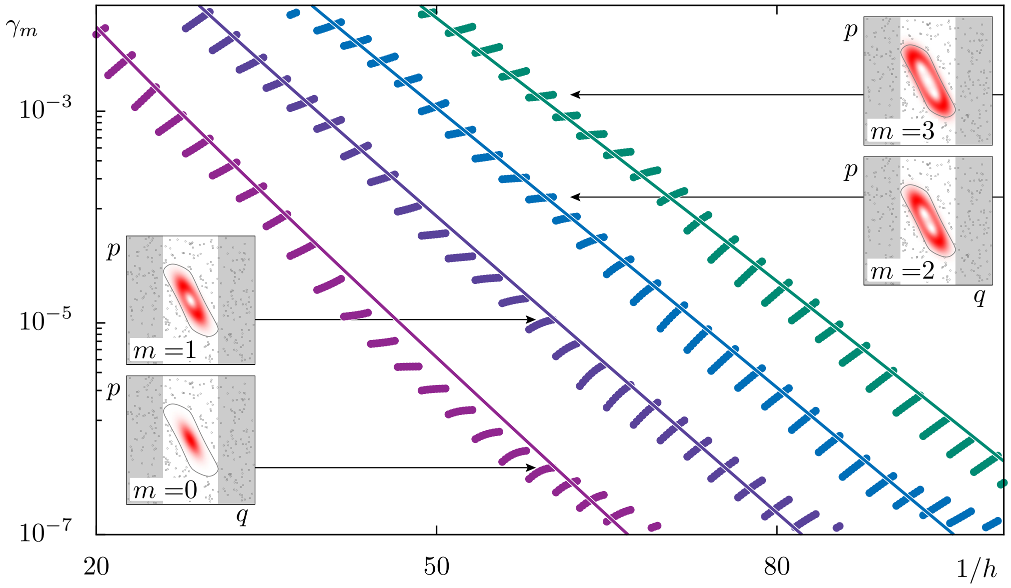

Figure 4.9.: Regular-to-chaotic tunneling rates γ_m of the standard map at $\kappa = 2.9$ versus inverse effective Planck constant $1/h$. Numerical rates (dots) are obtained from Eq. (3.3) with $\widehat{U}_{\text{open}}$, Eq. (3.2), using $\widehat{P}_{\text{abs}}$ as in Eq. (3.51). Semiclassical rates (lines) are obtained from Eq. (4.14)using only the dominant path ν to $q_{\max}$ as, e. g., in Fig. 4.3, for each required transition from I_m to $q_{\min} = 0.2843$ and $q_{\max} = 1.0 - q_{\min}$, respectively.

to predict semiclassical tunneling rates for this absorbing region, $\mathcal{R}_{\text{abs}} = (-\infty, q_{\min}) \cup (q_{\max}, \infty)$ with $q_{\min} = 0.271286$ and $q_{\max} = 1 - q_{\min}$, we evaluate Eq. (4.14) using the single complex path going to the boundary of the absorbing region at $q_{\max}$. We account for the symmetry partner going to $q_{\min}$ by doubling the contribution of the path to $q_{\max}$. These paths are similar to the paths in Fig. 4.3. The results (lines) are presented in Fig. 4.10. Similar as before the agreement between numerical rates and semiclassical predictions is within a factor of three. Also for these tunneling rates, using the single dominant path in Eq. (4.14) semiclassically explains the exponential dependence of direct regular-to-chaotic tunneling rates on the effective Planck constant h. Note that accounting for absorbing regions beyond the outer partial barrier is so far neither quantum-mechanically nor semiclassically possible within the (improved) fictitious integrable system approach. As discussed in Sect. 3.3.5, this problem has to be solved for quantum predictions before meaningful semiclassical results can be expected.

Towards a WKB-like prediction for regular-to-chaotic tunneling rates

A semiclassical version of Eq. (3.31) giving the quantum-mechanical predictions of Fig. 3.11 was not further pursued in this thesis. Nevertheless, we point out that its semiclassical counterpart is encoded in Eq. (4.14) by replacing the time-evolution operator U with the identity map and deleting the corresponding action term in Eq. (4.7). Furthermore, constructing the projector in position representation space, cancels the third action term in Eq. (4.7). In that the semiclassical analog of Eq. (3.31), would be provided by a simple WKB-like action in Eq. (4.14) which is obtained by integrating along a WKB-

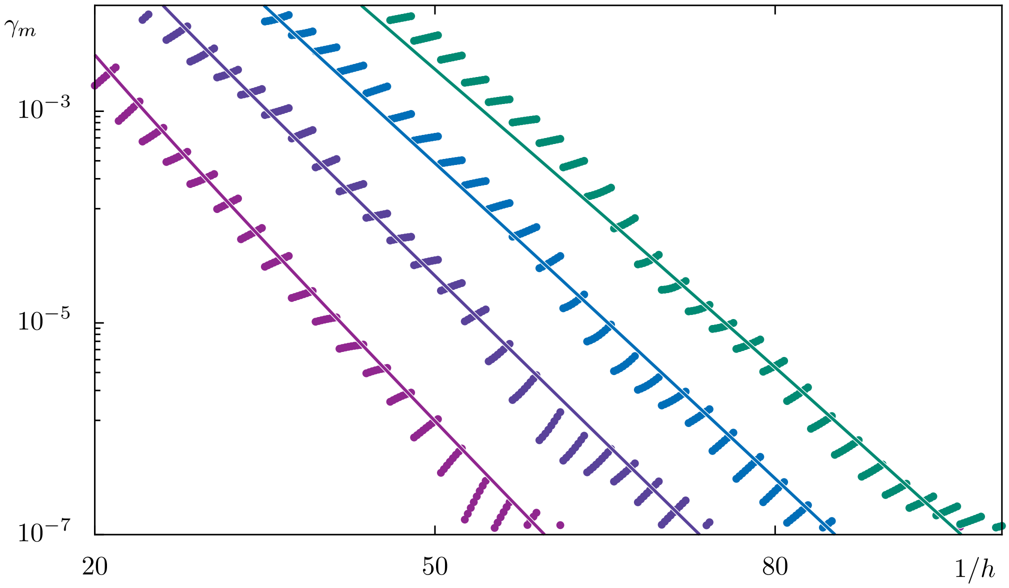

Figure 4.10.: Regular-to-chaotic tunneling rates γ_m of the standard map at $\kappa = 2.9$ versus inverse effective Planck constant $1/h$ for $m = 0, 1, 2, 3$ (bottom to top). Numerical rates (dots) are obtained from Eq. (3.3) with $\widehat{U}_{\text{open}}$, Eq. (3.2), using $\widehat{P}_{\text{abs}}$ as in Eq. (3.51). Semiclassical rates (lines) are obtained from Eq. (4.14) using only the dominant path ν to $q_{\max}$, as, e. g., in Fig. 4.3, for each required transition from I_m to $q_{\min} = 0.271286$ and $q_{\max} = 1.0 - q_{\min}$, respectively.

like segment on the complexified torus I_m up to the boundary of the absorbing region. Pursuing such simple WKB-like predictions is worth investigating in the future.

4.3.3. Discussion

In successfully applying our approach to the direct regular-to-chaotic tunneling rates of the standard map we demonstrate that our semiclassical complex-path approach gives meaningful results. Especially, in showing that Eq. (4.14) can predict regular-to-chaotic tunneling rates based on a single complex path, provides a semiclassical explanation for the exponential decrease of direct regular-to-chaotic tunneling rates with decreasing h.

Despite its success, our approach does not allow for describing effects of resonance-assisted tunneling, yet. Furthermore, it is so far only possible to successfully predict tunneling rates for absorbing regions close to the regular phase-space region. As discussed in detail in Sect. 3.3.5, overcoming these limitations requires regular basis states, which mimic the corresponding metastable eigenstate of the open system. Therefore, including effects of resonance-assisted tunneling requires regular basis states, which mimic the localization properties of metastable eigenstates on multiple quantizing tori. Furthermore, describing tunneling rates for absorbing regions far away from the regular phase-space region within a semiclassical version of the fictitious integrable system approach, requires regular basis states which mimic localization properties of metastable eigenstates on the hierarchical phase-space region. Both tasks are challenging and must be solved for quantum predictions, before a semiclassical prediction is feasible.

In contrast, open problems of the current semiclassical approach include the correct determination of Maslov phases ϕ_ν and a more careful consideration of the Stokes phenomenon. Furthermore, it remains an open question whether the presented complex paths hint at an invariant, classical structure which controls regular-to-chaotic tunneling in non-integrable systems with a mixed phase space. For tunneling in integrable systems such an invariant structure is the complexified torus connecting disconnected regions of the real phase space in complexified phase space. For regular-to-chaotic tunneling it is suggested in Refs. [80–82] that such a structure is provided by the complexified stable and unstable manifolds of the complexified chaotic phase-space region. However, a connection of our tunneling paths to these structures has not been investigated yet. In the future this is a project worth investigating.

4.4. Tunneling paths in complexified phase space

In this section, we construct the invariant tori of the non-integrable system U and compare them to the corresponding tori of the fictitious integrable system H_{reg}. This comparison confirms the essential geometrical picture behind our complex-path approach, namely that the approximate tori of H_{reg} extend beyond the natural boundary of the corresponding invariant tori of the non-integrable system. In that the WKB-like segment (S1) of our complex paths can be extended sufficiently deep into complexified phase space in order to find a time-evolution segment (S2) which maps to a complexified torus of the absorbing region.

In contrast to the first implementation of complexified tori by Green and Percival, who parametrized the real tori by analytic functions and considered the analytic continuation of these functions into complexified phase space, Refs. [24, 25], we construct the complexified regular tori from the dynamics of the complexified map, similar to Ref. [60, Appendix. B]. For a more general introduction to the complexified phase space, we refer the reader to Refs. [79–82, 125], which also discuss the embedding of tunneling paths in complexified phase space. Furthermore, Refs. [126–129] which make rigorous mathematical statements on the complexified phase space of polynomial maps are recommended. Note that the work presented here is based on results and numerical implementations of my co-workers Konstantin Clauß, Ref. [130], and Arnd Bäcker.

Definition of complexified tori

According to Refs. [24, 25], a complexified torus T_ω of the standard map is a two-dimensional manifold, which is parametrized by a complex angle θ,

$$T_\omega := \left\{ \big(q_\omega(\theta),\, p_\omega(\theta)\big) \in \mathbb{C}^2 \,:\, \theta = \theta_{\mathrm{r}} + \mathrm{i}\theta_{\mathrm{i}} \in \big([0, 2\pi) + \mathrm{i}(-\bar{\theta}_{\mathrm{i},\omega}, \bar{\theta}_{\mathrm{i},\omega})\big) \right\}, \tag{4.18}$$

up to the imaginary angle $\bar{\theta}_{\mathrm{i},\omega}$ corresponding to the natural boundary at which the analyticity of the functions $q_\omega(\theta)$ and $p_\omega(\theta)$ breaks along a dense line of singularities. This torus is invariant under the dynamics of the complexified map U. More specifically, applying U to a point on the torus is equivalent to shifting the corresponding complex angle by the real number ω, Refs. [24, 25],

$$U(q_\omega(\theta),\, p_\omega(\theta)) = (q_\omega(\theta+\omega),\, p_\omega(\theta+\omega)). \tag{4.19}$$

Hence, the complexified torus T_ω is a collection of one-dimensional invariant curves parametrized by the real angle coordinate θ_r at fixed imaginary angle θ_i according to

$$O_{\omega,\theta_\mathrm{i}}(\theta_\mathrm{r}) := \left\{ \big(q_\omega(\theta_\mathrm{r}+\mathrm{i}\theta_\mathrm{i}),\, p_\omega(\theta_\mathrm{r}+\mathrm{i}\theta_\mathrm{i})\big) \in \mathbb{C}^2 \;:\; \theta_\mathrm{r} \in [0, 2\pi) \right\}. \tag{4.20}$$

Along these curves the orbits of U wind with frequency ω. If $\omega/(2\pi)$ is irrational, $O_{\omega,\theta_\mathrm{i}}(\theta_\mathrm{r})$ is explored densely by any orbit of U. Note that each of these invariant curves is determined by the choice of the imaginary angle θ_i, which indicates its depth along the complexified torus T_ω in complexified phase space. For later reference, recall that the curve defined by fixing $\theta_\mathrm{r} = 0$,

$$C_\omega(\theta_\mathrm{i}) := \left\{ \big(q_\omega(\mathrm{i}\theta_\mathrm{i}),\, p_\omega(\mathrm{i}\theta_\mathrm{i})\big) \in \mathbb{C}^2 \;:\; \theta_\mathrm{i} \in (-\bar{\theta}_{\mathrm{i},\omega}, \bar{\theta}_{\mathrm{i},\omega}) \right\}, \tag{4.21}$$

parametrizes the invariant curves of the complexified torus in terms of the complex angle θ_i.

Symmetrized standard map

In order to construct the complexified tori of the standard map, we now switch from its after-kick to its half-free representation,

$$q' = q + p + \frac{\kappa}{4\pi}\sin\left(2\pi\left[q + \frac{p}{2}\right]\right), \tag{4.22a}$$
$$p' = p + \frac{\kappa}{4\pi}\sin\left(2\pi\left[q + \frac{p}{2}\right]\right). \tag{4.22b}$$

This is convenient, since the symmetries of the standard map become easier accessible, i. e., the half-free representation has real tori which have a mirror symmetry along the line $p = 0$, see real phase-space plane in Fig. 4.11. Given that θ is defined such that the point $q_\omega(\theta = 0)$ and $p_\omega(\theta = 0)$ is on that symmetry line, the real tori fulfill

$$q_\omega(\theta) = q_\omega(-\theta), \tag{4.23}$$
$$p_\omega(\theta) = -p_\omega(-\theta), \tag{4.24}$$

respectively. Hence, assuming $q_\omega(\theta)$ and $p_\omega(\theta)$ are analytic functions of the angle, the general form of their power-series expansion reads

$$q_\omega(I,\theta) = \sum_{n\in\mathbb{N}} a_n \theta^{2n}, \tag{4.25}$$
$$p_\omega(I,\theta) = \sum_{n\in\mathbb{N}} b_n \theta^{2n+1}. \tag{4.26}$$

From these relations we infer that the curve $C_\omega(\theta_\mathrm{i})$, Eq. (4.21), which parametrizes the invariant curves of the complexified torus T_ω has purely real positions and purely imaginary momenta. Hence, the intersection of each complexified torus with the two-dimensional plane

$$P := \{q, p \, : \mathrm{Im}\, q = 0, \mathrm{Re}\, p = 0\}, \tag{4.27}$$

is a one-dimensional line. Note that this property follows from the symmetry of the standard map, and is specific for the plane P. In contrast an arbitrary two-dimensional plane in the four-dimensional complexified phase space typically intersects a two-dimensional complexified torus in points.

Survival times of the complex P-plane

In order to identify the curves $C_\omega(\theta_\mathrm{i}) \subset P$ we study the survival times of orbits originating from the complex P-plane. To this end we define a survival box around the central fixed point,

$$(\mathrm{Re}\, q, \mathrm{Im}\, q, \mathrm{Re}\, p, \mathrm{Im}\, p) \in [0.0, 1.0] \times [-0.5, 0.5] \times [-0.5, 0.5] \times [-0.5, 0.5]. \tag{4.28}$$

Subsequently, we iterate the points (q, p) of the complex P-plane and determine the time $n_\mathrm{max}(q, p)$ which the corresponding orbit $U^n(q, p)$, survives in the above box. The results are presented in Figs. 4.11 and 4.12(a), respectively. Here, we show points on P in red if they survive for 2000 iterations. On the other hand, points which exit the survival box, Eq. (4.28), are colored in blue, with dark blue indicating short survival times n_max and light blue indicating survival times n_max almost up to 2000 iterations.

The blue-colored points of P numerically approximate the intersection of P with the forward Fatou set F^+, consisting of points which are transported to infinity forward in time. On the other hand, the red-colored points of P numerically approximate the intersection of P with the forward filled Julia set K^+, consisting of points which remain bounded under the complexified time-evolution of U. Here, the notation is chosen as in Refs. [80–82]. By definition the curves $C_\omega(\theta_\mathrm{i})$ on P give rise to orbits along the invariant curves $O_{\omega,\theta_\mathrm{i}}(\theta_\mathrm{r})$ on the torus T_ω. Hence, these curves are also a subset of the filled Julia set $C_\omega(\theta_\mathrm{i}) \subset P \cap K^+$ and should be contained in the red region of the survival time plot in Fig. 4.11. A magnification of this region is shown in Fig. 4.12(a). A projection of an example orbit along an invariant curve $O_{\omega,\theta_\mathrm{i}}(\theta_\mathrm{r})$ emanating from $C_\omega(\theta_\mathrm{i})$ on $P \cap K^+$ is shown by a gray line in Fig. 4.11. This illustrates that while the curve $C_\omega(\theta_\mathrm{i})$ parametrizing the invariant curves $O_{\omega,\theta_\mathrm{i}}(\theta_\mathrm{r})$ of T_ω is embedded in P, the orbits initiated from $C_\omega(\theta_\mathrm{i})$ map along $O_{\omega,\theta_\mathrm{i}}(\theta_\mathrm{r})$, and thus, explore the parts of T_ω which are not on P.

Constructing complexified tori

In order to construct the tori T_ω from the dynamics of U, we now group the initial points on P which belong to the trapped orbits of K^+ according to their frequency ω. In order to numerically obtain this frequency for each point $(q, p) \in P \cap K^+$ we use the analysis of fundamental frequencies [120] on

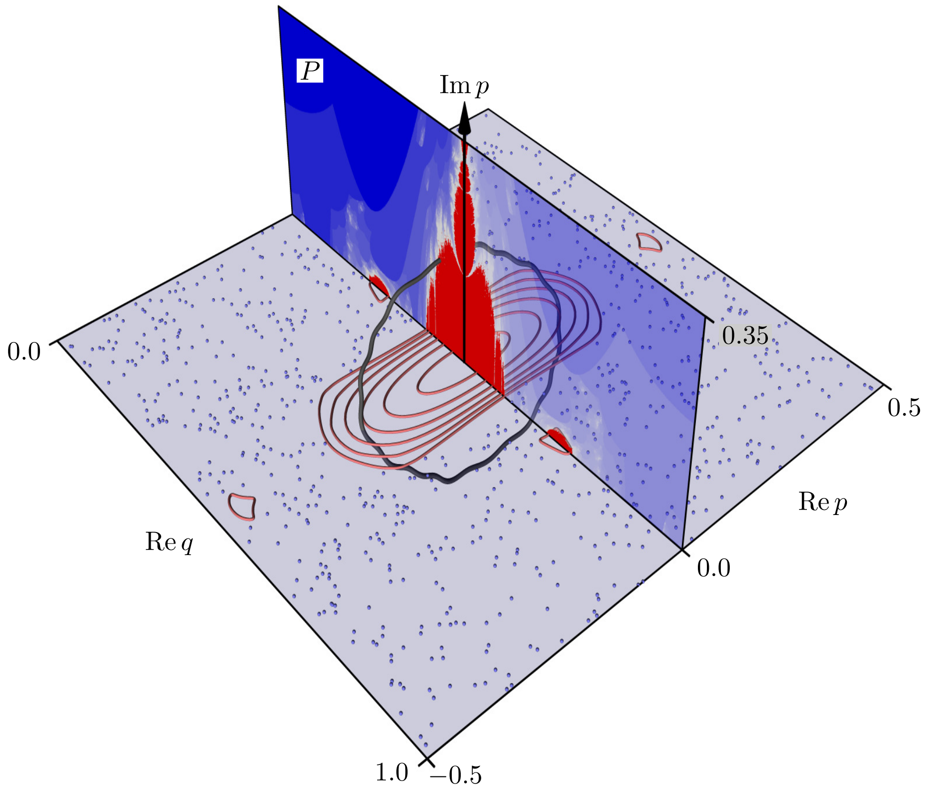

Figure 4.11.: Phase space of the complexified standard map, Eq. (4.22), at $\kappa = 2.9$. Real plane showing the real phase space. Survival times of points on the complex P-plane ($\mathrm{Re}\, p = 0$, $\mathrm{Im}\, q = 0$) are shown in red for bound orbits and blue for escaping orbits, with dark blue indicating short and light blue long survival times, respectively. An example orbit (gray line) is shown as a projection.

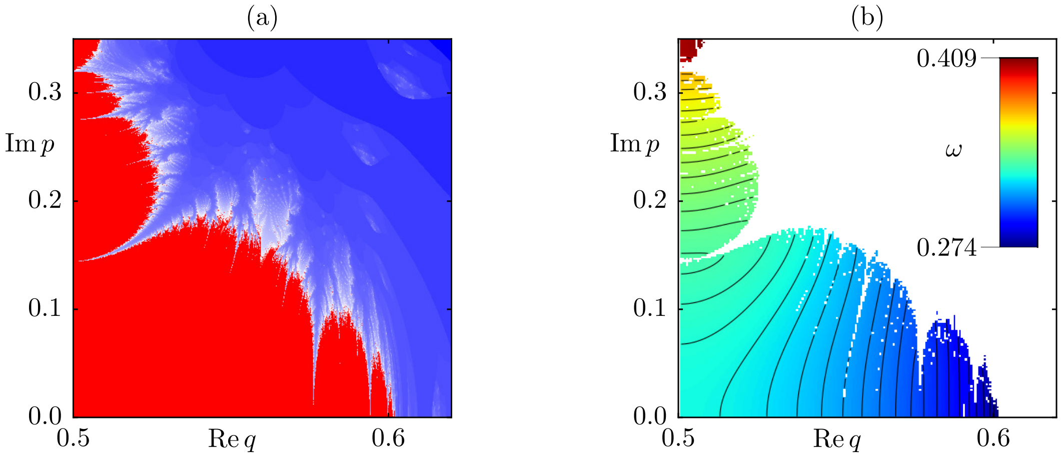

Figure 4.12.: Magnified region of the complex P-plane of Fig. 4.11. (a) Survival times of points on P ($\mathrm{Re}\, p = 0$, $\mathrm{Im}\, q = 0$). Red regions indicate initial conditions of bound orbits while blue indicates initial conditions for escaping orbits, with dark blue indicating short and light blue long survival times, respectively. (b) Frequencies ω of the surviving orbits of (a).

the real phase-space coordinates of the corresponding orbit $U^n(q,p)$. A preliminary overview of the frequencies of orbits initiated on $P \cap K^+$ is shown in Fig. 4.12(b). These frequencies are presented by a color map. Additional contour lines indicate the curves $C_\omega(\theta_\mathrm{i})$, connecting from the real phase space $\operatorname{Im} p = 0$ up to the natural boundary where $C_\omega(\theta_\mathrm{i})$ ends. Note that $P \cap K^+$ is interspersed with white channels in Fig. 4.12 indicating the fractal structure of the set $P \cap K^+$, and thus, the erratic fluctuations of the depth up to which a curve $C_\omega(\theta_\mathrm{i})$ extends into complexified phase space.

We now give a precise construction of complexified tori. The presented algorithm essentially follows the implementation of Ref. [60, Appendix. B]. We start by determining the real torus of U corresponding to a specific action I, e. g., the action I_1 at $1/h = 50$. Using the numerical analysis of fundamental frequencies [120], we determine its frequency $\omega(I)$. Starting from the intersection point of this real torus with P we ascend into complexified phase space along the curve $C_{\omega(I)}(\theta_\mathrm{i})$. Since this curve is not known, we ascend into complexified phase space along P by first increasing the coordinate $\operatorname{Im} p$ by a small amount. At this value we fix $\operatorname{Im} p$ and determine the corresponding coordinate $\operatorname{Re} q$ on $C_{\omega(I)}(\theta_\mathrm{i})$ by numerically searching for the initial condition ($\operatorname{Im} p$, $\operatorname{Re} p$) on P, which gives rise to the orbit with frequency $\omega(I)$. By repeating this procedure we successively obtain points along the curve $C_{\omega(I)}(\theta_\mathrm{i})$. Using these points as initial conditions for the complexified map gives orbits along the corresponding invariant curve $O_{\omega(I),\theta_\mathrm{i}}(\theta_\mathrm{r})$. The collection of these curves represents the torus $T_{\omega(I)}$.

The complexified torus I_1 at $1/h = 50$ of the standard map at $\kappa = 2.9$ is presented in Fig. 4.13. Here, we visualize the torus, Eq. (4.18), by plotting

$$(\operatorname{Re} q_{\omega(I)}(\theta), \operatorname{Re} p_{\omega(I)}(\theta), \operatorname{Im} p_{\omega(I)}(\theta_\mathrm{i})). \tag{4.29}$$

This visualization is convenient since it assigns each invariant curve along the complexified torus a uniform depth in complexified phase space. Especially, the depth up to which the analytic continuation of a torus extends is intuitively visualized by the numerical approximation of the natural boundary, see the gray line in Fig. 4.13. Furthermore, this presentation gives meaningful connections both to the survival time plot in the plane P and to the real phase space. Therefore, the red colored region of the survival plot nicely indicates how deep the continuation of neighboring tori extends into complexified phase space.

Tunneling paths in complexified phase space

Finally, we compare the complexified torus of Fig. 4.13 to the corresponding torus of H_reg presented in Fig. 4.1. To this end, we symmetrize all data of Fig. 4.1 by mapping points (q,p) to points $(q + p/2, p)$. Furthermore, the imaginary angle coordinates of Fig. 4.1 are transformed to the corresponding imaginary momenta according to the function $\operatorname{Im} p(I_1, \theta_\mathrm{i})$ which describes the intersection of the plane P with the symmetrized approximate torus I_1 of H_reg. The result is presented in Fig. 4.14. This picture shows the generic embedding of tunneling paths according to the presented semiclassical complex-path approach in complexified phase space. In using complexified tori of a fictitious integrable system (light red), we suitably approximate the corresponding tori of the non-integrable map U (lighter red) up to

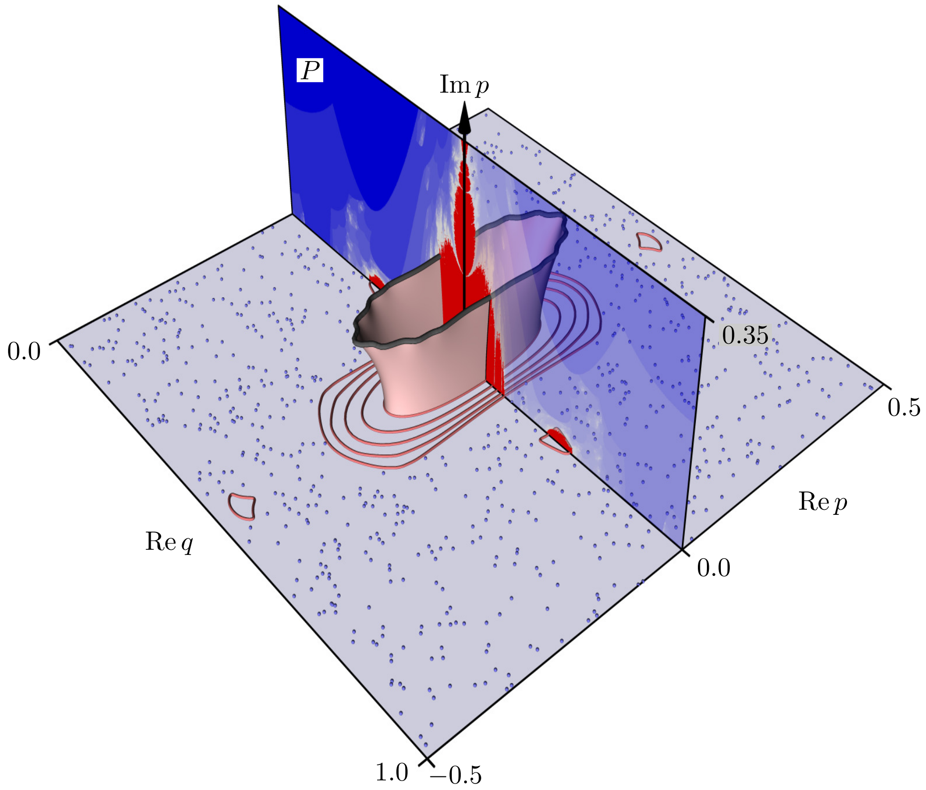

Figure 4.13.: Complexified quantizing torus I_1 of the standard map, Eq. (4.22), at $\kappa = 2.9$ and $h = 1/50$. The quantizing torus (light red) is presented according to Eq. (4.29), see text for details. The gray line illustrates its natural boundary. Real plane showing the real phase space. Survival times of points on the complex P-plane ($\mathrm{Re}\, p = 0$, $\mathrm{Im}\, q = 0$) are shown in red for bound orbits and blue for escaping orbits, with dark blue indicating short and light blue long survival times, respectively.

the natural boundary (gray line). These integrable approximations of the original tori do not have a natural boundary, and thus, extend beyond the natural boundary of the corresponding torus of U. In that they extend beyond the regular region of complexified phase space into the chaotic region of complexified phase space. This fact allows for extending the WKB-segment (S1) of our complex paths sufficiently deep into complexified phase space such that the time-evolution segment (S2) can map to a fictitious complexified torus of the absorber in the chaotic phase-space region. This geometrical picture completes our chapter on complex paths for regular-to-chaotic tunneling rates.

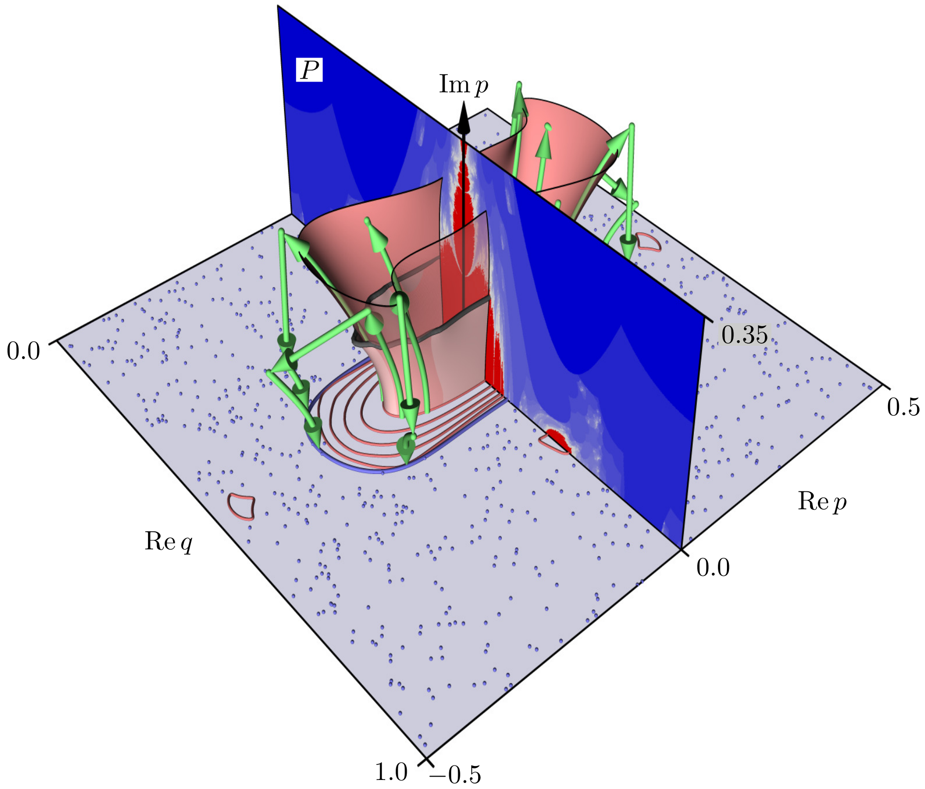

Figure 4.14.: Embedding of complex tunneling paths (green arrows) into the complexified phase space of the standard map, at $\kappa = 2.9$ and $h = 1/50$. The projection of the complexified quantizing torus I_1 (short, light red) and its natural boundary (gray line) is compared to the corresponding torus of H_{reg} (longer, slightly darker light red). The real plane shows the real phase space. Survival times of points on the complex P-plane ($\mathrm{Re}\, p = 0$, $\mathrm{Im}\, q = 0$) are shown in red for bound orbits and blue for escaping orbits, with dark blue indicating short and light blue long survival times, respectively.

5. Summary and outlook

In this thesis we have developed a semiclassical complex-path approach for regular-to-chaotic tunneling rates. It combines the quantum-mechanical predictions of the fictitious integrable system approach [62, 65] with the semiclassical time-evolution method of complex tunneling paths [76–82]. In that it brings together two important research lines on regular-to-chaotic tunneling in non-integrable systems. The main result of our complex-path approach is Eq. (4.14), which predicts direct regular-to-chaotic tunneling rates semiclassically. The fundamental accomplishment, and thus, the success of our complex-path approach is the existence of the required complex paths. The essential ingredient which allows for their construction is the use of approximate regular tori, e. g., from a fictitious integrable system H_{reg}. In contrast to the invariant regular tori of non-integrable systems, these approximate tori do not have natural boundaries. This allows for extending WKB-like segments along the approximate regular torus into the chaotic region of the complexified phase space, such that a subsequent time-evolution can reach the absorber which is embedded in the complexified chaotic phase-space region. While this thesis represents the first implementation of such an idea for non-integrable systems, similar ways to overcome natural boundaries were used in near-integrable systems before [59, 71, 73, 75]. Remarkably, Eq. (4.14) also gives a semiclassical justification for the long-conjectured [83] and often-observed [40, 42, 43, 47, 50, 65], exponential h-scaling of direct regular-to-chaotic tunneling rates. Finally, this thesis demonstrates the applicability of the presented complex-path approach by successfully predicting regular-to-chaotic tunneling rates of the standard map from a single complex path.

Our results lead to several open questions: The current complex-path approach can so far not account for the enhancement of regular-to-chaotic tunneling rates due to resonance-assisted tunneling [59–61, 63]. Therefore, it is applicable only in the quantum regime where Planck's constant is comparable to the size of the regular phase-space region, $h \lesssim A_{\text{reg}}$. Including resonance-assisted tunneling into the discussed complex-path approach seems feasible by constructing integrable systems H_{reg} which include nonlinear-resonance chains. A subsequent semiclassical treatment of such H_{reg} similar to Refs. [60, App. C] and [63, 131] should allow for including resonance-assisted tunneling into the presented complex-path approach.

The current complex-path approach does further not include the effects of partial transport barriers [27, 111, 112] in the hierarchical phase-space region on regular-to-chaotic tunneling rates. Therefore, our semiclassical predictions are only applicable for regular-to-chaotic tunneling rates of systems where the hierarchical phase-space region is either negligible or contained in the absorbing region. As discussed in detail in Sect. 3.3.5 this problem already exists for the quantum-mechanical predictions of regular-to-chaotic tunneling rates. Its solution within the fictitious integrable system approach requires a construction of regular basis states which mimic localization properties of metastable eigenstates on the hierarchical phase-space region. In the eyes of the author this is a challenging task.

Even though we expect the presented complex-path approach to apply not only to the standard map, but also to experimentally relevant systems, such as microwave billiards [47–50], optical microcavities [42–46], or atoms and molecules [32, 34, 36, 38–40], an implementation of our method for these systems is still an open problem. For billiards and microcavities it seems most promising to implement our complex-path approach by exploiting the corresponding boundary map of these systems. This map is two-dimensional, and thus, highly analogous to the standard map. On the other hand, an extension of the presented complex-path approach to higher-dimensional systems is required. For such systems we believe that the tunneling rate is still given by complex paths from an approximate torus of the regular region to tori of the absorbing region. This would follow from a generalization of Eq. (4.8) with the prefactor replaced by the determinant of the stability matrix. However, several new challenges arise: (i) Regular regions are formed by a collection of regular tori interwoven with threads of the Arnold web [84, 132, 133]. Even when ignoring the complications due to the Arnold web, the boundary of the regular region is now given by a family of boundary tori. (ii) The construction of approximate tori requires new methods. (iii) The search algorithm for complex paths has to be generalized to higher dimensions. (iv) It is not clear, if a simplification analogous to Eq. (4.14) is possible.

Despite its successful use for predictions of regular-to-chaotic tunneling rates of quantum maps [62, 64, 65, 116], billiards [50], and optical microcavities [43] it remains an open question to establish precise criteria, which guarantee the applicability of the fictitious integrable system approach. For the presented complex-path approach this leads to the puzzling effect that two distinct integrable approximations of the regular phase-space region in terms of two different integrable systems H_{reg} can give results of similar quality, using tunneling paths with entirely different locations in the complexified phase space. One possible way to solve this problem within our complex-path approach might be the use of local approximations to the invariant torus of the regular region, e. g., in terms of a Fourier expansion as presented in Refs. [24, 25]. This would provide a more controllable approximation process. Inevitably, the above discussion leads to the most important question of regular-to-chaotic tunneling, namely: Which invariant classical structure of the complexified phase space governs regular-to-chaotic tunneling rates? In view of the presented results this question remains open. As argued by Shudo and Ikeda in Refs. [80–82] this structure is provided by the complexified stable and unstable manifolds of the chaotic phase-space region. A connection of these structures to our complex tunneling paths is not obvious and requires a detailed investigation.

As a closing remark of this thesis we point out that the presented complex-path approach to regular-to-chaotic tunneling rates is so far conceptually constructed from the properties of a closed system. However, regular-to-chaotic tunneling rates are defined for an open system. In the future it is worth investigating, if using properties of such open systems allows for accessing tunneling rates more easily. A first idea in this direction was discussed in Sect. 3.3 by showing that regular-to-chaotic tunneling rates can quantum mechanically be evaluated from the time evolution of the corresponding metastable eigenstates, Eq. (3.16). This prediction does not require approximate regular basis states and includes both the effects of resonance-assisted tunneling and partial transport barriers. Therefore, if a semiclassical expression for metastable eigenstates was known, it would provide the ideal starting point for a semiclassical evaluation of regular-to-chaotic tunneling rates.

Appendix

A. The method of steepest descent

The method of steepest descent is a powerful mathematical tool which is widely used in semiclassical physics. This appendix aims at giving a short and intuitive introduction to this method for a reader who never used a saddle-point approximation before. The presentation essentially follows the presentation in Ref. [92].

A.1. The method of steepest descent in one dimension

In the following let us consider integrals of the form

$$\int_{\mathcal{C}} \mathrm{d}x \exp\left(\frac{f(x)}{\hbar}\right), \tag{A.1}$$

where the contour $\mathcal{C}$ is such that x is a real integration variable in the interval $[x_{\mathrm{min}}, x_{\mathrm{max}}]$ and f is an analytic real-valued function. It is the goal to approximate this integral in the limit that $\hbar \to 0$. Hence, we can consider its analytic continuation as a function of the complex coordinate $z := x + \mathrm{i}y$ and split f into its real and its complex part

$$f(x + \mathrm{i}y) := u(x, y) + \mathrm{i}v(x, y). \tag{A.2}$$

Due to the analyticity of f it is possible to show that both u and v are harmonic functions, i. e., $\Delta u = 0$, $\Delta v = 0$. Hence, u and v exhibit a saddle-point structure in the neighborhood of a stationary point z_μ, which fulfills

$$\frac{\mathrm{d}f(z_\mu)}{\mathrm{d}z} = 0. \tag{A.3}$$

Furthermore, it follows from the analyticity of f that the level sets of v are the lines of steepest descent or ascent in u and vice versa [92].

In order to exploit these facts we split the integrand in Eq. (A.1) in two exponentials which describe its modulus and its phase separately,

$$\int_{\mathcal{C}} \mathrm{d}x \exp\left(\frac{u(x, y)}{\hbar}\right) \exp\left(\mathrm{i}\frac{v(x, y)}{\hbar}\right). \tag{A.4}$$

From $u(x, y)$ being a harmonic function, we conclude that the modulus of the integrand $\exp\left(u(x, y)/\hbar\right)$

can be visualized as a landscape over the complex plane that never shows a local maximum or minimum, but only saddle points. Subsequently, we assume we can deform the contour $\mathcal{C}$ into a new contour $\mathcal{C}'$ such that $\mathcal{C}'$ passes through a subset of saddle points z_ν of $u(x,y)$ along the level sets of constant $v(x,y)$. In that, $\mathcal{C}'$ follows the path of steepest descent of $\exp\left(u(x,y)/\hbar\right)$ into the valleys on both sides of a saddle point z_ν. If no singularities of $f(z)$ have been passed during the transformation, we have

$$\int_{\mathcal{C}} \mathrm{d}x \exp\left(\frac{f(x)}{\hbar}\right) = \int_{\mathcal{C}'} \mathrm{d}z \exp\left(\frac{u(x,y)}{\hbar}\right) \exp\left(\mathrm{i}\frac{v(x,y)}{\hbar}\right) \tag{A.5}$$

by Cauchy's theorem.

Finally, we come to the actual approximation in the method of steepest descent, which is sometimes also called saddle-point approximation. To this end, we need to realize that the most important contributions to the integral in Eq. (A.5) along $\mathcal{C}'$ originate from the neighborhood of those saddle points z_ν through which the contour $\mathcal{C}'$ passes. This is the case because along $\mathcal{C}'$ the modulus of the integrand $\exp\left(u(x,y)/\hbar\right)$ has a local maximum at z_ν, while $\exp\left(\mathrm{i}v(x,y)/\hbar\right)$ gives a constant phase integrating along $\mathcal{C}'$. In the limit $\hbar \to 0$ the local maximum of $\exp\left(u(x,y)/\hbar\right)$ becomes more and more amplified, such that significant contributions originate from an ever smaller neighborhood of the saddle point z_ν. To evaluate this contribution approximately, one expands the function $f(z)$ around this saddle point,

$$f(z) \approx f(z_\nu) + \frac{1}{2}\frac{\mathrm{d}^2 f}{\mathrm{d}z^2}(z_\nu)(z-z_\nu)^2. \tag{A.6}$$

such that

$$\int_{\mathcal{C}} \mathrm{d}x \exp\left(\frac{f(x)}{\hbar}\right) \approx \sum_\nu \exp\left(\frac{f(z_\nu)}{\hbar}\right) \int_{\mathcal{C}_\nu} \mathrm{d}z \exp\left(\frac{1}{2\hbar}\frac{\mathrm{d}^2 f(z_\nu)}{\mathrm{d}z^2}(z-z_\nu)^2\right), \tag{A.7}$$

where $\mathcal{C}_\nu$ is a straight line in the complex plane tangential to $\mathcal{C}'$ in the saddle point z_ν. Since the integrals in the arising contribution are Gaussians which have their significant contributions in the small neighborhood of the saddle point z_ν we only make a tiny error by extending $\mathcal{C}_\nu$ infinitely in the complex plane.

It now remains our task to compute a set of Gaussian integrals in complex space. To this end, we introduce χ_ν by

$$\frac{\mathrm{d}^2 f}{\mathrm{d}z^2}(z_\nu) = \left|\frac{\mathrm{d}^2 f}{\mathrm{d}z^2}(z_\nu)\right| \exp\left(\mathrm{i}\chi_\nu\right), \tag{A.8}$$

and parametrize the integration contour $\mathcal{C}_\nu$ by

$$\sqrt{\frac{\left|\frac{\mathrm{d}^2 f}{\mathrm{d}z^2}(z_\nu)\right|}{2\hbar}}(z-z_\nu) = s\exp\left(\mathrm{i}\varphi_\nu\right), \tag{A.9}$$

with $s \in \mathbb{R}$ and $\varphi_\nu \in [0, 2\pi)$ picking the direction of the contour $\mathcal{C}_\nu$. As a consequence, we have

$$\int_{\mathcal{C}} \mathrm{d}x \exp\left(\frac{f(x)}{\hbar}\right) \approx \sum_\nu \sqrt{\frac{2\hbar}{\left|\frac{\partial^2 f}{\partial z^2}(z_\nu)\right|}} \exp\left(\frac{f(z_\nu)}{\hbar} + \mathrm{i}\varphi_\nu\right) \int\limits_{-\infty}^{\infty} \mathrm{d}s \exp\left(-s^2 e^{\mathrm{i}[\pi+\chi_\nu+2\varphi_\nu]}\right). \tag{A.10}$$

We can now deduce φ_ν from χ_ν as

$$\varphi_\nu = \pi r_\nu - \frac{\pi + \chi_\nu}{2}, \tag{A.11}$$

where r_ν is an integer which has to be chosen such that the contour $\mathcal{C}_\nu$ is integrated along the correct direction. For integrals with $x_{\text{min}} < x_{\text{max}}$, φ_ν is typically in the range $[-\pi/2, \pi/2]$ indicating that $\mathcal{C}_\nu$ is followed towards rising real part. This makes a unique choice of r_ν possible. These manipulations give the final result,

$$\int_{\mathcal{C}} \mathrm{d}x \exp\left(\frac{f(x)}{\hbar}\right) \approx \sum_\nu \exp\left(\mathrm{i}\pi r_\nu - \frac{\pi + \chi_\nu}{2}\right) \sqrt{\frac{2\pi\hbar}{\left|\frac{\partial^2 f}{\partial z^2}(z_\nu)\right|}} \exp\left(\frac{f(z_\nu)}{\hbar}\right), \tag{A.12}$$

which is sometimes formally written as

$$\int_{\mathcal{C}} \mathrm{d}x \exp\left(\frac{f(x)}{\hbar}\right) \approx \sum_\nu (-1)^{r_\nu} \sqrt{\frac{-2\pi\hbar}{\frac{\partial^2 f}{\partial z^2}(z_\nu)}} \exp\left(\frac{f(z_\nu)}{\hbar}\right). \tag{A.13}$$

Note, that along the same lines of reasoning, the method of steepest descent can be generalized to integrals of the form

$$\int_{\mathcal{C}} \mathrm{d}x\, g(x) \exp\left(\frac{f(x)}{\hbar}\right) \approx \sum_\nu g(z_\nu) \exp\left(\mathrm{i}\pi r_\nu - \frac{\pi + \chi_\nu}{2}\right) \sqrt{\frac{2\pi\hbar}{\left|\frac{\partial^2 f}{\partial z^2}(z_\nu)\right|}} \exp\left(\frac{f(z_\nu)}{\hbar}\right). \tag{A.14}$$

A.2. Applying the method of steepest descent in physics

When being faced with an integral like Eq. (A.14) in semiclassical physics, we can solve it in the spirit of the method of steepest descent along the following steps:
(i) We search for saddle points $z_\nu \in \mathbb{C}$, $\nu \in \mathbb{N}$, in f, i. e.,

$$\frac{\mathrm{d}f(z_\nu)}{\mathrm{d}z} =: f'(z_\nu) = 0. \tag{A.15}$$

(ii) We compute $f''(z_\nu)$ giving $|f''(z_\nu)|$ while $\varphi_\nu = \pi r_\nu - \frac{\pi+\chi_\nu}{2}$ is typically chosen from the interval $[-\frac{\pi}{2}, \frac{\pi}{2}]$. In step (iii) this gives

$$\int_{\mathcal{C}} \mathrm{d}x\, g(x) \exp\left(\frac{f(x)}{\hbar}\right) \approx \sum_\nu g(z_\nu) \exp\left(\varphi_\nu\right) \sqrt{\frac{2\pi\hbar}{\left|\frac{\partial^2 f}{\partial z^2}(z_\nu)\right|}} \exp\left(\frac{f(z_\nu)}{\hbar}\right). \tag{A.16}$$

Applying a saddle-point method in this way bears many pitfalls which one has to be aware of. A collection of such problems shall be discussed here, briefly. The first assumption, which has to hold for applying the method of steepest descent is that the deformation of the integration contour $\mathcal{C}$ into the contour $\mathcal{C}'$ which passes through the saddle points z_ν is possible. Even in this case, it might be necessary to pass isolated singularities which give additional contributions to the integral. In a physical context, one sometimes calls such contributions diffraction contributions, as they arise from sharp non-analytic changes in the integrand. Furthermore, if the deformation of the integration contour into $\mathcal{C}'$ is possible, it can still happen that the most important contributions to the integral originate from the edges of $\mathcal{C}'$ close to the points x_{min} or x_{max}. In that case, a different approximation strategy for these edge terms is necessary. Moreover, it is possible that a careful deformation of the integration contour into $\mathcal{C}'$ yields that only a subset of all saddle points of $f(z)$ actually contributes to the final integral. However, such a deformation cannot always be controlled and hence one needs so-called *pruning* rules in order to select the right saddle points which contribute to the integral. Finally, at some saddle points z_ν it is possible that $f''(z_\nu)$ is also zero. In that case one has to expand $f(z)$ to cubic order leading to Airy instead of Gaussian integrals. In physics, this problem arises at turning points, where an additional Maslov-phase shift has to be considered.

B. Derivation of complex paths for regular-to-chaotic tunneling-matrix elements

In this Appendix, we derive semiclassical expressions for the regular-to-chaotic tunneling-matrix elements $\langle I'_{ch}|\widehat{U}|I_m\rangle$ of Eq. (4.5). In order to illuminate how classical paths in complexified phase space arise in a semiclassical evaluation of regular-to-chaotic tunneling-matrix elements, the derivation is presented in great detail. The result, Eq. (4.6), gives exactly the one-step version of the semiclassical propagator presented in Ref. [81]. It is summarized in Sect. 4.1.2.

B.1. Semiclassical expressions for the basis states and the propagator

We start our derivation of semiclassical tunneling-matrix elements $\langle I'_{ch}|\widehat{U}|I_m\rangle$ by inserting the position representation,

$$\langle I'_{ch}|\widehat{U}|I_m\rangle = \int \mathrm{d}q' \int \mathrm{d}q \; \langle I'_{ch}|q'\rangle \, \langle q'|\widehat{U}|q\rangle \, \langle q|I_m\rangle \,. \tag{B.1}$$

In order to transform Eq. (B.1) into a semiclassical expression, the initial basis state $\langle q|I_m\rangle$, the propagator $\langle q'|\widehat{U}|q\rangle$, and the final basis state $\langle I'_{ch}|q'\rangle$ are subsequently replaced by their semiclassical counter parts.

In order to achieve such expressions for the basis states we use the result of Miller [134],

$$\langle q|I_m\rangle = \sum_{\mu} \sqrt{\frac{1}{2\pi \mathrm{i}\hbar} \frac{\partial^2 \mathcal{F}_{\mu}^{(2)}(q, I_m)}{\partial q\, \partial I_m}} \exp\left(\frac{\mathrm{i}}{\hbar} \mathcal{F}_{\mu}^{(2)}(q, I_m)\right), \tag{B.2}$$

$$\langle I'_{ch}|q'\rangle = \sum_{\sigma} \sqrt{\frac{1}{2\pi \mathrm{i}\hbar} \frac{\partial^2 \mathcal{F}_{\mu}^{(3)}(I'_{ch}, q')}{\partial I'_{ch}\, \partial q'}} \exp\left(\frac{\mathrm{i}}{\hbar} \mathcal{F}_{\sigma}^{(3)}(I'_{ch}, q')\right). \tag{B.3}$$

This makes explicit use of the canonical transformations, Eqs. (4.4) and (4.3), which ensures the existence of the required type-two generating function $\mathcal{F}_{\mu}^{(2)}(q, I)$ and the type-three generating function $\mathcal{F}_{\sigma}^{(3)}(I', q')$, respectively.

Differentiating $\mathcal{F}_{\mu}^{(2)}(q, I)$ with respect to q gives the momentum

$$p_{\mu}(q, I) = \frac{\partial \mathcal{F}_{\mu}^{(2)}(q, I)}{\partial q}, \tag{B.4}$$

on the torus of action I at the toruses intersection with the plane of positions q. Since this function arises from solving Eq. (4.3) for p, it can be multi-valued. This is accounted for by the index μ. Further, differentiating $\mathcal{F}_{\mu}^{(2)}(q, I)$ with respect to I gives the corresponding angle,

$$\theta_{\mu}(q, I) = \frac{\partial \mathcal{F}_{\mu}^{(2)}(q, I)}{\partial I}. \tag{B.5}$$

Analogously, differentiating $\mathcal{F}_{\sigma}^{(3)}(I', q')$ with respect to q' gives the momentum

$$p'_{\sigma}(I', q') = -\frac{\partial \mathcal{F}_{\sigma}^{(3)}(I', q')}{\partial q'}, \tag{B.6}$$

on the torus of action I' at the toruses intersection with the plane of position q'. Since this function arises from solving Eq. (4.4) for p', it can also be multi-valued. This is accounted for by the index σ. Further, differentiating $\mathcal{F}_{\sigma}^{(3)}(I', q')$ with respect to I' gives the corresponding angle,

$$\theta'_{\sigma}(I', q') = -\frac{\partial \mathcal{F}_{\sigma}^{(3)}(I', q')}{\partial I'}. \tag{B.7}$$

For the following derivation it is important to keep in mind that (q, p_{μ}) denotes a point on the initial torus I, while (q', p'_{σ}) denotes a point on the final torus I'.

For the propagator, we use the general semiclassical expression

$$\langle \tilde{q}'|\widehat{U}|\tilde{q}\rangle = \sum_{\nu} \sqrt{\frac{\mathrm{i}}{2\pi\hbar} \frac{\partial^2 \mathcal{S}_{\nu}^{U}(\tilde{q}', \tilde{q})}{\partial \tilde{q}'\, \partial \tilde{q}}} \exp\left(\frac{\mathrm{i}}{\hbar} \mathcal{S}_{\nu}^{U}(\tilde{q}', \tilde{q})\right). \tag{B.8}$$

Here, $\mathcal{S}_{\nu}^{U}(\tilde{q}', \tilde{q})$ is the action of a path ν which maps from $\tilde{q}$ to $\tilde{q}'$ via the classical map U. This action is a type-one generating function, which encodes the information about initial and final momenta of the path ν according to

$$\tilde{p}'_\nu(\tilde{q}', \tilde{q}) = \frac{\partial \mathcal{S}^U_\nu(\tilde{q}', \tilde{q})}{\partial \tilde{q}'}, \tag{B.9}$$

$$\tilde{p}_\nu(\tilde{q}', \tilde{q}) = -\frac{\partial \mathcal{S}^U_\nu(\tilde{q}', \tilde{q})}{\partial \tilde{q}}. \tag{B.10}$$

These equations originate from solving the map $(\tilde{q}', \tilde{p}') = U(\tilde{q}, \tilde{p})$ for $\tilde{p}$, $\tilde{p}'$, i. e., by finding paths from $\tilde{q}$ to $\tilde{q}'$. Since this is a boundary-value problem it can have multiple solutions. This is accounted for by the index ν. Note that the above presentation is not restricted to the standard map but holds for general time-periodic systems whose classical dynamics is described by the stroboscopic map U over unit time.

We now take the semiclassical expressions Eqs. (B.2), (B.3), and (B.8) and insert them into Eq. (B.1),

$$\begin{aligned}
\langle I'_{ch}|\widehat{U}|I_m\rangle = \sum_{\sigma,\nu,\mu} \int \mathrm{d}q \int \mathrm{d}q' \, \frac{1}{(2\pi\hbar)^{3/2}} \sqrt{\frac{1}{\mathrm{i}} \frac{\partial^2 \mathcal{F}^{(3)}_\sigma(I'_{ch}, q')}{\partial I'_{ch}\, \partial q'} \frac{\partial^2 \mathcal{S}^U_\nu(q', q)}{\partial q'\, \partial q} \frac{\partial^2 \mathcal{F}^{(2)}_\mu(q, I_m)}{\partial q\, \partial I_m}} \\
\times \exp\left(\frac{\mathrm{i}}{\hbar}\left[\mathcal{F}^{(3)}_\sigma(I'_{ch}, q') + \mathcal{S}^U_\nu(q', q) + \mathcal{F}^{(2)}_\mu(q, I_m)\right]\right) \qquad \text{(B.11)} \\
\overset{\text{(B.4), (B.7), (B.10)}}{=} \sum_{\sigma,\nu,\mu} \int \mathrm{d}q \int \mathrm{d}q' \, \frac{1}{(2\pi\hbar)^{3/2}} \sqrt{\mathrm{i} \frac{\partial \theta'_\sigma(I'_{ch}, q')}{\partial q'} \frac{\partial \tilde{p}'_\nu(q', q)}{\partial q} \frac{\partial p_\mu(q, I_m)}{\partial I_m}} \\
\times \exp\left(\frac{\mathrm{i}}{\hbar}\left[\mathcal{F}^{(3)}_\sigma(I'_{ch}, q') + \mathcal{S}^U_\nu(q', q) + \mathcal{F}^{(2)}_\mu(q, I_m)\right]\right). \qquad \text{(B.12)}
\end{aligned}$$

In that the initial position $\tilde{q}$ of the path ν is immediately identified with a position q on the initial torus I_m. Analogously, the final position $\tilde{q}'$ of the path ν is identified with a position q' on the final torus I'_{ch}. This allows for omitting the tilde symbol on the position coordinates. In contrast to positions q, q', which are from now on always attached to the tori I_m, I'_{ch}, respectively, the initial and final momenta $\tilde{p}$, $\tilde{p}'$ of the path ν are still unrelated to the tori I_m, I'_{ch}.

B.2. Method of steepest descent – The cradle of complex paths

In order to evaluate the integrals in Eq. (B.12) semiclassically, we apply the method of steepest descent [91, 92], see App. A for a short introduction. This amounts to approximating the integrals in Eq. (B.12) by Gaussian integrals, which arise from a second order expansion of the exponent function in Eq. (B.12) around its saddle points. See the details below.

The *first step* of the steepest-descent method requires to define the exponent function, composed from the action $\bar{\mathcal{S}}$,

$$h(q', q) := \mathrm{i}\bar{\mathcal{S}}(q', q) := \mathrm{i}\left[\mathcal{F}^{(3)}_\sigma(I'_{ch}, q') + \mathcal{S}^U_\nu(q', q) + \mathcal{F}^{(2)}_\mu(q, I_m)\right]. \tag{B.13}$$

This function depends on the integration coordinates q and q'. It further has a parametric dependence on the actions I_m and I'_{ch}. Note that these actions correspond to physical observables which determine the representation of the considered tunneling-matrix element $\langle I'_{ch}|\widehat{U}|I_m\rangle$. Therefore, I_m and I'_{ch} are always real in the following.

The *second step* of the steepest-descent method requires to identify the saddle-point positions of $h(q',q)$, i. e., we have to search for positions at which the gradient of $h(q',q)$ vanishes,

$$0 \overset{!}{=} \frac{\partial \mathcal{S}^U_\nu(q',q)}{\partial q} + \frac{\partial \mathcal{F}^{(2)}_\mu(q,I_m)}{\partial q}, \tag{B.14}$$

$$0 \overset{!}{=} \frac{\partial \mathcal{F}^{(3)}_\sigma(I'_{ch},q')}{\partial q'} + \frac{\partial \mathcal{S}^U_\nu(q',q)}{\partial q'}. \tag{B.15}$$

Using Eqs. (B.4), (B.6), (B.9), and (B.10), gives the saddle-point conditions, which determine the saddle-point positions q, q' implicitly,

$$\tilde{p}_\nu(q',q) \overset{!}{=} p_\mu(q,I_m), \tag{B.16}$$

$$p'_\sigma(I'_{ch},q') \overset{!}{=} \tilde{p}'_\nu(q',q). \tag{B.17}$$

These conditions provide the essential semiclassical connection between regular-to-chaotic tunneling-matrix elements and classical paths of U, which map from the torus I_m to the torus I'_{ch}. In order to realize this, recall that q and q' are already positions on the tori I_m and I'_{ch}, respectively. Hence, for positions which solve the saddle-point equations, the corresponding initial momentum $\tilde{p}_\nu$ of the path ν coincides with the corresponding momentum p_μ on the initial torus I_m, Eq. (B.16). Similarly, for positions which solve the saddle-point equations, the corresponding final momentum $\tilde{p}_\nu$ of the path ν coincides with the corresponding momentum p'_σ on the final torus I'_{ch}, Eq. (B.17). Hence, searching for saddle-point positions is equivalent to searching for paths ν which map via U from the torus I_m to the torus I'_{ch}. This allows for labeling the solutions of the saddle-point conditions by the index ν,

$$q_\nu = q_\nu(I'_{ch}, I_m), \tag{B.18}$$

$$q'_\nu = q'_\nu(I'_{ch}, I_m). \tag{B.19}$$

For regular-to-chaotic tunneling-matrix elements, identifying saddle-points which solve Eqs. (B.16) and (B.17) contains an additional twist. This twist is obvious, when thinking of saddle-points in terms of classical paths. The tori I_m and I'_{ch} localize in dynamically separated phase-space regions. So how can there be saddle-points which corresponds to a path mapping from I_m to I'_{ch}?

The correct answer to this question is provided by realizing that there cannot be a classical path of U, which connects I_m and I'_{ch} in real phase space, i. e., there are no real solutions for Eqs. (B.16) and (B.17). However, the method of steepest descent allows for resorting to complex saddle points [92]. This is implemented in our integral approximation by exploiting Cauchy's theorem and deforming the integration contours in Eq. (B.12) across complex saddle points. This procedure assumes that the integrand in Eq. (B.12) is analytic in q and q'. Note that this implies analyticity for the momentum and angle functions, Eqs. (B.4), (B.5), (B.6), (B.7), (B.9), and (B.10). When using the method of steepest descent with complexified saddle points, Eqs. (B.16) and (B.17) become two complex equations for two complex saddle points. It is essential to note that even a complex saddle-point solution of Eqs. (B.16) and (B.17) is equivalent to a classical path which maps from I_m to I'_{ch} via the map U. However, now the complex saddle-point solution corresponds to a complex path, which maps from a point on the complexified torus I_m to a point on the complexified torus I'_{ch} via the complexified map U.

After finding the paths ν which connect I_m and I'_{ch}, we can express the indexes μ and σ as $\mu(\nu)$ and $\sigma(\nu)$, respectively. This allows for defining the complex coordinates of the path ν, p_ν, θ_ν, p'_ν, and θ'_ν, which correspond to the complex saddle points q_ν and q'_ν as functions of the real actions I_m and I'_{ch},

$$p_\nu(I'_{ch}, I_m) := \tilde{p}_\nu(q'_\nu(I'_{ch}, I_m), q_\nu(I'_{ch}, I_m)) \overset{(\text{B.16})}{=} p_{\mu(\nu)}(q_\nu(q', I_m), I_m), \tag{B.20}$$

$$\theta_\nu(I'_{ch}, I_m) := \theta_{\mu(\nu)}(q_\nu(I'_{ch}, I_m), I_m), \tag{B.21}$$

$$p'_\nu(I'_{ch}, I_m) := \tilde{p}'_\nu(q'_\nu(I'_{ch}, I_m), q_\nu(I'_{ch}, I_m)) \overset{(\text{B.17})}{=} p'_{\sigma(\nu)}(I'_{ch}, q'_\nu(I'_{ch}, I_m)), \tag{B.22}$$

$$\theta'_\nu(I'_{ch}, I_m) := \theta_{\sigma(\nu)}(I'_{ch}, q'_\nu(I'_{ch}, I_m)). \tag{B.23}$$

The *third step* of the steepest-descent method requires to evaluate the function $h(q, q')$, Eq. (B.13), at the saddle points. We do this by defining the complex action of the path ν,

$$\bar{\mathcal{S}}_\nu(I'_{ch}, I_m) := \mathcal{F}^{(3)}_{\sigma(\nu)}(I'_{ch}, q'_\nu(I'_{ch}, I_m)) + \mathcal{S}^U_\nu(q'_\nu(I'_{ch}, I_m), q_\nu(I'_{ch}, I_m)) + \mathcal{F}^{(2)}_{\mu(\nu)}(q_\nu(I'_{ch}, I_m), I_m). \tag{B.24}$$

Note that this function can be shown to fulfill the properties of a type-four generating function

$$\frac{\partial \bar{\mathcal{S}}_\nu(I'_{ch}, I_m)}{\partial I'_{ch}} = -\theta'_\nu(I'_{ch}, I_m), \tag{B.25}$$

$$\frac{\partial \bar{\mathcal{S}}_\nu(I'_{ch}, I_m)}{\partial I_m} = \theta_\nu(I'_{ch}, I_m) \tag{B.26}$$

by using Eqs. (B.4), (B.5), (B.6), (B.7), (B.9), (B.10), (B.20), (B.21), (B.22), and (B.23).

The *fourth step* of the steepest-descent method requires to compute the determinant of the Hessian of $h(q', q)$, Eq. (B.13), at the saddle points

$$\det \operatorname{Hess} h(q', q) = \left[-\frac{\partial \tilde{p}_\nu(q', q)}{\partial q'} \frac{\partial \tilde{p}'_\nu(q', q)}{\partial q} - \left(\frac{\partial \tilde{p}_\nu(q', q)}{\partial q} - \frac{\partial p_{\mu(\nu)}(q, I_m)}{\partial q} \right) \cdot \left(\frac{\partial p'_{\sigma(\nu)}(I'_{ch}, q')}{\partial q'} - \frac{\partial \tilde{p}'_\nu(q', q)}{\partial q'} \right) \right] \Bigg|_{q'=q'_\nu,\, q=q_\nu} . \tag{B.27}$$

The *fifth step* of the steepest-descent method requires to evaluate the arising Gaussian integrals as approximations to the integrals in Eq. (B.12). This gives the semiclassical regular-to-chaotic tunneling-matrix elements [91, 92],

$$\begin{aligned}\langle I'_{ch}|\widehat{U}|I_m\rangle &= \frac{1}{(2\pi \mathrm{i}\hbar)^{1/2}} \sum_{\nu} \exp\left(\frac{\mathrm{i}}{\hbar}\bar{\mathcal{S}}(I'_{ch}, I_m)\right) \\ &\times \sqrt{\frac{\frac{\partial {\theta'}_{\sigma(\nu)}(I'_{ch},q')}{\partial q'} \cdot \frac{\partial \tilde{p}'_{\nu}(q',q)}{\partial q} \cdot \frac{\partial p_{\mu(\nu)}(q,I_m)}{\partial I_m}}{\frac{\partial \tilde{p}_{\nu}(q',q)}{\partial q'}\frac{\partial \tilde{p}'_{\nu}(q',q)}{\partial q} + \left(\frac{\partial \tilde{p}_{\nu}(q',q)}{\partial q} - \frac{\partial p_{\mu(\nu)}(q,I_m)}{\partial q}\right) \cdot \left(\frac{\partial {p'}_{\sigma(\nu)}(I'_{ch},q')}{\partial q'} - \frac{\partial \tilde{p}'_{\nu}(q',q)}{\partial q'}\right)}}\Bigg|_{q'=q'_{\nu},\, q=q_{\nu}} . \qquad \text{(B.28)}\end{aligned}$$

B.3. Stability prefactor

Equation (B.28) still contains a very complicated relation in the root function. In the following computation, we show that this root function can be rearranged in terms of a stability prefactor, casting the semiclassical tunneling-matrix elements of Eq. (B.28) in the elegant form of a semiclassical propagator in action coordinates, Eq. (B.37).

We start by computing the partial derivative of the saddle points, Eqs. (B.18) and (B.19), with respect to I_m,

$$\frac{\partial q'_{\nu}}{\partial I_m} = \frac{\partial q'_{\nu}(I'_{ch}, I_m)}{\partial I_m}, \qquad \text{(B.29)}$$

$$\frac{\partial q_{\nu}}{\partial I_m} = \frac{\partial q_{\nu}(I'_{ch}, I_m)}{\partial I_m}. \qquad \text{(B.30)}$$

Subsequently, we compute the partial derivative of the final angle θ'_{ν}, Eq. (B.23), with respect to I_m ,

$$\frac{\partial \theta'_{\nu}(I'_{ch}, I_m)}{\partial I_m} = \frac{\partial {\theta'}_{\sigma(\nu)}(I'_{ch}, q')}{\partial q'}\bigg|_{q'=q'_{\nu}} \frac{\partial q'_{\nu}}{\partial I_m}. \qquad \text{(B.31)}$$

We also compute the partial derivative of the right relation in Eq. (B.20) with respect to I_m,

$$\frac{\partial {p'}_{\sigma(\nu)}(I'_{ch}, q')}{\partial q'}\bigg|_{q'=q'_{\nu}} \frac{\partial q'_{\nu}}{\partial I_m} = \frac{\partial \tilde{p}'_{\nu}(q', q)}{\partial q'}\bigg|_{q'=q'_{\nu}} \frac{\partial q'_{\nu}}{\partial I_m} + \frac{\partial \tilde{p}'_{\nu}(q', q)}{\partial q}\bigg|_{q=q_{\nu}} \frac{\partial q_{\nu}}{\partial I_m}, \qquad \text{(B.32)}$$

giving

$$\frac{\partial q'_{\nu}}{\partial I_m} = \frac{\frac{\partial \tilde{p}'_{\nu}(q',q)}{\partial q}}{\frac{\partial {p'}_{\sigma(\nu)}(I'_{ch},q')}{\partial q'} - \frac{\partial \tilde{p}'_{\nu}(q',q)}{\partial q'}}\Bigg|_{q'=q'_{\nu},\, q=q_{\nu}} \frac{\partial q_{\nu}}{\partial I_m}. \qquad \text{(B.33)}$$

Furthermore, we compute the partial derivative of the right relation in Eq. (B.22) with respect to I_m

$$\left.\frac{\partial \tilde{p}_\nu(q',q)}{\partial q'}\right|_{q'=q'_\nu}\frac{\partial q'_\nu}{\partial I_m}+\left.\frac{\partial \tilde{p}_\nu(q',q)}{\partial q}\right|_{q=q_\nu}\frac{\partial q_\nu}{\partial I_m}=\left.\frac{\partial p_{\mu(\nu)}(q,I_m)}{\partial q}\right|_{q=q_\nu}\frac{\partial q_\nu}{\partial I_m}+\left.\frac{\partial p_{\mu(\nu)}(q,I_m)}{\partial I_m}\right|_{q=q_\nu}, \tag{B.34}$$

which together with Eq. (B.33) gives

$$\frac{\partial q_\nu}{\partial I_m}=\left.\frac{\left(\frac{\partial p'_{\sigma(\nu)}(I'_{ch},q')}{\partial q'}-\frac{\partial \tilde{p}'_\nu(q',q)}{\partial q'}\right)\frac{\partial p_{\mu(\nu)}(q,I_m)}{\partial I_m}}{\frac{\partial \tilde{p}_\nu(q',q)}{\partial q'}\frac{\partial \tilde{p}'_\nu(q',q)}{\partial q}+\left(\frac{\partial \tilde{p}_\nu(q',q)}{\partial q}-\frac{\partial p_{\mu(\nu)}(q,I_m)}{\partial q}\right)\cdot\left(\frac{\partial p'_{\sigma(\nu)}(I'_{ch},q')}{\partial q'}-\frac{\partial \tilde{p}'_\nu(q',q)}{\partial q'}\right)}\right|_{q'=q'_\nu,\,q=q_\nu}. \tag{B.35}$$

Combining Eqs. (B.31), (B.33), and (B.35) gives a simplified expression for the stability prefactor in Eq. (B.28) according to

$$\frac{\partial \theta'_\nu(I'_{ch},I_m)}{\partial I_m}=\left.\frac{\frac{\partial \theta'_{\sigma(\nu)}(I'_{ch},q')}{\partial q'}\cdot\frac{\partial \tilde{p}'_\nu(q',q)}{\partial q}\cdot\frac{\partial p_{\mu(\nu)}(q,I_m)}{\partial I_m}}{\frac{\partial \tilde{p}_\nu(q',q)}{\partial q'}\frac{\partial \tilde{p}'_\nu(q',q)}{\partial q}+\left(\frac{\partial \tilde{p}_\nu(q',q)}{\partial q}-\frac{\partial p_{\mu(\nu)}(q,I_m)}{\partial q}\right)\cdot\left(\frac{\partial p'_{\sigma(\nu)}(I'_{ch},q')}{\partial q'}-\frac{\partial \tilde{p}'_\nu(q',q)}{\partial q'}\right)}\right|_{q'=q'_\nu,\,q=q_\nu}. \tag{B.36}$$

Together with Eq. (B.25) this gives a semiclassical prediction of regular-to-chaotic tunneling-matrix elements in the shape of a semiclassical propagator between classical actions I_m and I'_{ch},

$$\langle I'_{ch}|\widehat{U}|I_m\rangle=\sum_\nu\sqrt{\frac{\mathrm{i}}{2\pi\hbar}\frac{\partial^2\bar{\mathcal{S}}_\nu(I'_{ch},I_m)}{\partial I'_{ch}\,\partial I_m}}\exp\left(\frac{\mathrm{i}}{\hbar}\bar{\mathcal{S}}_\nu(I'_{ch},I_m)\right), \tag{B.37}$$

for the tunneling-matrix elements.

B.4. WKB-like actions and semiclassical normalization for basis states

In order to make the semiclassical propagator for regular-to-chaotic tunneling-matrix elements, given by Eq. (B.37) applicable for practical use, we evaluate the generating functions $\mathcal{F}^{(2)}_\mu$ and $\mathcal{F}^{(3)}_\sigma$, required for computing the action $\bar{\mathcal{S}}_\nu(I'_{ch},I_m)$, Eq. (B.24), by integrating Eqs. (B.4) and (B.6), along quantizing tori $I=I_m$ and $I'=I'_{ch}$, respectively,

$$\mathcal{F}^{(2)}_\mu(q,I_m)=\int\limits_{\mathcal{C}_{m,\mu}}p_\mu(\tilde{q},I_m)\mathrm{d}\tilde{q}+\tilde{f}(I_m)\qquad\text{with}\quad\tilde{f}(I_m)=-\mathrm{i}\hbar\log(\hbar), \tag{B.38}$$

$$\mathcal{F}^{(3)}_\sigma(I'_{ch},q')=\int\limits_{\mathcal{C}_{ch,\sigma}}p'_\sigma(I'_{ch},\tilde{q}')\mathrm{d}\tilde{q}'+\tilde{f}(I'_{ch})\quad\text{with}\quad\tilde{f}(I'_{ch})=-\mathrm{i}\hbar\log(\hbar). \tag{B.39}$$

The integrations take place along curves $\mathcal{C}_{m,\mu}$ and $\mathcal{C}_{ch,\sigma}$, on the (possibly complexified) tori of action I_m and I'_{ch}, respectively. The curve $\mathcal{C}_{m,\mu}$ originates from a conveniently chosen reference point (q_m, p_m) on the real phase-space branch $\mathcal{T}_m$ of the quantizing torus I_m. It ends at the point $(q, p_\mu(q, I_{ch}))$, with q determined from the considered basis state $\langle q|I_m\rangle$. In contrast, the curve $\mathcal{C}_{ch,\sigma}$ originates from the point $(q', p'_\sigma(I'_{ch}, q'))$, with q' determined from the basis state $\langle I'_{ch}|q'\rangle$. It ends at the conveniently chosen reference point (q'_{ch}, p'_{ch}) on the real phase-space branch $\mathcal{T}_{ch}$ of the quantizing torus I'_{ch}. The choice of the reference points and the real part of the integration constants $\mathrm{Re}\,\tilde{f}(I_m)$ and $\mathrm{Re}\,\tilde{f}(I'_{ch})$ affect the irrelevant global phase of the initial and final basis states, Eqs. (B.2) and (B.3), respectively. The imaginary part of the integration constants are chosen such that the basis states, Eqs. (B.2) and (B.3), are normalized. This is confirmed by inserting Eq. (B.38) into Eq. (B.2) and using Eq. (B.5),

$$\langle q|I_m\rangle = \sum_\mu \sqrt{\frac{1}{2\pi \mathrm{i}} \frac{\partial\theta(q, I_m)}{\partial q}} \exp\left(\frac{\mathrm{i}}{\hbar} \int\limits_{\mathcal{C}_{m,\mu}} p_\mu(\tilde{q}, I_m)\mathrm{d}\tilde{q}\right), \tag{B.40}$$

or similarly inserting (B.39) into (B.3) and using Eq. (B.7),

$$\langle I'_{ch}|q'\rangle = \sum_\sigma \sqrt{\frac{1}{2\pi \mathrm{i}} \frac{\partial\theta'(I'_{ch}, q')}{\partial q'}} \exp\left(-\frac{\mathrm{i}}{\hbar} \int\limits_{\mathcal{C}_{ch,\sigma}} p'_\sigma(I'_{ch}, \tilde{q}')\mathrm{d}\tilde{q}'\right), \tag{B.41}$$

respectively. This gives WKB-like wave functions whose normalization is semiclassically dominated by the classical probability densities on the real phase-space branches $\mathcal{T}_m$ and $\mathcal{T}_{ch}$ of the quantizing tori I_m and I'_{ch} [66, 67],

$$\int\limits_{-\infty}^{\infty} \mathrm{d}q\, |\langle q|I_m\rangle|^2 \overset{\text{S.P.A.}}{=} \oint\limits_{\mathcal{T}_m} \frac{\mathrm{d}q}{2\pi} \left|\frac{\partial\theta(q, I_m)}{\partial q}\right|, \tag{B.42}$$

$$\int\limits_{-\infty}^{\infty} \mathrm{d}q'\, |\langle I'_{ch}|q'\rangle|^2 \overset{\text{S.P.A.}}{=} \oint\limits_{\mathcal{T}_{ch}} \frac{\mathrm{d}q'}{2\pi} \left|\frac{\partial\theta'(q', I'_{ch})}{\partial q'}\right|, \tag{B.43}$$

respectively. Exploiting that $\mathcal{T}_m$ and $\mathcal{T}_{ch}$ can be parametrized by $q = q(\theta, I_m)$ and $q' = q'(I'_{ch}, \theta')$ the normalization is evident,

$$\oint\limits_{\mathcal{T}_m} \frac{\mathrm{d}q}{2\pi} \left|\frac{\partial\theta(q, I_m)}{\partial q}\right| = \int\limits_0^{2\pi} \frac{\mathrm{d}\theta}{2\pi} = 1, \tag{B.44}$$

$$\oint\limits_{\mathcal{T}_{ch}} \frac{\mathrm{d}q'}{2\pi} \left|\frac{\partial\theta'(q', I'_{ch})}{\partial q'}\right| = \int\limits_0^{2\pi} \frac{\mathrm{d}\theta'}{2\pi} = 1. \tag{B.45}$$

This concludes our derivation. We combine Eqs. (B.38) and (B.39) with the semiclassical propagator for regular-to-chaotic tunneling-matrix elements, Eq. (B.37) and its corresponding action Eq. (B.24) giving our final result, Eq. (4.6), with the action given by Eq. (4.7). Furthermore, we introduce a Maslov phase ϕ_ν which accounts for additional phase shifts due to turning points [67, 91, 92].

List of Figures

1.1. Complex paths for integrable versus non-integrable systems 2

2.1. Phase space of the standard map 9
2.2. Scheme of resonances for the standard map 11
2.3. Lowest order resonances in the standard map 12
2.4. Scheme of partial barriers in the standard map 12
2.5. Quantum manifestations of the mixed phase space 18
2.6. Quantum manifestations of partial barriers 20
2.7. Quantum manifestations of partial barriers 20
2.8. Quantum manifestations of non-linear resonance chains 21

3.1. Open system 24
3.2. Direct regular-to-chaotic tunneling rates of the standard map 26
3.3. Regular-to-chaotic tunneling rates with resonance-assisted tunneling effects 27
3.4. Regular-to-chaotic tunneling rates for non-absorbed hierarchical region 28
3.5. Regular-to-chaotic tunneling rates for weakly absorbed hierarchical region 29
3.6. Regular-to-chaotic tunneling rates with absorbed hierarchical region 30
3.7. Regular-to-chaotic tunneling rates compared to splittings of chaos-assisted tunneling . 31
3.8. Comparing the phase space of the standard map to the phase space of a fictitious integrable system 37
3.9. Eigenstates of a non-integrable systems versus basis states from a fictitious integrable system 41
3.10. Tunneling rates from the improved fictitious integrable system approach 42
3.11. Tunneling rates from regular basis states 42
3.12. Regular-to-chaotic tunneling rates using the fictitious integrable system approach inconsistently 43
3.13. Tunneling rates from the fictitious integrable system approach 44

4.1. Dominant complex paths of the standard map for the fictitious integrable system approach 54
4.2. Dominant complex paths of the standard map for the fictitious integrable system approach in action–angle coordinates 55
4.3. Dominant complex paths of the standard map for the improved fictitious integrable system approach 57

4.4. Semiclassical tunneling-matrix elements 58
4.5. Semiclassical regular-to-chaotic tunneling rates from summed tunneling-matrix elements 60
4.6. Semiclassical regular-to-chaotic tunneling rates from complex paths to the boundary of the absorber 60
4.7. Relative contributions of each complex path to the regular-to-chaotic tunneling rate . . 61
4.8. Semiclassical regular-to-chaotic tunneling rates from a singe complex path 62
4.9. Semiclassical regular-to-chaotic tunneling rates for the improved fictitious integrable system approach 63
4.10. Semiclassical regular-to-chaotic tunneling rates for absorbers beyond the inner partial barrier 64
4.11. Phase space of the complexified standard map 68
4.12. Survival times and frequencies of complex orbits 68
4.13. Invariant tori of the complexified standard map 70
4.14. Tunneling paths in complexified phase space 71

Bibliography

[1] F. Hund: *Zur Deutung der Molekelspektren. I*, Zeitschrift für Physik **40** (1927), 742–764. Cited on page 1.

[2] F. Hund: *Zur Deutung der Molekelspektren. III.*, Zeitschrift für Physik **43** (1927), 805–826. Cited on page 1.

[3] G. Gamow: *Zur Quantentheorie des Atomkernes*, Zeitschrift für Physik **51** (1928), 204–212. Cited on page 1.

[4] G. Gamow: *The Quantum Theory of Nuclear Disintegration*, Nature **122** (1928), 805–806. Cited on page 1.

[5] R. W. Gurney and E. U. Condon: *Wave Mechanics and Radioactive Disintegration*, Nature **122** (1928), 439. Cited on page 1.

[6] R. W. Gurney and E. U. Condon: *Quantum Mechanics and Radioactive Disintegration*, Phys. Rev. **33** (1929), 127–140. Cited on page 1.

[7] R. H. Fowler and L. Nordheim: *Electron Emission in Intense Electric Fields*, Proc. R. Soc. Lond. **119** (1928), 173–181. Cited on page 1.

[8] L. Esaki: *Long journey into tunneling*, Rev. Mod. Phys. **46** (1974), 237–244. Cited on page 1.

[9] I. Giaever: *Electron tunneling and superconductivity*, Rev. Mod. Phys. **46** (1974), 245–250. Cited on page 1.

[10] B. D. Josephson: *The discovery of tunnelling supercurrents*, Rev. Mod. Phys. **46** (1974), 251–254. Cited on page 1.

[11] G. Binnig and H. Rohrer: *Scanning tunneling microscopy*, IBM J. Res. Dev. **30** (1986), 355–369. Cited on page 1.

[12] L. J. Lauhon and W. Ho: *Direct Observation of the Quantum Tunneling of Single Hydrogen Atoms with a Scanning Tunneling Microscope*, Phys. Rev. Lett. **85** (2000), 4566–4569. Cited on page 1.

[13] A. Yazdani: *Quantum physics: Watching an atom tunnel*, Nature **409** (2001), 471–472. Cited on page 1.

[14] M. Albiez, R. Gati, J. Fölling, S. Hunsmann, M. Cristiani, and M. K. Oberthaler: *Direct Observation of Tunneling and Nonlinear Self-Trapping in a Single Bosonic Josephson Junction*, Phys. Rev. Lett. **95** (2005), 010402. Cited on page 1.

[15] L. D. Landau and E. M. Lifshitz: *Course of Theoretical Physics, Vol.3: Quantum Mechanics*, (Pergamon Press, New York), 3rd edn., (1977). Cited on pages 1, 2, and 19.

[16] E. Merzbacher: *Quantum Mechanics*, (John Wiley and Sons, Hoboken, NJ), 3rd edn., (1998). Cited on pages 1, 2, and 19.

[17] H. Jeffreys: *On certain approximate Solutions of linear differential Equations of the second Order*, Proc. London Math. Soc. **s2-23** (1923), 428–436. Cited on page 1.

[18] G. Wentzel: *Eine Verallgemeinerung der Quantenbedingungen für die Zwecke der Wellenmechanik*, Zeitschrift für Physik **38** (1926), 518–529. Cited on page 1.

[19] H. Kramers: *Wellenmechanik und halbzahlige Quantisierung*, Zeitschrift für Physik **39** (1926), 828–840. Cited on pages 1 and 19.

[20] L. Brillouin: *La mécanique ondulatoire de Schrödinger; une méthode générale de résolution par approximations successives* (in French), C. R. Acad. Sci. Paris **183** (1926), 24–26. Cited on page 1.

[21] L. Brillouin: *Remarques sur la mécanique ondulatoire* (in French), Le Journal de Physique et le Radium **7** (1926), 353–368. Cited on page 1.

[22] M. J. Davis and E. J. Heller: *Quantum dynamical tunnelling in bound states*, J. Chem. Phys. **75** (1981), 246–254. Cited on page 1.

[23] S. Keshavamurthy and P. Schlagheck: *Dynamical Tunneling: Theory and Experiment*, (CRC Press, New York), 1st edn., (2011). Cited on page 1.

[24] J. M. Greene and I. C. Percival: *Hamiltonian maps in the complex plane*, Physica D **3** (1981), 530–548. Cited on pages 1, 65, 66, and 74.

[25] I. C. Percival: *Chaotic boundary of a Hamiltonial map*, Physica D **6** (1982), 67–77. Cited on pages 1, 65, 66, and 74.

[26] W. A. Lin and L. E. Ballentine: *Quantum tunneling and chaos in a driven anharmonic oscillator*, Phys. Rev. Lett. **65** (1990), 2927–2930. Cited on page 1.

[27] O. Bohigas, S. Tomsovic, and D. Ullmo: *Manifestations of classical phase space structures in quantum mechanics*, Phys. Rep. **223** (1993), 43–133. Cited on pages 1, 23, 32, 46, and 73.

[28] S. Tomsovic and D. Ullmo: *Chaos-assisted tunneling*, Phys. Rev. E **50** (1994), 145–162. Cited on pages 1, 23, and 32.

[29] F. Leyvraz and D. Ullmo: *The level splitting distribution in chaos-assisted tunnelling*, J. Phys. A **29** (1996), 2529–2551. Cited on page 1.

[30] S. Tomsovic: *Chaos-assisted tunnelling in the absence of reflexion symmetry*, J. Phys. A **31** (1998), 9469–9481. Cited on page 1.

[31] K. Richter and D. Wintgen: *Stable planetary atom configurations*, Phys. Rev. Lett. **65** (1990), 1965–1965. Cited on page 2.

[32] J. Zakrzewski, D. Delande, and A. Buchleitner: *Ionization via chaos assisted tunneling*, Phys. Rev. E **57** (1998), 1458–1474. Cited on pages 2 and 74.

[33] P. Schlagheck and A. Buchleitner: *Stable classical configurations in strongly driven helium*, Physica D **131** (1999), 110–124. Cited on page 2.

[34] A. Buchleitner, D. Delande, and J. Zakrzewski: *Non-dispersive wave packets in periodically driven quantum systems*, Phys. Rep. **368** (2002), 409 – 547. Cited on pages 2 and 74.

[35] S. Keshavamurthy: *Resonance-assisted tunneling in three degrees of freedom without discrete symmetry*, Phys. Rev. E **72** (2005), 045203. Cited on page 2.

[36] S. Wimberger, P. Schlagheck, C. Eltschka, and A. Buchleitner: *Resonance-Assisted Decay of Nondispersive Wave Packets*, Phys. Rev. Lett. **97** (2006), 043001. Cited on pages 2 and 74.

[37] S. Keshavamurthy: *Dynamical tunneling in molecules: quantum routes to energy flow*, Int. Rev. Phys. Chem. **26** (2007), 521–584. Cited on page 2.

[38] W. K. Hensinger et al.: *Dynamical tunnelling of ultracold atoms*, Nature **412** (2001), 52–. Cited on pages 2, 23, and 74.

[39] D. A. Steck, W. H. Oskay, and M. B. Raizen: *Observation of Chaos-Assisted Tunneling Between Islands of Stability*, Science **293** (2001), 274–278. Cited on pages 2, 23, and 74.

[40] A. Mouchet, C. Miniatura, R. Kaiser, B. Grémaud, and D. Delande: *Chaos-assisted tunneling with cold atoms*, Phys. Rev. E **64** (2001), 016221. Cited on pages 2, 23, 25, 52, 73, and 74.

[41] J. U. Nöckel and A. D. Stone: *Ray and wave chaos in asymmetric resonant optical cavities*, Nature **385** (1997), 45–47. Cited on page 2.

[42] V. A. Podolskiy and E. E. Narimanov: *Semiclassical description of chaos-assisted tunneling*, Phys. Rev. Lett. **91** (2003), 263601 (4 pages). Cited on pages 2, 25, 52, 73, and 74.

[43] A. Bäcker, R. Ketzmerick, S. Löck, J. Wiersig, and M. Hentschel: *Quality factors and dynamical tunneling in annular microcavities*, Phys. Rev. A **79** (2009), 063804. Cited on pages 2, 25, 52, 73, and 74.

[44] S. Shinohara, T. Harayama, T. Fukushima, M. Hentschel, T. Sasaki, and E. E. Narimanov: *Chaos-Assisted Directional Light Emission from Microcavity Lasers*, Phys. Rev. Lett. **104** (2010), 163902. Cited on pages 2 and 74.

[45] J. Yang, S.-B. Lee, S. Moon, S.-Y. Lee, S. W. Kim, T. T. A. Dao, J.-H. Lee, and K. An: *Pump-Induced Dynamical Tunneling in a Deformed Microcavity Laser*, Phys. Rev. Lett. **104** (2010), 243601. Cited on pages 2 and 74.

[46] Q. Song, L. Ge, B. Redding, and H. Cao: *Channeling Chaotic Rays into Waveguides for Efficient Collection of Microcavity Emission*, Phys. Rev. Lett. **108** (2012), 243902. Cited on pages 2 and 74.

[47] E. Doron and S. D. Frischat: *Semiclassical Description of Tunneling in Mixed Systems: Case of the Annular Billiard*, Phys. Rev. Lett. **75** (1995), 3661–3664. Cited on pages 2, 25, 52, 73, and 74.

[48] C. Dembowski, H.-D. Gräf, A. Heine, R. Hofferbert, H. Rehfeld, and A. Richter: *First Experimental Evidence for Chaos-Assisted Tunneling in a Microwave Annular Billiard*, Phys. Rev. Lett. **84** (2000), 867–870. Cited on pages 2, 23, and 74.

[49] R. Hofferbert, H. Alt, C. Dembowski, H.-D. Gräf, H. L. Harney, A. Heine, H. Rehfeld, and A. Richter: *Experimental investigations of chaos-assisted tunneling in a microwave annular billiard*, Phys. Rev. E **71** (2005), 046201. Cited on pages 2 and 74.

[50] A. Bäcker, R. Ketzmerick, S. Löck, M. Robnik, G. Vidmar, R. Höhmann, U. Kuhl, and H.-J. Stöckmann: *Dynamical Tunneling in Mushroom Billiards*, Phys. Rev. Lett. **100** (2008), 174103. Cited on pages 2, 25, 52, 73, and 74.

[51] G. Vidmar, H.-J. Stöckmann, M. Robnik, U. Kuhl, R. Höhmann, and S. Grossmann: *Beyond the Berry–Robnik regime: a random matrix study of tunneling effects*, J. Phys. A **40** (2007), 13883. Cited on page 2.

[52] B. Batistić and M. Robnik: *Semiempirical theory of level spacing distribution beyond the Berry–Robnik regime: modeling the localization and the tunneling effects*, J. Phys. A **43** (2010), 215101. Cited on page 2.

[53] A. Bäcker, R. Ketzmerick, S. Löck, and N. Mertig: *Fractional-Power-Law Level Statistics Due to Dynamical Tunneling*, Phys. Rev. Lett. **106** (2011), 024101. Cited on page 2.

[54] T. Rudolf, N. Mertig, S. Löck, and A. Bäcker: *Consequences of flooding on spectral statistics*, Phys. Rev. E **85** (2012), 036213. Cited on page 2.

[55] L. Hufnagel, R. Ketzmerick, M.-F. Otto, and H. Schanz: *Eigenstates Ignoring Regular and Chaotic Phase-Space Structures*, Phys. Rev. Lett. **89** (2002), 154101. Cited on page 2.

[56] A. Bäcker, R. Ketzmerick, and A. G. Monastra: *Flooding of Chaotic Eigenstates into Regular Phase Space Islands*, Phys. Rev. Lett. **94** (2005), 054102 (4 pages). Cited on pages 2 and 19.

[57] J. Feist, A. Bäcker, R. Ketzmerick, S. Rotter, B. Huckestein, and J. Burgdörfer: *Nanowires with Surface Disorder: Giant Localization Lengths and Quantum-to-Classical Crossover*, Phys. Rev. Lett. **97** (2006), 116804. Cited on page 2.

[58] J. Feist, A. Bäcker, R. Ketzmerick, J. Burgdörfer, and S. Rotter: *Nanowires with surface disorder: Giant localization length and dynamical tunneling in the presence of directed chaos*, Phys. Rev. B **80** (2009), 245322. Cited on page 2.

[59] O. Brodier, P. Schlagheck, and D. Ullmo: *Resonance-Assisted Tunneling in Near-Integrable Systems*, Phys. Rev. Lett. **87** (2001), 64101. Cited on pages 2, 10, 21, 52, 57, and 73.

[60] O. Brodier, P. Schlagheck, and D. Ullmo: *Resonance-Assisted Tunneling*, Ann. Phys. **300** (2002), 88–136. Cited on pages 2, 10, 21, 65, 69, and 73.

[61] C. Eltschka and P. Schlagheck: *Resonance- and Chaos-Assisted Tunneling in Mixed Regular-Chaotic Systems*, Phys. Rev. Lett. **94** (2005), 14101. Cited on pages 2 and 73.

[62] A. Bäcker, R. Ketzmerick, S. Löck, and L. Schilling: *Regular-to-Chaotic Tunneling Rates Using a Fictitious Integrable System*, Phys. Rev. Lett. **100** (2008), 104101. Cited on pages 2, 12, 23, 26, 32, 34, 36, 41, 43, 46, 47, 49, 57, 59, 73, and 74.

[63] J. Le Deunff and A. Mouchet: *Instantons re-examined: Dynamical tunneling and resonant tunneling*, Phys. Rev. E **81** (2010), 046205. Cited on pages 2 and 73.

[64] S. Löck, A. Bäcker, R. Ketzmerick, and P. Schlagheck: *Regular-to-Chaotic Tunneling Rates: From the Quantum to the Semiclassical Regime*, Phys. Rev. Lett. **104** (2010), 114101. Cited on pages 2, 21, 26, 27, 45, and 74.

[65] A. Bäcker, R. Ketzmerick, and S. Löck: *Direct regular-to-chaotic tunneling rates using the fictitious-integrable-system approach*, Phys. Rev. E **82** (2010), 056208. Cited on pages 2, 23, 25, 26, 31, 32, 34, 36, 41, 43, 46, 47, 49, 52, 57, 59, 73, and 74.

[66] M. V. Berry and K. E. Mount: *Semiclassical approximations in wave mechanics*, Reports on Progress in Physics **35** (1972), 315–397. Cited on pages 2, 56, and 87.

[67] S. Creagh: *Tunnelling in multidimensional systems*, J. Phys. A **27** (1994), 4969–4993. Cited on pages 2, 56, 87, and 88.

[68] M. Wilkinson: *Tunnelling between tori in phase space*, Physica D **21** (1986), 341–354. Cited on page 2.

[69] M. Wilkinson and J. H. Hannay: *Multidimensional tunnelling between excited states*, Physica D **27** (1987), 201–212. Cited on page 2.

[70] S. C. Creagh: *Tunneling in two dimensions*, in: *Tunneling in Complex Systems*, vol. 5 of *Proceedings from the Institute for Nuclear Theaory*, 35–100, (World Scientific, Singapore, New Jersey, London, Hong Kong), 1st edn., (1998). Cited on page 2.

[71] M. Sheinman, S. Fishman, I. Guarneri, and L. Rebuzzini: *Decay of quantum accelerator modes*, Phys. Rev. A **73** (2006), 052110. Cited on pages 2, 52, 57, and 73.

[72] A. Mouchet: *Importance of the Wick rotation on tunnelling*, J. Phys. A **40** (2007), F663. Cited on pages 2 and 31.

[73] S. C. Creagh: *Directional Emission from Weakly Eccentric Resonators*, Phys. Rev. Lett. **98** (2007), 153901. Cited on pages 2, 52, 57, and 73.

[74] S. C. Creagh and M. M. White: *Differences between emission patterns and internal modes of optical resonators*, Phys. Rev. E **85** (2012), 015201. Cited on page 2.

[75] A. Shudo and K. S. Ikeda: *Tunneling Effect and the Natural Boundary of Invariant Tori*, Phys. Rev. Lett. **109** (2012), 154102. Cited on pages 2, 52, 57, and 73.

[76] A. Shudo and K. S. Ikeda: *Complex Classical Trajectories and Chaotic Tunneling*, Phys. Rev. Lett. **74** (1995), 682–685. Cited on pages 2, 3, 47, 49, 55, 56, and 73.

[77] A. Shudo and K. S. Ikeda: *Stokes Phenomenon in Chaotic Systems: Pruning Trees of Complex Paths with Principle of Exponential Dominance*, Phys. Rev. Lett. **76** (1996), 4151–4154. Cited on pages 2, 3, 47, 49, 55, 56, and 73.

[78] A. Shudo and K. S. Ikeda: *Chaotic tunneling: A remarkable manifestation of complex classical dynamics in non-integrable quantum phenomena*, Physica D **115** (1998), 234–292. Cited on pages 2, 3, 47, 49, 56, and 73.

[79] A. Shudo, Y. Ishii, and K. S. Ikeda: *Julia set describes quantum tunnelling in the presence of chaos*, J. Phys. A **35** (2002), L225. Cited on pages 2, 3, 47, 49, 65, and 73.

[80] A. Shudo, Y. Ishii, and K. S. Ikeda: *Chaos attracts tunneling trajectories: A universal mechanism of chaotic tunneling*, Europhys. Lett. **81** (2008), 50003. Cited on pages 2, 3, 47, 49, 65, 67, 73, and 74.

[81] A. Shudo, Y. Ishii, and K. S. Ikeda: *Julia sets and chaotic tunneling: I*, J. Phys. A **42** (2009), 265101. Cited on pages 2, 3, 47, 49, 65, 67, 73, 74, and 80.

[82] A. Shudo, Y. Ishii, and K. S. Ikeda: *Julia sets and chaotic tunneling: II*, J. Phys. A **42** (2009), 265102. Cited on pages 2, 3, 47, 49, 65, 67, 73, and 74.

[83] J. D. Hanson, E. Ott, and T. M. Antonsen: *Influence of finite wavelength on the quantum kicked rotator in the semiclassical regime*, Phys. Rev. A **29** (1984), 819–825. Cited on pages 2, 52, and 73.

[84] B. V. Chirikov: *A universal instability of many-dimensional oscillator systems*, Phys. Rep. **52** (1979), 263–379. Cited on pages 5 and 74.

[85] V. I. Arnold: *Small denominators and problems of stability of motion in classical and Celestial Mechanics*, Russian Mathematical Surveys **18** (1963), 85–191. Cited on page 9.

[86] V. I. Arnold: *Proof of a theorem of A. N. Kolmogorov on the invariance of quasi-periodic motions under small perturbations of the Hamiltonian*, Russ. Math. Surv. **18** (1963), 9–36. Cited on page 9.

[87] D. K. Arrowsmith and C. M. Place: *An Introduction to Dynamical Systems*, (Cambridge University Press, Cambrige), 3rd edn., (1994). Cited on page 9.

[88] R. S. MacKay, J. D. Meiss, and I. C. Percival: *Transport in Hamiltonian systems*, Physica D **13** (1984), 55–81. Cited on page 10.

[89] H. Sambe: *Steady States and Quasienergies of a Quantum-Mechanical System in an Oscillating Field*, Phys. Rev. A **7** (1973), 2203–2213. Cited on page 13.

[90] F. Grossmann: *Theoretical Femtosecond Physics: Atoms and Molecules in Strong Laser Fields*, Springer series on atomic, optical and plasma physics, (Springer, Berlin, Heidelberg), 1st edn., (2008). Cited on page 13.

[91] L. S. Schulman: *Techniques and Applications of Path Integration*, (Dover Publications Inc., Minola, New York), 1st edn., (2005). Cited on pages 13, 49, 82, 85, and 88.

[92] J. D. Murray: *Asymptotic analysis*, (Clarendon Press, Oxford), 1st edn., (1974). Cited on pages 13, 49, 77, 82, 83, 85, and 88.

[93] F. Bloch: *Über die Quantenmechanik der Elektronen in Kristallgittern*, Zeitschrift für Physik **52** (1929), 555–600. Cited on page 14.

[94] J. H. Hannay and M. V. Berry: *Quantization of linear maps on a torus-fresnel diffraction by a periodic grating*, Physica D **1** (1980), 267 – 290. Cited on pages 16 and 17.

[95] M. Degli Esposti and S. Graffi: *Mathematical aspects of quantum maps*, in: *The Mathematical Aspects of Quantum Maps* [135], 49–90. Cited on pages 16 and 40.

[96] J. P. Keating, F. Mezzadri, and J. M. Robbins: *Quantum boundary conditions for torus maps*, Nonlinearity **12** (1999), 579–591. Cited on page 17.

[97] S.-J. Chang and K.-J. Shi: *Evolution and exact eigenstates of a resonant quantum system*, Phys. Rev. A **34** (1986), 7–22. Cited on page 17.

[98] M. V. Berry, N. L. Balazs, M. Tabor, and A. Voros: *Quantum maps*, Ann. Phys. **122** (1979), 26–63. Cited on page 17.

[99] E. B. Bogomolny: *Semiclassical quantization of multidimensional systems*, Nonlinearity **5** (1992), 805–886. Cited on page 17.

[100] A. Bäcker: *Numerical Aspects of Eigenvalue and Eigenfunction Computations for Chaotic Quantum Systems*, in: Degli Esposti and Graffi [135], 91–144. Cited on page 17.

[101] K. Husimi: *Some formal properties of the density matrix*, Proc. Phys. Math. Soc. Jpn. **22** (1940), 264–314. Cited on page 18.

[102] C. Cohen-Tannoudji, B. Diu, and F. Laloë: *Quantenmechanik Teil 1*, (Walter de Gruyter, Berlin, New York), 2nd edn., (1999). Cited on page 18.

[103] C. Cohen-Tannoudji, B. Diu, and F. Laloë: *Quantenmechanik Teil 2*, (Walter de Gruyter, Berlin, New York), 2nd edn., (1999). Cited on page 18.

[104] I. C. Percival: *Regular and irregular spectra*, J. Phys. B **6** (1973), L229–L232. Cited on page 18.

[105] M. V. Berry: *Regular and irregular semiclassical wavefunctions*, J. Phys. A **10** (1977), 2083–2091. Cited on page 18.

[106] A. Voros: *Semi-classical ergodicity of quantum eigenstates in the Wigner representation*, in: *Stochastic Behavior in Classical and Quantum Hamiltonian Systems* (Eds. G. Casati and J. Ford), vol. 93 of *Lecture Notes in Physics*, 326–333, (Springer Berlin Heidelberg), (1979). Cited on page 18.

[107] N. Bohr: *I. On the constitution of atoms and molecules*, Philosophical Magazine Series 6 **26** (1913), 1–25. Cited on page 19.

[108] N. Bohr: *II. On the constitution of atoms and molecules*, Philosophical Magazine Series 6 **26** (1913), 476–502. Cited on page 19.

[109] A. Sommerfeld: *Zur Quantentheorie der Spektrallinien*, Annalen der Physik **356** (1916), 1–94. Cited on page 19.

[110] A. Bäcker, R. Ketzmerick, and A. G. Monastra: *Universality in the flooding of regular islands by chaotic states*, Phys. Rev. E **75** (2007), 066204. Cited on page 19.

[111] M. Michler, A. Bäcker, R. Ketzmerick, H.-J. Stöckmann, and S. Tomsovic: *Universal Quantum Localizing Transition of a Partial Barrier in a Chaotic Sea*, Phys. Rev. Lett. **109** (2012), 234101. Cited on pages 19, 28, and 73.

[112] M. Michler: *Quantum signatures of partial barriers in phase space*, Dissertation, Technische Universität Dresden, Fachrichtung Physik, (2011). Cited on pages 19, 28, and 73.

[113] N. Moiseyev: *Quantum theroy of resonances: calculating energies, widths and cross-sections by complex scaling*, Phys. Rep. **302** (1998), 212 – 293. Cited on page 24.

[114] Á. Vibók and G. G. Balint-Kurti: *Reflection and transmission of waves by a complex potential – a semiclassical Jeffreys-Wentzel-Kramers-Brillouin treatment*, J. Chem. Phys. **96** (1992), 7615–7622. Cited on page 24.

[115] Á. Vibók and G. G. Balint-Kurti: *Parametrization of complex absorbing potentials for time-dependent quantum dynamics*, J. Phys. Chem. **96** (1992), 8712–8719. Cited on page 24.

[116] N. Mertig, S. Löck, A. Bäcker, R. Ketzmerick, and A. Shudo: *Complex paths for regular-to-chaotic tunnelling rates*, Europhys. Lett. **102** (2013), 10005. Cited on pages 26, 47, and 74.

[117] S. Löck and P. Schlagheck: (2012), private communication. Cited on page 29.

[118] M. Körber: *Fraktales Weylgesetz in Systemen mit gemischtem Phasenraum*, Diplomarbeit, Technische Universität Dresden, Fachrichtung Physik, (2012). Cited on page 34.

[119] S. Löck: (2013), private communication. Cited on page 36.

[120] J. Laskar, C. Froeschlé, and A. Celletti: *The measure of chaos by the numerical analysis of the fundamental frequencies. Application to the standard mapping*, Physica D **56** (1992), 253–269. Cited on pages 36, 37, 67, and 69.

[121] H. Weyl: *Quantenmechanik und Gruppentheorie*, Zeitschrift für Physik **46** (1927), 1–46. Cited on page 38.

[122] J. E. Campbell: *On a Law of Combination of Operators*, Proc. London Math. Soc. **s1-29** (1897), 14–32. Cited on page 38.

[123] H. F. Baker: *Alternants and continuous groups*, Proc. London Math. Soc. **s2-3** (1905), 24–47. Cited on page 38.

[124] A. Shudo and K. S. Ikeda: *Stokes geometry for the quantum Hénon map*, Nonlinearity **21** (2008), 1831. Cited on page 56.

[125] T. Onishi, A. Shudo, K. S. Ikeda, and K. Takahashi: *Tunneling mechanism due to chaos in a complex phase space*, Phys. Rev. E **64** (2001), 025201. Cited on page 65.

[126] E. Bedford and J. Smillie: *Polynomial diffeomorphisms of* C^2*: currents, equilibrium measure and hyperbolicity*, Inventiones mathematicae **103** (1991), 69–99. Cited on page 65.

[127] E. Bedford and J. Smillie: *Polynomial Diffeomorphisms of* C^2*. II: Stable Manifolds and Recurrence*, Journal of the American Mathematical Society **4** (1991), pp. 657–679. Cited on page 65.

[128] E. Bedford and J. Smillie: *Polynomial diffeomorphisms of* C^2, Mathematische Annalen **294** (1992), 395–420. Cited on page 65.

[129] E. Bedford, M. Lyubich, and J. Smillie: *Polynomial diffeomorphisms of C^2. IV: The measure of maximal entropy and laminar currents*, Inventiones mathematicae **112** (1993), 77–125. Cited on page 65.

[130] K. Clauß: *Dynamik der komplexifizierten Standardabbildung*, Bachelorarbeit, Technische Universität Dresden, Fachrichtung Physik, (2012). Cited on page 65.

[131] F. Fritzsch: *Beschreibung von resonanzunterstützten Tunnelprozessen mit komplexen Pfaden*, Bachelorarbeit, Technische Universität Dresden, Fachrichtung Physik, (2012). Cited on page 73.

[132] V. I. Arnold: *Instability of dynamical systems with several degrees of freedom*, Sov. Math. Dokl. **6** (1964), 581–585. Cited on page 74.

[133] M. Richter: *Classical and quantum investigations of four-dimensional maps with a mixed phase space*, Dissertation, Technische Universität Dresden, Fachrichtung Physik, (2012). Cited on page 74.

[134] W. H. Miller: *Classical-Limit Quantum Mechanics and the Theory of Molecular Collisions*, no. 25 in Advances in Chemical Physics, 69–175, (John Wiley and Sons, Inc., Hoboken, NJ, USA), (1974). Cited on page 81.

[135] M. Degli Esposti and S. Graffi (eds.): *The Mathematical Aspects of Quantum Maps*, no. 618 in Lect. Notes Phys., (Springer-Verlag, Berlin), (2003). Cited on pages 97 and 98.

Acknowledgements

The years of my PhD have been a happy and satisfying period of my life. I would like to express my gratitude for this by thanking the people who made this possible.

Above all it is a great pleasure to thank my supervisors Roland Ketzmerick for giving me the opportunity of working on a topic as fascinating as regular-to-chaotic tunneling. Furthermore, I would like to thank him for investing into my scientific education, discussing with me, and supporting me patiently in productive and harder times of my PhD. Furthermore, I thank him for creating the pleasant, cordial and productive working environment in his team which is the basis for enjoying the pleasures of scientific everyday life. In very much the same way I thank Roland Ketzmerick's supervisor team Arnd Bäcker and Steffen Löck for supporting this scientific mission and investing into this PhD in every possible way.

One of the biggest pleasures in working on a PhD is of course the opportunity of collaborating with so many interesting and open minded people from all around the globe. For this opportunity I would especially like to thank Akira Shudo. The discussions with him have always been enlightening and provided a great boost for this PhD. Furthermore, I am extremely grateful for having been given the opportunity to meet and discuss with Kensuke Ikeda, Stephen Creagh, Peter Schlagheck, Steven Tomsovic, Denis Ullmo, Amaury Mouchet, Shmul Fishman, Italo Guarneri, Srihari Keshavamurty, and Hans-Jürgen Stöckman. Most of these people I was able to meet at the Advanced Study Group "Towards a Semiclassical Theory of Dynamical Tunneling" held in Dresden in 2011. At this point I would also like to acknowledge the scientific networks provided by the international Max Planck research school "Dynamical Processes in Atoms, Molecules, and Solids" and the DFG research unit FOR760 "Scattering Systems with Complex Dynamics" which helped broadening my scientific scope.

Moreover, I would like to thank all the fabulous members of the computational physics gang: Steffen Löck, Waltraut Wustmann, Lars Bittrich (now I talk a little Linux), Matthias Michler, Martin Richter (keep it rolling), Clemens Löbner, Torsten Rudolf, Martin J. Körber, Steffen Lange, Alexander Schnell (keep it trolling), Konstantin Clauß, Felix Fritzsch, Franziska Onken, Julius Kullig, and Jérémy Le Deunf for collaboration, support, and friendship. Working with all of you has been and still is amazing. Special thanks for proofreading this manuscript goes to Martin J. Körber and Steffen Löck.

Achieving a PhD is of course only possible with a good work-life balance. Therefore I thank all of my friends, especially Elisabeth, Dietrich, and Martin, for balancing me during my PhD.

Finally, I would like to thank my parents, Ingrid and Michael, for being a great family and offering support wherever they can.

Versicherung

Diese Arbeit wurde am Institut für Theoretische Physik der Technischen Universität Dresden unter der wissenschaftlichen Betreuung Prof. Dr. Roland Ketzmericks durchgeführt.

Hiermit versichere ich, dass ich die vorliegende Arbeit ohne unzuls̈sige Hilfe Dritter und ohne Benutzung anderer als der angegebenen Hilfsmittel angefertigt habe; die aus fremden Quellen direkt oder indirekt übernommenen Gedanken sind als solche kenntlich gemacht. Die Arbeit wurde bisher weder im Inland noch im Ausland in gleicher oder ähnlicher Form einer anderen Prüfungsbehörde vorgelegt.

Darüber hinaus erkenne ich die Promotionsordnung der Fakultät Mathematik und Naturwissenschaften der Technischen Universität Dresden vom 23. Februar 2011 an.

Normann Mertig

Dresden, 06.06. 2013